OSTEOARTHRITIS

Cartilage-on-a-chip to aid OA drug development

> chondrocytes grown under hyper-physiological compression for 7 days showed a distinct OA-like phenotype

The development of disease-modifying osteoarthritis (OA) drugs (DMOADs) has been hampered by a lack of experimental models that accurately recapitulate the disease phenotype. However, a new cartilage-on-a-chip device looks set to open up the possibility of high-throughput drug screening for OA.

"The conceptual design was inspired by a previous beating heart-on-chip device," explains last author Marco Rasponi. "The device consists of a top cell culture chamber in which a 3D cell-laden hydrogel is confined by two rows of overhanging posts in a miniaturized rectangular channel. This chamber lies on a membrane covering a pneumatic chamber. As the pressure in the pneumatic chamber increases, the membrane bends upward and compresses the hydrogel while the hanging posts limit the lateral expansion."

The researchers first used this device to culture adult human articular chondrocytes in a synthetic polyethylene glycol hydrogel, thereby creating a microtissue, or cartilage-on-a-chip. "A cartilaginous construct was achieved in the device following 14 days of chondrogenic differentiation in a 3D environment, and was characterized by the deposition of extracellular matrix rich in type II collagen and aggrecan, two major constituents of adult cartilage," states co-first author Andrea Mainardi.

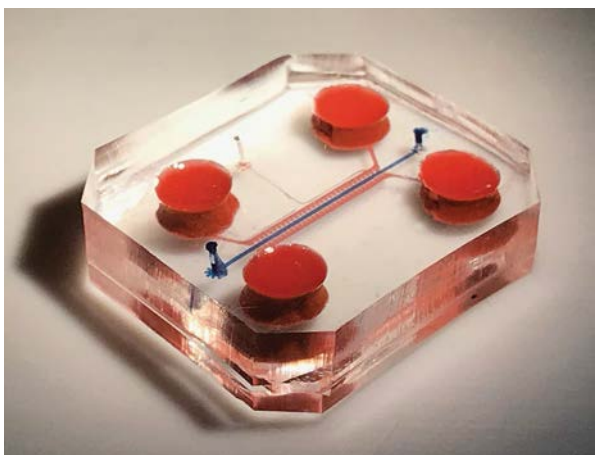

Photograph of an assembled device. Adapted from Occhetta, P. et al. *Nat. Biomed. Eng.* **3**, 545–557 (2019)

Evidence that abnormal joint loading and biomechanics can influence the development of OA led the researchers to add cyclical rounds of compression to the culture conditions to try and create OA-like cartilage. Two different levels of compression were used: 10% (physiological compression) and 30% (hyper-physiological compression). Chondrocytes grown under hyper-physiological compression for 7 days showed a distinct OA-like phenotype at a genetic and cellular level.

"A major finding of this paper is that mechanical hyper-physiological compression alone is somehow sufficient to elicit OA-like traits in a cartilaginous construct," says corresponding author Andrea Barbero. "The OA-like traits were achieved without the need for the administration of cytokines, which are often used in OA in vitro models."

"Despite limitations related to its focus on cartilage, rather than the whole joint, this model is more effective than other ex vivo and in vitro models that rely on single stimuli such as a pro-inflammatory cytokine," says Mary Goldring, an expert in OA who was not involved in this study. "Indeed, using this model it is possible to observe a whole constellation of responses and network interactions involved in promoting the inflammatory response in cartilage, the catabolic–anabolic imbalance and the hypertrophic phenotype that usually cannot be assessed together."

Having established an OA-like model, the researchers tested the effects of anakinra, rapamycin and celecoxib (drugs known to counteract OA-associated inflammation) against dexamethasone as a reference compound, all of which behaved as expected from previous in vivo studies. The hyaluronic acid alkylamide HYADD®4, which is currently being developed for use in OA, was also tested against hyaluronic acid as a reference, and reduced matrix metalloproteinase expression in a manner consistent with the results of preclinical studies.

In the future, the authors hope to further develop the device for high-throughput use. "Including new features such as the introduction of tissues other than cartilage in the model to make it better resemble the whole joint is another option we are looking into," adds Barbero.

"One could imagine that the availability of different compartments might enable the development of a 'joint-on-a-chip', although the introduction of such complexity by, for example, adding a subchondral bone compartment along with synovium and other peri-articular tissues might reduce the ability to show efficacy of a single DMOAD candidate," concludes Goldring. "Nevertheless, one could envision, as a next step, having a two-compartment system with a 'cartilage–synovium co-culture-on-a-chip', since interactions between these two tissues are important for promoting disease progression in post-traumatic OA."

Joanna Collison

ORIGINAL ARTICLE Occhetta, P. et al. Hyperphysiological compression of articular cartilage induces an osteoarthritic phenotype in a cartilage-on-a-chip model. *Nat. Biomed. Eng.* **3**, 545–557 (2019)

IN BRIEF

SYSTEMIC LUPUS ERYTHEMATOSUS

Pregnancy outcomes in SLE are improving

In the USA, in-hospital maternal mortality and overall outcomes improved considerably from 1998 to 2015, especially in pregnant women with systemic lupus erythematosus (SLE), according to a retrospective cohort study. Of the 93,820 hospitalizations of pregnant women with SLE recorded in the National Inpatient Sample database over the 18 year-period, the rate of in-hospital maternal deaths declined from 442 per 100,000 admissions (for 1998 to 2000) to <50 per 100,000 admissions (for 2013 to 2015), which was a greater decline than that reported for pregnant women without SLE.

ORIGINAL ARTICLE Mehta, B. et al. Trends in maternal and fetal outcomes among pregnant women with systemic lupus erythematosus in the United States: a cross-sectional analysis. *Ann. Intern. Med.* https://doi.org/10.7326/M19-0120 (2019)

GOUT

Genetic loci associated with progression to gout

Researchers have identified two genetic loci (in *CNTN5* and *MIR302F*) and one potential locus (in *ZNF724*) associated with progression from hyperuricaemia to gout. The first-of-its-kind genome-wide association study (GWAS) compared patients with gout to individuals with asymptomatic hyperuricaemia, rather than patients with gout to normouricaemic individuals (as has been done in previous GWAS), to identify loci that influence the transition from hyperuricaemia to gout. Comparisons with results from previous GWAS suggested the existence of distinct mechanisms during the normouricaemia-to-hyperuricaemia and hyperuricaemia-to-gout transitions.

ORIGINAL ARTICLE Kawamura, Y. et al. Genome-wide association study revealed novel loci which aggravate asymptomatic hyperuricaemia into gout. *Ann. Rheum. Dis.* https://doi.org/10.1136/annrheumdis-2019-215521 (2019)

RHEUMATOID ARTHRITIS

Mass cytometry markers for stratification of RA?

An exploratory mass cytometry analysis identified candidate markers for distinguishing between patients with newly-diagnosed rheumatoid arthritis (RA) and healthy individuals. A panel of 13 phenotyping and 10 functional markers were used to characterize TNF-mediated signalling patterns in peripheral blood mononuclear cells from patients with RA or healthy individuals, leading to the identification of a small set of RA-specific markers. A combined model of these markers could correctly classify 18 out of 20 patients with RA and 17 out of 20 healthy individuals. These markers could potentially be used for the diagnosis and stratification of RA in the future.

ORIGINAL ARTICLE Bader, L. et al. Candidate markers for stratification and classification in rheumatoid arthritis. *Front. Immunol.* https://doi.org/10.3389/fimmu.2019.01488 (2019)

AUTOIMMUNITY

NET formation differs in SLE and vasculitis

Sera from patients with either systemic lupus erythematosus (SLE) or anti-neutrophil cytoplasmic antibody (ANCA)-associated vasculitis (AAV) induce distinct forms of neutrophil extracellular trap (NET) formation, according to a new study. In an ex vivo comparison, the NET formation differed in morphology, kinetics, triggers and pathways and resembled lytic and non-lytic mechanisms for AAV sera and SLE sera, respectively. Furthermore, the NETs produced had different compositions and immunogenic properties.

ORIGINAL ARTICLE van Dam, L. S. et al. Neutrophil extracellular trap formation is intrinsically distinct in ANCA-associated vasculitis and systemic lupus erythematosus. *Arthritis Rheumatol.* https://doi.org/10.1002/art.41047 (2019)

Credit: Dr_Microbe/iStock/Getty Images Plus

INFLAMMATION

P. gingivalis exacerbates arthritis via gut barrier dysfunction

Porphyromonas gingivalis has frequently been implicated in the pathogenesis of rheumatoid arthritis (RA), but little is known about the mechanisms linking this oral pathobiont to joint inflammation. New findings suggest that, during arthritis, disruption of intestinal resolution pathways impairs gut barrier function, which facilitates pathogenic barrier breach by *P. gingivalis*.

The researchers showed that intestinal lipid mediator profiles were altered in mice with K/BxN serum transfer-induced arthritis in comparison with naive (non-arthritic) mice, with arthritic mice having reduced concentrations of several specialized proresolving mediators (SPMs), including the gut-protective n-3 docosapentaenoic acid (n-3 DPA)-derived resolvin $RvD5_{n\text{-}3\ DPA}$. These alterations were linked with reduced expression of genes involved in epithelial barrier function and *Il10* in gut tissue, as well as a reduction in the number of mucus-producing goblet cells. Expression of IL-10 and IL-10 receptor (IL-10R) was also downregulated in lamina propria macrophages.

Further experiments revealed that inactivation of $RvD5_{n\text{-}3\ DPA}$ during inflammatory arthritis was promoted by upregulation of the SPM-inactivating enzyme 15-prostaglandin dehydrogenase (15-PGDH) and increased metabolism of $RvD5_{n\text{-}3\ DPA}$ to its inactive metabolite 17-oxo-$RvD5_{n\text{-}3\ DPA}$. Notably, incubation with immune complexes upregulated 15-PGDH expression in bone marrow–derived macrophages.

Mice with K/BxN serum transfer-induced arthritis had impaired gut barrier function in comparison with naive mice, marked by downregulation of *Tjp1* and *Lyz1* (encoding a tight junction molecule and an antimicrobial protein, respectively) as well as increased plasma endotoxin concentrations. Inoculation of arthritic mice with *P. gingivalis* exacerbated these changes and led to an increased bacterial load in the lamina propria and the colonic inner mucus layer in comparison with non-inoculated arthritic mice. This breach of bacteria across the gut barrier was not observed in non-arthritic mice inoculated with *P. gingivalis*.

Administration of $RvD5_{n\text{-}3\ DPA}$ restored gut barrier function in *P. gingivalis*-inoculated arthritic mice; bacterial levels in mesentyric lymph nodes were reduced and the lamina propria and colonic inner mucus layer of $RvD5_{n\text{-}3\ DPA}$-treated mice were free of bacteria. $RvD5_{n\text{-}3\ DPA}$ administration also restored expression of *Tjp1, Lyz1* and *Il10* in the intestinal epithelium. The rescue of gut barrier function following $RvD5_{n\text{-}3\ DPA}$ administration was associated with reduced joint inflammation and swelling.

The research could have implications for the management of RA, particularly in patients with periodontal disease. "Our findings suggest that there could be scope for the stratification of patients with RA based on the presence of increased levels of *P. gingivalis* and/or periodontal disease, to devise personalised therapeutic strategies," says corresponding author Magdalena Flak. "In addition, our findings suggest that new therapeutics modelled around $RvD5_{n\text{-}3\ DPA}$ might also be useful drug candidates in RA, since they regulate both the gut barrier and joint inflammation."

Sarah Onuora

ORIGINAL ARTICLE Flak, M. B. et al. Inflammatory arthritis disrupts gut resolution mechanisms, promoting barrier breakdown by *Porphyromonas gingivalis*. *JCI Insight* **4**, e125191 (2019)

SJÖGREN SYNDROME

Immunofibroblasts are the cornerstone of TLS formation in pSS

> proliferation of immunofibroblasts preceded the infiltration of lymphocytes into tissues

Aggregates of lymphocytes and stromal cells known as tertiary lymphoid structures (TLSs) form in peripheral tissues and contribute to autoantibody production and pathology in autoimmune diseases such as primary Sjögren syndrome (pSS). Insight into the mechanism by which TLSs form in pSS is raising hope that this process could one day be targeted therapeutically.

"We believed that this process was driven, within the TLS, by the presence of 'immunofibroblasts', a population of non-haematopoietic stromal cells that are capable of supporting both B and T lymphocyte survival, migration, activation and proliferation and that have similar functional properties to the stromal fibroblasts described in secondary lymphoid organs," explains co-corresponding author Francesca Barone.

On the basis of this belief, Barone and colleagues examined TLSs from patients with pSS, which contained podoplanin-positive fibroblasts that expressed molecules related to either lymphocyte survival within TLSs or to TLS organization. In vitro, these 'immunofibroblasts' proliferated and upregulated cell adhesion molecules in response to IL-22 and IL-13, respectively.

Using a viral infection model of pSS in various types of knockout mice, the researchers unravelled the precise mechanisms by which these immunofibroblasts participate in TLS formation. Activation and proliferation of immunofibroblasts preceded the infiltration of lymphocytes into tissues, was indispensable for TLS formation and was controlled by both IL-13 and IL-22. "Interestingly these cytokines are very different from the signalling

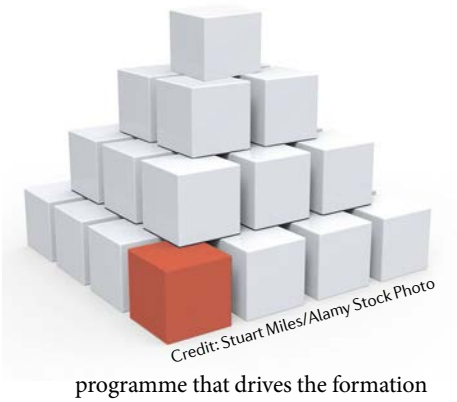

Credit: Stuart Miles/Alamy Stock Photo

programme that drives the formation of secondary lymphoid organs," notes Barone.

"Blocking these cytokines, or eliminating the immunofibroblasts in vivo, was sufficient to disrupt TLSs," states co-corresponding author Mark Coles. "This is particularly important because drugs targeting these two different cytokines have already been developed for other inflammatory conditions, thus can be repurposed for TLS-associated pathologies."

Joanna Collison

ORIGINAL ARTICLE Nayar, S. et al. Immunofibroblasts are pivotal drivers of tertiary lymphoid structure formation and local pathology. *Proc. Natl Acad. Sci. USA* **116**, 13490–13497 (2019)

OSTEOPOROSIS

Gene therapy counteracts bone loss in osteoporosis

Silencing expression of the adaptor protein Schnurri-3 (SHN3) via bone-targeting adeno-associated virus (AAV)-mediated gene therapy could be an attractive approach to treat osteoporosis by promoting bone formation, according to new research published in *Nature Communications*.

Previous work by the researchers had identified SHN3 as a potent suppressor of bone formation. The current paper highlights the therapeutic effects of silencing SHN3 in a mouse model of osteoporosis. The researchers used a recombinant AAV (rAAV) vector carrying an artificial microRNA (amiR) that targets *Shn3* (*amiR-Shn3*). "This technology can confer gene silencing to osteoblast lineage cells residing on the bone surface with a single administration to dramatically alter bone physiology," explains corresponding author Jae-Hyuck Shim.

> administration of rAAV9-*amiR-Shn3* … increased osteoblast activity and trabecular bone mass

Shim and colleagues showed that administration of rAAV9-*amiR-Shn3* either systemically or directly to the knee joints of mice reduced *Shn3* expression in osteoblast-lineage cells and increased osteoblast activity and trabecular bone mass, compared with a control amiR delivered by rAAV9. Furthermore, a single systemic administration of rAAV9-*amiR-Shn3* after the onset of ovariectomy-induced osteoporosis reversed trabecular bone loss and enhanced femur strength and stiffness in mice. "These findings suggest that rAAV9-mediated silencing of *Shn3* improves clinically meaningful endpoints," reports Shim. Notably, systemic delivery of rAAV9-*amiR-Shn3* did not affect osteoclast function in vivo.

Observing that rAAV9 can extensively transduce tissues other than bone, the researchers grafted a bone-targeting peptide motif onto the AAV9 capsid

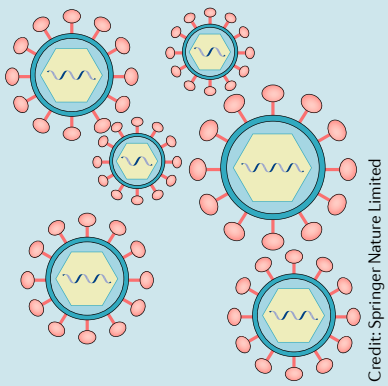

Credit: Springer Nature Limited

scaffold to produce a novel bone-specific capsid of rAAV9 that reduced transgene expression in non-bone peripheral organs, including liver, heart and muscle.

"Systemic delivery of *amiR-Shn3* via bone-targeting AAV9 has clinical utility for counteracting bone loss during osteoporosis," concludes Shim. "However, much more work needs to be done to establish the safety and efficacy of this therapeutic approach."

Sarah Onuora

ORIGINAL ARTICLE Yang, Y.-S. et al. Bone-targeting AAV-mediated silencing of Schnurri-3 prevents bone loss in osteoporosis. *Nat. Commun.* **10**, 2958 (2019)

SYSTEMIC LUPUS ERYTHEMATOSUS

Hitting the right spot on CXCR4


Credit: Steven Milne/Alamy Stock Photo

Toll-like receptor 7 (TLR7) and TLR7-mediated production of type I interferons by plasmacytoid dendritic cells (pDCs) are thought to have central roles in systemic lupus erythematosus (SLE). New findings highlight IT1t, a ligand of the chemokine receptor CXCR4, as an inhibitor of type I interferon production by pDCs, and the IT1t binding site on CXCR4 as a potential therapeutic target in SLE.

Previous studies have shown that a synthetic histamine analogue, clobenpropit, could interact with CXCR4 and inhibit type I interferon production by pDCs. Because clobenpropit also binds histamine receptors, in the new study, the researchers investigated the effects of two CXCR4-specific ligands: AMD3100 (an FDA-approved CXCR4 antagonist) and IT1t (a small amino compound).

The two ligands bind to different sites on CXCR4 and are proposed to have different biological activities. "Interestingly, IT1t is structurally similar to clobenpropit and was, as expected, the only one of these two ligands that could inhibit type I interferon production by pDCs in vitro," explains corresponding author Jean-Philippe Herbeuval.

In ex vivo tonsil mononuclear cell suspensions, IT1t inhibited TLR7-mediated production of IFNα. Furthermore, IT1t treatment reduced systemic inflammation and autoantibody production, and prevented glomerulonephritis, in a TLR7-dependent mouse model of SLE (pristane-induced lupus).

Treatment with IT1t in vitro also abrogated the production of IFNα by resting and stimulated peripheral blood mononuclear cells from patients with SLE, and normalized the expression of inflammatory gene transcripts in these cells.

"We propose that agonists of CXCR4 could represent a novel class of anti-inflammatory molecules that target CXCR4-positive cells such as pDCs," says Nikaïa Smith, co-corresponding author on the study.

> "IT1t treatment reduced systemic inflammation and autoantibody production"

The researchers plan to fully characterize the IT1t binding pocket on CXCR4 and the underlying mechanisms of action, to develop new CXCR4 ligands that have an even higher efficiency for blocking type I interferon production than IT1t, and to expand these findings to other autoimmune diseases (such as dermatomyositis).

Jessica McHugh

ORIGINAL ARTICLE Smith, N. et al. Control of TLR7-mediated type I IFN signaling in pDCs through CXCR4 engagement — A new target for lupus treatment. *Sci. Adv.* **5**, eaav9019 (2019)

OSTEOARTHRITIS

Partial knee replacement comes out on TOP(KAT)

Knee replacement surgery is a common treatment for late-stage osteoarthritis (OA), but evidence as to whether total knee replacement (TKR) or partial knee replacement (PKR) is best has been lacking. TOPKAT, a multicentre randomized controlled trial (RCT), aimed to address questions around the efficacy and cost-effectiveness of TKR versus PKR for knee OA.

"Despite many previous studies and considerable data, we have never had a sufficiently large RCT to answer this important question," says corresponding author David Beard. "TOPKAT has now definitively shown us that both operations provide benefit and are worthwhile but, given the option, PKR is probably the surgery of choice — providing sufficient expertise exists to perform it."

> "no difference was seen in the primary outcome between … PKR and … TKR"

In TOPKAT, 528 patients with isolated medial compartment knee OA were recruited from 27 hospitals in the UK. Patients were randomly allocated to receive either TKR or PKR by expert surgeons at a 1:1 ratio and were evaluated for knee pain and function using the Oxford Knee Score (OKS) as the primary outcome at 5 years post-surgery.

"A unique feature of the research was the incorporation of an innovative combined equipoise–expertise based approach to allow surgeons who were not in equipoise (in other words, who had a strong preference for one implant design over another) to participate," explains Beard. "The expertise-based randomization enabled surgeons not in equipoise to participate in the trial by working in pairs, each providing the operation type they felt was appropriate (as 'experts')."

At 5 years follow-up, no difference was seen in the primary outcome between the patients who received PKR and those who received TKR. The incidences of re-operation and adverse events were also similar between the two groups, contrary to previous findings from systematic reviews. Furthermore, PKR was more effective and less expensive than TKR in the cost-effectiveness analysis.

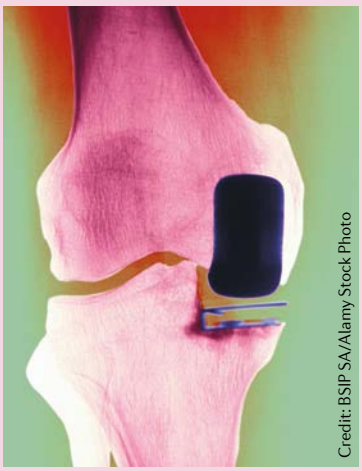
Credit: BSIP SA/Alamy Stock Photo

Whether the results of this trial will be enough to inform future policy regarding the choice of surgery for medial compartment knee OA remains to be seen, but the 10-year follow-up results will be eagerly awaited.

Joanna Collison

ORIGINAL ARTICLE Beard, D. J. et al. The clinical and cost-effectiveness of total versus partial knee replacement in patients with medial compartment osteoarthritis (TOPKAT): 5-year outcomes of a randomised controlled trial. *Lancet* https://doi.org/10.1016/S0140-6736(19)31281-4 (2019)

SYSTEMIC LUPUS ERYTHEMATOSUS

Is ethnicity linked to the severity of SLE manifestations?

Naureen Kabani and Ellen M. Ginzler

Epidemiological data on the prevalence and severity of specific manifestations of systemic lupus erythematosus (SLE) among different ethnic groups are now emerging. The use of rigorous epidemiological methods should enable a better understanding of these features of SLE in different ethnic groups, which could influence disease management.

Refers to Maningding, E. et al. Racial/ethnic differences in prevalence of and time to onset of SLE manifestations: the California Lupus Surveillance Project (CLSP). *Arthritis Care Res.* https://doi.org/10.1002/acr.23887 (2019).

Systemic lupus erythematosus (SLE) is an autoimmune disease that differs in incidence and prevalence in groups of patients from different ethnic backgrounds. In the USA, four registries funded by the Centers for Disease Control and Prevention (CDC) were established in Michigan, New York, Georgia and California to investigate the epidemiology of SLE[1–4]. As well as studying overall incidence and prevalence of SLE, these registries also aimed to evaluate epidemiological differences in the prevalence of specific manifestations of SLE, which is incompletely understood. In a retrospective analysis of data from the CDC-funded California Lupus Surveillance Project (CLSP), Maningding et al.[5] now report that severe manifestations, such as renal and haematological disease, might be common in patients with SLE from minority ethnic groups.

Worldwide differences in SLE related to race and ethnicity are considerably understudied, but some notable findings have been reported. Data from the four CDC-funded SLE registries revealed that populations of individuals classified as 'black', 'Asian/Pacific islander (API)', 'Hispanic' and 'American Indian/Alaskan native' have a higher incidence and prevalence of SLE than 'white' populations in the USA[1–4]. A systematic review of epidemiological studies of SLE from around the world published before 2016 revealed that the highest incidence and prevalence of SLE was in black populations and the lowest in white populations, with Asian and Hispanic populations having intermediate incidences and prevalences[6]. Not surprisingly, one of the studies included in this systematic review[6] described a Hawaiian cohort of patients with SLE, in which the highest prevalence of SLE occurred in Chinese and native Hawaiian individuals and the lowest prevalence in white individuals. A 2.1-fold higher incidence of SLE was noted in Arab-Americans compared with non-Arab populations in the Michigan Lupus Epidemiology Registry[1]. In a 2018 review on the epidemiology of SLE[7], a similarly high age-standardized incidence and prevalence of SLE was reported in the United Arab Emirates, suggesting an ethnic rather than geographical explanation for this high incidence. A study from the UK was also highlighted in the 2018 review[7], in which the highest incidence and prevalence of SLE occurred in Afro-Caribbean individuals.

Aside from variation in SLE incidence and prevalence, data from the USA suggest that variation occurs in specific manifestations and complications of SLE according to ethnicity. A study of all-cause mortality among American Medicaid recipients with SLE between 2000 and 2006 showed mortality to be lower among API or Hispanic individuals than in black, white or Native American individuals[7]. Another analysis of Medicaid data, this time between 2000 and 2010, revealed an increased risk of cardiovascular events among black individuals with SLE compared with white individuals with SLE, and a reduced risk of myocardial infarction in Hispanic or Asian individuals with SLE compared with white individuals with SLE[7]. The same analysis also showed a higher risk of stroke among black or Hispanic individuals with SLE than in white individuals with SLE[7]. Another study into the effect of socioeconomic status on racial and ethnic disparities in pregnancy outcomes for women with SLE in the USA showed that socioeconomic status was a contributor to differences in pregnancy outcomes for African American women, but not for Asian or Hispanic women[8].

Preliminary results from the California Lupus Epidemiology Study (the study population for which was derived from the CLSP registry) showed variation by race and ethnicity in associations between the age of diagnosis of SLE and accrued damage: white individuals had less damage than Asian, African American or Hispanic individuals diagnosed at a similar age[9]. To further probe the racial and ethnic differences in the prevalence of specific manifestations of SLE and the time of onset of these manifestations, Maningding et al.[5] studied data from the CLSP registry with a specific focus on API and Hispanic populations in San Francisco County. The authors retrospectively identified 724 patients with SLE from the CLSP registry and grouped their SLE manifestations into ten clinical categories, including cardiovascular, renal and haematological. The authors also investigated the onset of specific severe manifestations of SLE: lupus nephritis, thrombocytopenia, neuropsychiatric lupus, antiphospholipid syndrome and a combined outcome of these four manifestations. The study cohort consisted of API individuals (36.9%), white individuals (26.2%), black individuals (18.8%) and Hispanic individuals (15.5%).

Compared with white individuals, black, API and Hispanic individuals had a 1.4–1.77-fold higher prevalence of renal manifestations[5]. Similarly, the prevalence of neurological and haematological manifestations was greatest in black individuals (up to 1.5-fold higher than in white individuals for neurological manifestations). The highest risk of developing antiphospholipid syndrome

occurred in API and Hispanic individuals, with a prevalence more than twofold greater than that of other ethnic groups.

The time between onset of SLE to development of lupus nephritis, thrombocytopenia, antiphospholipid syndrome or the combined outcome was shorter for individuals from all minority ethnicities compared with white individuals, and the risk of developing these severe manifestations was greatest in the first year after disease onset[5]. Maningding et al. also noted that the high prevalence of severe manifestations in the API population was unlikely to be attributable to socioeconomic status, as this population had high levels of income and education, and good access to healthcare.

A few points should be considered in interpreting the findings of the study by Maningding et al.[5]. First, the rates of prevalence come from a registry that was active between 2007 and 2009, making them 10 years old. Demographic changes might have occurred in this population since that time, and thus we cannot know if these data accurately represent the current prevalence of SLE manifestations in individuals from racial and ethnic minority groups in San Francisco County. Another point to consider is the lack of available information on coexisting medical conditions, specifically renal manifestations. In this study[5], the category 'renal manifestations' included lupus nephritis, proteinuria, renal transplantation and dialysis; these manifestations can have other, more common, aetiologies such as hypertension and type II diabetes mellitus. It would be worthwhile to explore whether this population had an increased prevalence of such comorbidities and then to reanalyse the data, controlling for these confounding variables.

Lastly, the most important consideration is whether these findings[5] are generalizable, or pertain only to this specific population. Unfortunately, the burden of specific SLE manifestations in specific ethnic groups is understudied and more work needs to be done to explore this area of research before the findings of Maningding et al. can be applied more generally in the USA. Perhaps similar rigorous epidemiological methods could be applied to the other CDC-funded SLE registries to further study differences in specific SLE manifestations in individuals of different ethnicities. More data from around the USA would help to make these findings more generalizable, as would similar data from around the world that encompasses a wider variety of ethnic groups. For example, in the preliminary results of an epidemiological study in Berkshire, UK, the prevalence of lupus nephritis in individuals with a South-Asian background was similar to that in white individuals[10]. However, South-Asian individuals with lupus nephritis were younger than white individuals in this study. In addition, 7% of individuals in this study population were classified as 'other', a group that included individuals of mixed race, East-Asian or Arab background. Notably, this 'other' group had a prevalence of lupus nephritis of 57%, which was substantially higher than the prevalence in white individuals (24%)[10].

Despite these considerations and questions, Maningding et al.[5] have taken an excellent first step towards applying rigorous epidemiological methods to study differences in SLE manifestations in different ethnic groups. Of the CDC-funded SLE registries, the California registry had the largest percentage of API individuals, so the findings regarding the API population come from a robust data source[1–4]. These findings also have important clinical relevance and encourage increased vigilance when treating individuals from different ethnic backgrounds, especially at an early stage in the disease process, in the hope of preventing damage onset and accrual.

*Naureen Kabani and Ellen M. Ginzler**
SUNY-Downstate Medical Center, Department of Medicine, Brooklyn, NY, USA.
**e-mail: ellen.ginzler@downstate.edu*
https://doi.org/10.1038/s41584-019-0271-1

1. Somers, E. C. et al. Population-based incidence and prevalence of systemic lupus erythematosus: the Michigan Lupus Epidemiology and Surveillance program. *Arthritis Rheumatol.* **66**, 369–378 (2014).
2. Izmirly, P. M. et al. The incidence and prevalence of systemic lupus erythematosus in New York County (Manhattan), New York: the Manhattan Lupus Surveillance Program. *Arthritis Rheumatol.* **69**, 2006–2017 (2017).
3. Lim, S. S. et al. The incidence and prevalence of systemic lupus erythematosus, 2002 –2004: the Georgia Lupus Registry. *Arthritis Rheumatol.* **66**, 357–369 (2014).
4. Dall'Era, M. et al. The incidence and prevalence of systemic lupus erythematosus in San Francisco County, California: the California Lupus Surveillance Project. *Arthritis Rheumatol.* 69, (1996–2005 (2017).
5. Maningding, E. et al. Racial/ethnic differences in prevalence of and time to onset of SLE manifestations: the California Lupus Surveillance Project (CLSP). *Arthritis Care Res.* https://doi.org/10.1002/acr.23887 (2019).
6. Rees, F. et al. The worldwide incidence and prevalence of systemic lupus erythematosus: a systematic review of epidemiological studies. *Rheumatology* **56**, 1945–1961 (2017).
7. Stojan, G. & Petri, M. Epidemiology of systemic lupus erythematosus: an update. *Curr. Opin. Rheumatol.* **30**, 144–150 (2018).
8. Kaplowitz, E. T. et al. Contribution of socioeconomic status to racial/ethnic disparities in adverse pregnancy outcomes among women with systemic lupus erythematosus. *Arthritis Care Res.* **70**, 230–235 (2018).
9. Trupin, L. et al. Association between age of SLE diagnosis and disease damage differs across racial/ethnic groups: results from the California Lupus Epidemiology Study [abstract]. *Lupus Sci. Med.* **6** (Suppl. 1), A213 (2019).
10. Gindea, S. & Williams, S. Lupus nephritis in a multi-ethnic cohort of patients with systemic lupus erythematosus from Berkshire, UK [abstract]. *Lupus Sci. Med.* **5** (Suppl. 1), A170 (2018).

Competing interests
The authors declare no competing interests.

GOUT

Defining remission in patients with gout

Thomas Bardin and Pascal Richette

Criteria to define remission in gout could be valuable in clinical trials and practice. But do the available preliminary criteria truly predict the long-term absence of gout signs and symptoms?

Refers to Dalbeth, N. et al. Concurrent validity of provisional remission criteria for gout: a dual-energy CT study. *Arthritis Res. Ther.* **21**, 150 (2019).

Gout symptoms arise from monosodium urate (MSU) crystal deposition, and the best way to obtain persistent disappearance of gout features — that is, gout remission — is to achieve the dissolution of the culprit crystal by lowering serum uric acid (SUA) levels below the saturation point of uric acid, mainly by using urate-lowering therapy (ULT). In 2016, a large group of rheumatologists with an interest in gout published preliminary criteria for gout remission[1], which were presented as preliminary and requiring validation. An attempt to validate the criteria, using advanced imaging to assess MSU crystal deposition, has now been published by Dalbeth et al.[2].

The 2016 provisional definition of remission required that five criteria are met: SUA level <360 μmol/l at two or more time points within the previous 12 months; no tophi; no flare of disease during the past 12 months; pain level <2 on a 0–10 scale at least twice over the past 12 months and no pain score >2; and patient global assessment (PGA) of disease activity score <2 on a 0–10 scale at least

occurred in API and Hispanic individuals, with a prevalence more than twofold greater than that of other ethnic groups.

The time between onset of SLE to development of lupus nephritis, thrombocytopenia, antiphospholipid syndrome or the combined outcome was shorter for individuals from all minority ethnicities compared with white individuals, and the risk of developing these severe manifestations was greatest in the first year after disease onset[5]. Maningding et al. also noted that the high prevalence of severe manifestations in the API population was unlikely to be attributable to socioeconomic status, as this population had high levels of income and education, and good access to healthcare.

A few points should be considered in interpreting the findings of the study by Maningding et al.[5]. First, the rates of prevalence come from a registry that was active between 2007 and 2009, making them 10 years old. Demographic changes might have occurred in this population since that time, and thus we cannot know if these data accurately represent the current prevalence of SLE manifestations in individuals from racial and ethnic minority groups in San Francisco County. Another point to consider is the lack of available information on coexisting medical conditions, specifically renal manifestations. In this study[5], the category 'renal manifestations' included lupus nephritis, proteinuria, renal transplantation and dialysis; these manifestations can have other, more common, aetiologies such as hypertension and type II diabetes mellitus. It would be worthwhile to explore whether this population had an increased prevalence of such comorbidities and then to reanalyse the data, controlling for these confounding variables.

Lastly, the most important consideration is whether these findings[5] are generalizable, or pertain only to this specific population. Unfortunately, the burden of specific SLE manifestations in specific ethnic groups is understudied and more work needs to be done to explore this area of research before the findings of Maningding et al. can be applied more generally in the USA. Perhaps similar rigorous epidemiological methods could be applied to the other CDC-funded SLE registries to further study differences in specific SLE manifestations in individuals of different ethnicities. More data from around the USA would help to make these findings more generalizable, as would similar data from around the world that encompasses a wider variety of ethnic groups. For example, in the preliminary results of an epidemiological study in Berkshire, UK, the prevalence of lupus nephritis in individuals with a South-Asian background was similar to that in white individuals[10]. However, South-Asian individuals with lupus nephritis were younger than white individuals in this study. In addition, 7% of individuals in this study population were classified as 'other', a group that included individuals of mixed race, East-Asian or Arab background. Notably, this 'other' group had a prevalence of lupus nephritis of 57%, which was substantially higher than the prevalence in white individuals (24%)[10].

Despite these considerations and questions, Maningding et al.[5] have taken an excellent first step towards applying rigorous epidemiological methods to study differences in SLE manifestations in different ethnic groups. Of the CDC-funded SLE registries, the California registry had the largest percentage of API individuals, so the findings regarding the API population come from a robust data source[1–4]. These findings also have important clinical relevance and encourage increased vigilance when treating individuals from different ethnic backgrounds, especially at an early stage in the disease process, in the hope of preventing damage onset and accrual.

*Naureen Kabani and Ellen M. Ginzler**
SUNY-Downstate Medical Center, Department of Medicine, Brooklyn, NY, USA.
**e-mail: ellen.ginzler@downstate.edu*
https://doi.org/10.1038/s41584-019-0271-1

1. Somers, E. C. et al. Population-based incidence and prevalence of systemic lupus erythematosus: the Michigan Lupus Epidemiology and Surveillance program. *Arthritis Rheumatol.* **66**, 369–378 (2014).
2. Izmirly, P. M. et al. The incidence and prevalence of systemic lupus erythematosus in New York County (Manhattan), New York: the Manhattan Lupus Surveillance Program. *Arthritis Rheumatol.* **69**, 2006–2017 (2017).
3. Lim, S. S. et al. The incidence and prevalence of systemic lupus erythematosus, 2002 –2004: the Georgia Lupus Registry. *Arthritis Rheumatol.* **66**, 357–369 (2014).
4. Dall'Era, M. et al. The incidence and prevalence of systemic lupus erythematosus in San Francisco County, California: the California Lupus Surveillance Project. *Arthritis Rheumatol.* 69, (1996–2005 (2017).
5. Maningding, E. et al. Racial/ethnic differences in prevalence of and time to onset of SLE manifestations: the California Lupus Surveillance Project (CLSP). *Arthritis Care Res.* https://doi.org/10.1002/acr.23887 (2019).
6. Rees, F. et al. The worldwide incidence and prevalence of systemic lupus erythematosus: a systematic review of epidemiological studies. *Rheumatology* **56**, 1945–1961 (2017).
7. Stojan, G. & Petri, M. Epidemiology of systemic lupus erythematosus: an update. *Curr. Opin. Rheumatol.* **30**, 144–150 (2018).
8. Kaplowitz, E. T. et al. Contribution of socioeconomic status to racial/ethnic disparities in adverse pregnancy outcomes among women with systemic lupus erythematosus. *Arthritis Care Res.* **70**, 230–235 (2018).
9. Trupin, L. et al. Association between age of SLE diagnosis and disease damage differs across racial/ethnic groups: results from the California Lupus Epidemiology Study [abstract]. *Lupus Sci. Med.* **6** (Suppl. 1), A213 (2019).
10. Gindea, S. & Williams, S. Lupus nephritis in a multi-ethnic cohort of patients with systemic lupus erythematosus from Berkshire, UK [abstract]. *Lupus Sci. Med.* **5** (Suppl. 1), A170 (2018).

Competing interests
The authors declare no competing interests.

GOUT

Defining remission in patients with gout

Thomas Bardin and Pascal Richette

Criteria to define remission in gout could be valuable in clinical trials and practice. But do the available preliminary criteria truly predict the long-term absence of gout signs and symptoms?

Refers to Dalbeth, N. et al. Concurrent validity of provisional remission criteria for gout: a dual-energy CT study. *Arthritis Res. Ther.* **21**, 150 (2019).

Gout symptoms arise from monosodium urate (MSU) crystal deposition, and the best way to obtain persistent disappearance of gout features — that is, gout remission — is to achieve the dissolution of the culprit crystal by lowering serum uric acid (SUA) levels below the saturation point of uric acid, mainly by using urate-lowering therapy (ULT). In 2016, a large group of rheumatologists with an interest in gout published preliminary criteria for gout remission[1], which were presented as preliminary and requiring validation. An attempt to validate the criteria, using advanced imaging to assess MSU crystal deposition, has now been published by Dalbeth et al.[2].

The 2016 provisional definition of remission required that five criteria are met: SUA level <360 μmol/l at two or more time points within the previous 12 months; no tophi; no flare of disease during the past 12 months; pain level <2 on a 0–10 scale at least twice over the past 12 months and no pain score >2; and patient global assessment (PGA) of disease activity score <2 on a 0–10 scale at least

> The demonstration of urate deposits by DECT in patients fulfilling the remission criteria raises several issues…

twice over the past 12 months with no score >2. These remission criteria can be viewed as a surrogate endpoint for the disappearance of MSU crystals during ULT. This idea prompted Dalbeth et al.[2] to compare the preliminary gout remission criteria with volumetric measurement of MSU crystal deposition using dual-energy computed tomography (DECT), a modern noninvasive imaging technique that enables detection of MSU deposits with good sensitivity and specificity.

For the validation study[2], Dalbeth et al. used a previously published cross-sectional cohort of 152 patients with gout treated with allopurinol ≥300 mg daily and assessed by physical examination, patient questionnaires and DECT of the hands and feet[3], in order to compare the criteria with DECT results[2]. The main observation in the study was that urate deposits were detected by DECT less frequently in the 23 patients who fulfilled the provisional remission criteria (44%) than in the 129 patients who did not meet the criteria (74%)[2]. However, the fact that not every patient meeting the remission criteria had a negative DECT scan suggests, at first glance, that the criteria are not completely satisfactory.

The demonstration of urate deposits by DECT in patients fulfilling the remission criteria raises several issues, notably the potential effect of a persistent crystal load on musculoskeletal tissues and on cardiorenal outcomes[4]. However, owing to its cross-sectional nature, the study did not properly take into account the time during which the patients had met individual criteria for remission. Except for the lack of tophi, which did not require observation over time, and flare frequency during the past 12 months, which was recorded by patient interview, recording of the other individual criteria was insufficient: pain level, PGA and, most importantly, SUA level should have been recorded at least twice during a 12-month interval but were assessed only once. Strictly speaking, therefore, the study did not test the criteria as they had been defined.

A long observation period appears to be critical to defining remission. Persistence of urate deposits in patients treated with allopurinol was already shown in a previously published study of the cohort employed to test the remission criteria[3]. An important observation in this study[3] was that the longer a patient had been treated with allopurinol, the less often clinical examination detected tophi: patients without tophi had been treated for a mean of 5.80 (SD 7.58) years, compared with 3.80 (SD 4.64) years for those who still had palpable tophi.

Dissolution of MSU crystals can be achieved by ULT and several rheumatology societies have recommended a target SUA level of <360 μmol/l (REFS[5,6]), which can be estimated as the in vivo saturation concentration of uric acid[7] and is the value retained in the remission criteria[1]. However, dissolution of MSU crystals is a slow process that takes several months or even years, depending on the initial amount of crystals and the intensity of urate lowering[8]. The remission criteria article[1] highlighted this difficulty in defining remission and it appeared that consensus was not reached about the period of time during which the criteria, including the target SUA level (SUA < 360 μmol/l), had to be observed, although the authors determined that a 12-month period seemed reasonable but should be validated by future studies[1].

> Validation of a set of remission criteria for gout remains an important goal…

A longitudinal prospective study therefore seems to be necessary to resolve this difficult question. This suggested prospective study can be seen as presenting a real challenge, as it will require a large number of patients, a long follow-up period (at least 12 months, and preferably longer) and that patients do not receive anti-inflammatory treatment for a prolonged time during which the desirable SUA target is maintained and flares, pain and PGA of disease activity are assessed.

Validation of a set of remission criteria for gout remains an important goal, as these criteria would have multiple uses not only in clinical trials, but also in clinical practice to define the time when, once dissolution of MSU crystals has been achieved, the dose of urate-lowering drugs could be lowered to a dose that merely prevents new crystal formation, as recommended by the British Society for Rheumatology[9]. Dalbeth et al.[2] should therefore be commended for their attempt to solve this difficult issue, even though they didn't quite succeed in validating the remission criteria. Finally, disappearance of MSU crystals matters the most in defining gout remission, and whether remission criteria should include an imaging component to explore the remaining crystal load remains an open question.

Thomas Bardin[1,2,3]* *and Pascal Richette*[1,2]

[1]*Rheumatology department, Hôpital Lariboisière, Paris, France.*

[2]*Université de Paris, INSERM U 1132, Paris, France.*

[3]*French-Vietnamese Research Center and Gout and Chronic Disease, Vien Gut Medical Center, Ho Chi Minh City, Vietnam.*

**e-mail:* thomas.bardin@aphp.fr

https://doi.org/10.1038/s41584-019-0280-0

1. de Lautour, H. et al. Development of Preliminary Remission Criteria for Gout Using Delphi and 1000Minds Consensus Exercises. *Arthritis Care Res.* **68**, 667–672 (2016).
2. Dalbeth, N. et al. Concurrent validity of provisional remission criteria for gout: a dual-energy CT study. *Arthritis Res. Ther.* **21**, 150 (2019).
3. Dalbeth, N. et al. Presence of monosodium urate crystal deposition by dual-energy CT in patients with gout treated with allopurinol. *Ann. Rheum. Dis.* **77**, 364–370 (2018).
4. Richette, P. et al. Improving cardiovascular and renal outcomes in gout: what should we target? *Nat. Rev. Rheumatol* **10**, 654–661 (2014).
5. Khanna, D. et al. 2012 American College of Rheumatology guidelines for management of gout. Part 1: systematic nonpharmacologic and pharmacologic therapeutic approaches to hyperuricemia. *Arthritis Care Res.* **64**, 1431–1446 (2012).
6. Richette, P. et al. 2016 updated EULAR evidence-based recommendations for the management of gout. *Ann. Rheum. Dis.* **76**, 29–42 (2017).
7. Bardin, T. Hyperuricemia starts at 360 micromoles (6 mg/dL). *Joint Bone Spine* **82**, 141–143 (2015).
8. Perez-Ruiz, F. et al. Effect of urate-lowering therapy on the velocity of size reduction of tophi in chronic gout. *Arthritis Rheum.* **47**, 356–360 (2002).
9. Hui, M. et al. The British Society for Rheumatology Guideline for the Management of Gout. *Rheumatology* **56**, 1056–1059 (2017).

Competing interests
The authors declare no competing interests.

Cutaneous lupus erythematosus: new insights into pathogenesis and therapeutic strategies

Joerg Wenzel

Abstract | Cutaneous lupus erythematosus (CLE) is an autoimmune disease that can present as an isolated skin disease or as a manifestation within the spectrum of systemic lupus erythematosus. The clinical spectrum of CLE is broad, ranging from isolated discoid plaques to widespread skin lesions. Histologically, skin lesions present as interface dermatitis (inflammation of the skin mediated by anti-epidermal responses), which is orchestrated by type I and type III interferon-regulated cytokines and chemokines. Both innate and adaptive immune pathways are strongly activated in the formation of skin lesions owing to continuous re-activation of innate pathways via pattern recognition receptors (PRRs). These insights into the molecular pathogenesis of skin lesions in CLE have improved our understanding of the mechanisms underlying established therapies and have triggered the development of targeted treatment strategies that focus on immune cells (for example, B cells, T cells or plasmacytoid dendritic cells), as well as immune response pathways (for example, PRR signalling, Janus kinase (JAK)–signal transducer and activator of transcription (STAT) signalling and nuclear factor-κB signalling) and their cytokines and chemokines (for example, type I interferons, CXC-chemokine ligand 10 (CXCL10), IL-6 and IL-12).

Interface dermatitis
Cytotoxic, anti-epithelial inflammation at the dermo-epidermal junction, characterized by hydropic degeneration, keratinocytic cell death and colloid bodies

Department of Dermatology and Allergy, University Hospital of Bonn, Bonn, Germany.

e-mail: joerg.wenzel@ukbonn.de

https://doi.org/10.1038/s41584-019-0272-0

Lupus erythematosus is an autoimmune disease that has a large spectrum of manifestations ranging from skin lesions to systemic manifestations (systemic lupus erythematosus (SLE)). Cutaneous lupus erythematosus (CLE) can present as an isolated skin disease or as a manifestation within the spectrum of SLE[1–3]. CLE-specific cutaneous manifestations are characterized by clinical features (for example, a butterfly rash and ultraviolet (UV) light-induced skin lesions), serological features (for example, antinuclear antibodies (ANAs), particularly anti-SSA/Ro and anti-SSB/La antibodies) and histological features (for example, interface dermatitis alongside the expression of interferon-regulated chemokines)[1,3]. CLE-specific skin lesions can be subdivided into four subsets, based on clinical and histological features: acute CLE (ACLE), subacute CLE (SCLE), intermittent CLE (ICLE) and chronic CLE (CCLE)[4] (FIG. 1; Supplementary Fig. 1). In addition to these CLE-specific skin lesions, patients with CLE might also have other skin lesions that are not specific to this disease and that can present in any autoimmune disease, such as alopecia or vascular disorders[5].

In Europe and the USA, the incidence of isolated CLE is ~4 cases per 100,000 persons per year, which is slightly higher than the incidence of SLE (~3 cases per 100,000 persons per year)[6–9]. Skin involvement occurs in 70–80% of all patients with SLE during the course of their disease and skin lesions are the first disease manifestation to present in 20–25% of patients with SLE[8]. The involvement of internal organ systems can complicate CLE, irrespective of subtype. The rate of systemic manifestations depends on the underlying subtype of CLE; for example, ACLE has the highest rate of systemic involvement (~90%), whereas localized chronic discoid lupus erythematosus (CDLE) has the lowest (<5%)[7,10].

This Review provides an overview of the characteristic clinical and pathological findings in CLE and introduces the established standard therapies. Also discussed are new advances in our understanding of the molecular pathogenesis of CLE, as well as the emerging therapeutic strategies based on these new findings.

Skin lesions in CLE

Clinical classification

The clinical features and prognosis of CLE-specific skin lesions vary[4] (TABLE 1). ACLE can manifest as two main distinct forms: ACLE with localized, indurated erythematous lesions in the malar areas of the face (known as butterfly rash) or ACLE with widespread erythema, predominantly in sun-exposed areas of the skin (known as maculopapular rash). ACLE has a very close association with SLE (in that many patients develop systemic

Key points

- Cutaneous lupus erythematosus (CLE) occurs as isolated skin disease or in the context of systemic lupus erythematosus.
- Skin lesions in CLE are characterized by an interferon-orchestrated cytotoxic anti-epidermal immune response (known as interface dermatitis).
- Genetic variations in immune-regulation genes (such as genes involved in the type I interferon pathway, cell death, clearance of cell debris, antigen presentation, antibody production and immune cell regulation) predispose individuals to CLE.
- The chronic pathological cycle of CLE is fuelled by a continuous re-activation of innate immune pathways through adaptive effector mechanisms.
- Pharmacological inhibition of both adaptive and innate immune responses can be effective in the treatment of patients with CLE.
- New treatment strategies are being developed that mainly target type I interferon-producing cells (such as plasmacytoid dendritic cells) and their pathways (such as IFNAR or Janus kinase signalling).

disease) and is often accompanied by typical type I interferon-mediated general symptoms such as fever and fatigue. The close association of ACLE with SLE is also reflected by the high proportion of patients with ANAs (~80%) or anti-double-stranded DNA antibodies (30–40%)[7] (the distribution of subtypes are shown in Supplementary Figure 1).

SCLE can also occur as two major clinical forms: one characterized by papulosquamous or psoriasiform skin lesions, and the other by annular or polycyclic lesions. In both SCLE variants, skin lesions occur mainly in sun-exposed skin areas of the neck, shoulders, arms and/or legs, but not often the face. A high proportion of patients with SCLE have UV-associated autoantibodies (anti-SSA/Ro antibodies in 70–80% of patients and anti-SSB/La antibodies in 30–40% of patients), and between 20% and 30% of all patients with SCLE meet the criteria for systemic disease, for which the presence of nephritis and arthritis is common[1,7].

ICLE (also known as lupus erythematosus tumidus (LET)) is characterized by non-scarring and non-scaling skin lesions in sun-exposed areas of the skin, which present histologically with large clusters of plasmacytoid dendritic cells (pDCs) and mucin deposition[11]. Despite the high photosensitivity of patients with ICLE, anti-SSA/Ro and anti-SSB/La antibodies are rare (10–20% of patients) and patients with ICLE rarely develop systemic features of SLE (<5%)[7]. The classification of this subtype as a separate CLE subset is still under debate and ICLE has also been regarded as a subset of CCLE[12].

CCLE is characterized by a chronic clinical course (month to years) and a slow progression. The main CCLE variants are CDLE (which is the largest group (~50% of patients with CCLE)), lupus erythematosus profundus (also known as lupus erythematosus panniculitis or Kaposi–Irgang) and chilblain lupus erythematosus (ChLE). CDLE skin lesions are characterized by scarring erythrosquamous plaques accompanied by adherent scale formation, often with a disc-like (discoid) shape. CDLE can be localized (localized CDLE: affecting the skin of the head and face) or disseminated (disseminated CDLE: affecting the skin above and below the neck). CDLE might also present with extensive hyperkeratosis (hypertrophic CDLE). Only ~50% of all patients with CDLE are ANA-positive, and many patients develop systemic features of SLE (5–18% of patients)[1,6,7,13]. Lupus erythematosus profundus is a rare subtype of CCLE and involves lesions of the subcutaneous fat tissue[1,7] whereas ChLE is a rare acral variant of CCLE that typically affects the fingers, toes, ears and nose[1,7].

Other rare variants of CLE include bullous acute lupus erythematosus (characterized by subepidermal bullae), Rowell syndrome (with erythema multiforme-like target lesions), neonatal CLE (in newborn children) and mucocutaneous lupus erythematosus (with oral ulcers, plaques and/or discoid lesions)[14–16].

Histological features

CLE-specific skin lesions usually have a typical histological pattern, called interface dermatitis, which presents as an anti-epidermal immune reaction that includes the presence of cytotoxic CXC-chemokine receptor 3-positive (CXCR3$^+$) lymphocytes[17] and apoptotic or necroptotic keratinocytes (colloid bodies)[18,19]. In combination with clinical findings, histology therefore helps to establish the exact diagnosis in individual cases[20]. CLE skin lesions are characterized by a strong expression of interferon-regulated cytokines and chemokines[17], as well as the presence of two major type I and type III interferon producers: pDCs and keratinocytes[21–23]. Cytotoxic CXCR3$^+$ lymphocytes are recruited to the lesion via the corresponding chemokine CXC-chemokine ligand 10 (CXCL10), which is specifically expressed in the lower epidermis of active skin lesions, promoting keratinocytic cell death[24] (the main immunohistological features of CLE-specific skin lesions are shown in Supplementary Figure 2). The detection of a band of localized granular deposits of C3 and immunoglobulins (particularly IgG), known as a 'lupus band', by direct immunofluorescence can help to confirm a diagnosis of CLE in unclear clinical cases[25].

Other skin lesions

A large spectrum of cutaneous disorders exist that can occur in CLE as well as in the context of other autoimmune diseases (BOX 1; examples of these other skin lesions are shown in Supplementary Figure 3). In general, these lesions can be subdivided into two groups: vascular disorders, which include a wide spectrum of disorders ranging from dysfunction of single vessels to vascular ulcers, and disorders of the hair follicle (alopecia). Typical clinical manifestations are livedo racemosa, leukocytoclastic vasculitis, urticarial vasculitis, Raynaud phenomenon, vasculopathy, thrombophlebitis, periungual erythema and telangiectasia, fingertip necrosis and skin ulcers[26,27]. Diseases of the hair follicle include alopecia areata and telogen effluvium (known as lupus hair)[28].

Molecular pathogenesis of CLE

In genetically susceptible individuals, different environmental factors can activate innate and adaptive immune responses and induce the development of CLE skin lesions. In patients with CLE, skin lesions are characterized by an anti-epithelial cytotoxic immune response, which promotes the release of cell debris and in turn re-activates innate immune pathways, leading to a pro-inflammatory self-amplifying cycle (FIG. 2). At first,

Papulosquamous
A medium-sized (3–10 mm) elevated skin lesion with scaling

Psoriasiform
A 'psoriasis-like', well-circumscribed, elevated skin lesion with scaling

Annular
A ring-shaped skin lesion

Polycyclic
Skin lesions formed of several erythematous rings

Erythrosquamous
A red and scaling skin lesion

Bullae
Large blisters (>1 cm)

Target lesions
Annular skin lesions with similarity to an archer's bullseye with a central papule or vesicle, surrounded by pale oedema, and a peripheral ring-shaped erythema

Colloid bodies
Pale, hyaline residue material derived from dead keratinocytes seen in the lower epidermis and the upper dermis (also known as Civatte bodies)

autoantibodies were proposed to make a major contribution to this pathway; in this model, a primary trigger, such as UV light, causes keratinocytes to undergo cell death and present nuclear antigens on their surface, which are subsequently recognized by circulating autoantibodies[29]. This model explains the development of skin lesions and the photosensitivity in patients with pre-existing autoantibodies, but it is based on the assumption of pre-existing autoantibodies and fails to explain the pathogenesis in autoantibody-negative patients[3,30].

Particularly in solitary CDLE, which is characterized by a high proportion of autoantibody-negative patients, the pathogenetic function of autoantibodies and B cells is under discussion[31]. There is, however, strong evidence for a function of cytotoxic T cell-mediated immune reaction directed against the epidermis, as these cells can cause keratinocytic cell death and release of nuclear antigens[32–34]. In this context, B cells might function primarily as antigen-presenting cells that prime autoreactive T cell activation[35]. Moreover, some evidence suggests that keratinocytes themselves participate in the lesional self-perpetuating cycle by producing type I and III interferons and interferon-regulated pro-inflammatory cytokines and chemokines[21,22,31]. These observations have led to a broader pathogenetic model encompassing both adaptive and innate mechanisms (FIG. 2).

Genetic factors

CLE is a multifactorial disease that occurs within families and between twins, suggesting that genetic factors have a strong contribution[36]. To date, only one monogenetic variant of CLE has been identified: a rare familial ChLE variant characterized by a mutation in *TREX1*. TREX1 is a cytosolic DNase and deficiency of TREX1 leads to chronic hyperactivation of the type I interferon system via cytosolic DNA recognition pathways[37]. Moreover, several additional genetic associations, mutations and gene polymorphisms have been identified in different CLE populations[38] (TABLE 2). Most of these factors are functionally relevant, as they are involved in innate or adaptive immune responses, including the type I interferon pathway, cell death, clearance of cell debris, antigen presentation, antibody production and immune cell regulation.

Environmental factors

UV light is the most well-established provocation factor for CLE. Approximately 60–80% of patients with SLE have photosensitive skin lesions[7,39]. UV irradiation induces cellular damage resulting in pro-inflammatory responses, including cell death, the release of reactive oxygen species and distinct DNA modifications (such as an increase in the level of pro-inflammatory 8-hydroxyguanine (8-OHG), a marker of oxidative damage in DNA)[40]. In addition, UV light stimulates the release of pro-inflammatory factors from mast cells, which are increased in number within CLE skin lesions[41,42]. A disease-associated genetic background seems to be crucial for the development of skin lesions following UV exposure: in a prospective analysis, only patients with SLE and not healthy individuals developed CLE-like skin disease with a lesional type I interferon signature after UV provocation[43] and, importantly, UV irradiation upregulated interferon-related and MHC-related genes in the skin of patients with CLE but not in that of healthy individuals in a prospective gene expression study[44].

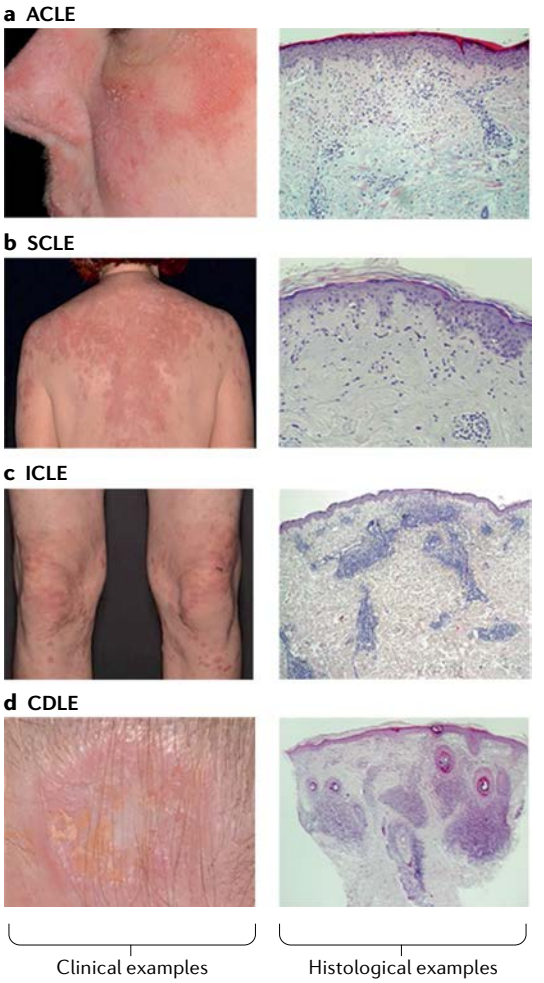

Fig. 1 | **Cutaneous lupus erythematosus subtypes.** Typical clinical and histological examples for the most common cutaneous lupus erythematosus (CLE) subsets: acute CLE (ACLE), subacute CLE (SCLE), intermittent CLE (ICLE) and chronic discoid lupus erythematosus (CDLE). **a** | Patients with ACLE typically have a butterfly rash on the face, and skin samples from these patients histologically show moderate interface dermatitis with some infiltrating neutrophils (magnification ×100). **b** | Non-scarring erythematosquamous lesions in sun-exposed skin are a typical feature of SCLE, which presents histologically as mild interface dermatitis (magnification ×100). **c** | ICLE presents clinically as non-scaling plaques in sun-exposed areas of the skin and histologically as patchy dermal infiltrates composed of lymphocytes and plasmacytoid dendritic cells (magnification ×50). **d** | Discoid lesions with central scarring are typically found in patients with CDLE, and histological samples show dense perifollicular and perivascular infiltrates combined with interface dermatitis and follicular plugging (magnification ×50).

Cigarette smoke is another important environmental factor for CLE[45]. In CLE, smokers have notably higher Cutaneous Lupus Erythematosus Disease Area and Severity Index (CLASI) scores than non-smokers,

Table 1 | **Subtypes of CLE**

Subtype of CLE	Variant	Key features
ACLE	Localized ACLE	Butterfly rash
	Disseminated ACLE	Maculopapular rash
	Bullous ACLE	Subepidermal blister
SCLE	Annular SCLE	Circular lesions
	Papulosquamous SCLE	Erythrosquamous lesions
	Rowell syndrome	Erythema multiforme-like target-shaped lesions
	Neonatal SCLE	SCLE in newborn children
ICLE	Lupus erythematosus tumidus	Plaques without squamae
CCLE	Chronic discoid lupus erythematosus	Localized or disseminated scarring lesions
	Hypertrophic chronic discoid lupus erythematosus	Extensive hyperkeratosis
	Lupus erythematosus profundus	Subcutaneous nodules
	Chilblain lupus erythematosus	Acral lesions
	Mucocutaneous CCLE	Oral plaques and ulcers

ACLE, acute CLE; CCLE, chronic CLE; CLE, cutaneous lupus erythematosus; ICLE, intermittent CLE; SCLE, subacute CLE.

and they need higher doses of immunoregulatory drugs to treat their disease[46]. Cigarette smoke can promote several pro-inflammatory processes involved in the pathogenesis of CLE, including neutrophil activation, neutrophil extracellular trap formation, cellular stress and apoptosis, thus fuelling disease activity[47].

Drug-induced SLE, which includes induction of CLE-like skin lesions, is a well-known adverse effect of several agents. Drugs traditionally associated with drug-induced SLE (for example, procainamide, hydralazine, quinidine and omeprazole) have been reported to directly activate the innate immune system or indirectly activate this system by inhibiting the clearance of autoantigens[48–50]. TNF-blocking agents can also induce SLE-like adverse effects (including the induction of CLE-like lesions)[51,52], which is probably because of the inhibition of the TNF-mediated regulation of the interferon system, leading to upregulation of interferon-associated pro-inflammatory factors and interferon-driven disease[53]. Recombinant type I interferons can also induce CLE-like skin lesions at the injection site, supporting a direct pathophysiological function of type I interferons in CLE[54]. Finally, immune stimulators such as checkpoint inhibitors have also been added to the list of potentially SLE-inducing drugs[55].

Gene expression patterns

The expression of type I interferon-regulated pro-inflammatory cytokines is a hallmark of CLE skin lesions[22,56]. Gene expression analyses have helped to form a detailed picture of the functional pathways activated in CLE skin lesions[21,22,57]. These analyses have revealed simultaneous activation of innate and adaptive immune pathways in the skin of patients with CLE[21,58] (FIG. 3). Genes encoding pro-inflammatory cytokines and chemokines are the most prominent subset within the innate pathways in CLE skin lesions. These pathways also include a large number of genes involved in DNA recognition and RNA recognition accompanied by genes involved in cell death pathways and complement activation. Genes relating to adaptive immune pathways include those involved in leukocyte migration, T cell and B cell activation, and antigen presentation. Gene expression signatures of CLE are also closely associated with not only other autoimmune diseases (such as SLE, rheumatoid arthritis, thyroid disease and inflammatory bowel disease) but also with type I interferon-mediated anti-viral responses (for example, responses to herpes simplex or influenza) and anti-epithelial disorders (for example, graft-versus-host disease and allograft reaction)[21], supporting the classification of CLE as an interferon-driven, cytotoxic autoimmune disease[59].

Molecular insights from mouse models

The contribution of cytotoxic interferon-associated inflammation, driven by innate immune mechanisms, in the pathogenesis of CLE is supported by findings in mouse models. The number of type I interferon-producing pDCs is increased in UV-induced skin lesions in lupus-prone MRL/lpr mice compared with non-lesional skin[60]. The mice also develop skin lesions after injection of IgG immune complexes[61]. Furthermore, activation of the innate immune response via Toll-like receptor 7 (TLR7) agonists aggravates skin disease in these mice, whereas inhibitors of the downstream pathway molecule MyD88 improve the skin condition[62].

In *Tlr9*$^{-/-}$ mice, the pro-apoptotic FAS ligand promotes CLE-like, interferon-driven skin inflammation, which notably improves following treatment with the anti-IFNAR1 antibody MAR1-5A3 (REF.[63]). CLE-like skin inflammation is also increased in *Trex1*$^{-/-}$ mice[21,64], and in mice with a mutated form of Janus kinase 1 (JAK1) that leads to increased activation of the JAK–signal transducer and activator of transcription (STAT) pathway[65].

Activation of innate immune pathways

Immune complexes can activate receptors of the innate immune system and can contribute to CLE pathogenesis. For example, immune complexes of autoantibodies with RNA and/or DNA can be taken up by pDCs via CD32-mediated endocytosis[66]; the nucleic acid components of these immune complexes activate type I interferon production via binding to TLR7 or TLR9 in the endosome[66–68]

Box 1 | **Non-specific CLE skin lesions**[14,15]

Skin lesions that can occur in cutaneous lupus erythematosus (CLE) but are not specific to this disease:

- Cutaneous vascular inflammation
  - Livedo racemosa
  - Leukocytoclastic vasculitis, purpura and urticarial vasculitis
  - Raynaud phenomenon
  - Vasculopathy
  - Thrombophlebitis
  - Periungual telangiectasia
  - Oral ulcers
- Alopecia
  - Alopecia areata
  - Telogen effluvium

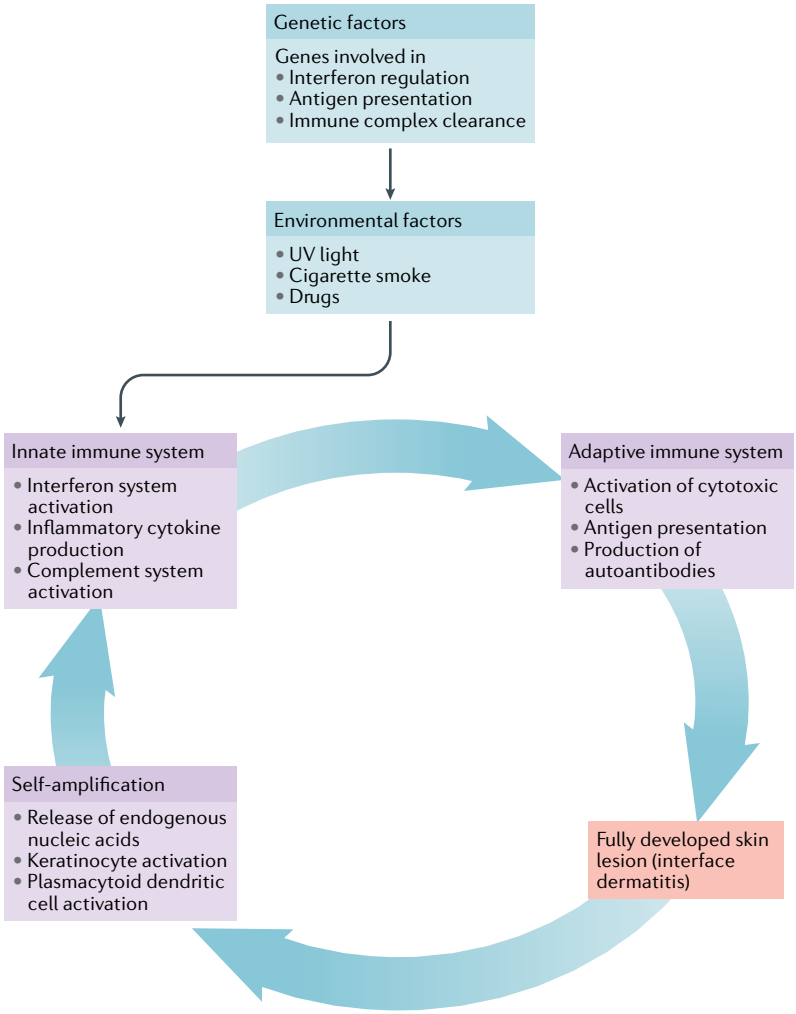

Fig. 2 | **Pro-inflammatory cycle within CLE lesions.** Against the background of predisposing genetic factors, distinct environmental factors, most notably ultraviolet (UV) light, activate innate immune responses. Activation of the innate immune system leads to subsequent activation of adaptive immune responses and the development of cutaneous lupus erythematosus (CLE) skin lesions. These skin lesions are characterized by anti-epithelial cytotoxic inflammation, called interface dermatitis, which provides a self-amplification loop: cellular stress and cell death cause the release of autoantigens and immunostimulatory endogenous nucleic acids that reactivate innate immune responses via pattern recognition receptors.

(FIG. 4). This mechanism could explain the continuous reactivation of the innate immune system in pDCs by adaptive immune mechanisms in CLE, which leads to the parallel activation of both arms of the immune system[69].

This hyperactivation of the innate immune pathways promotes lesional inflammation and also induces upregulation of CLE-typical autoimmune nuclear autoantigens, including SSA/Ro52 (which are interferon-inducible proteins)[70]. These autoantigens are recognized by adaptive immune mechanisms, resulting in the induction of autoantigen-specific cytotoxic T cells and autoantibodies produced by plasma cells. This process, however, might not explain how keratinocytes (which are crucial to the development of CLE skin lesions) contribute to the development of CLE skin lesions, and many patients with CLE lack autoantibodies[7]. Moreover, keratinocytes, as classical non-immune cells, have a different expression pattern of pattern recognition receptors (PRRs) and respond particularly to (TLR-independent) ligands that bind to cytosolic PRRs[71,72].

Lesional pathways

Keratinocytes participate in lesional inflammation in CLE by producing type I and type III interferons, particularly IFNκ and IFNλ, and interferon-regulated pro-inflammatory cytokines and chemokines (such as CXCL10)[21–23]. These interferons promote an autocrine feedback loop that increases the capacity of lesional keratinocytes to produce pro-inflammatory cytokines, including IL-6 (REF.[73]). UV light upregulates the expression of autoantigens such as Ro52 in keratinocytes and activates several pro-inflammatory pathways[2,74]. Morphologically, UV irradiation induces the expression of immunogenic 8-OHG nucleic acid motifs, together with the expression of pro-inflammatory cytokines, and promotes keratinocytic cell death within the whole epidermal layer[75]. In established lesions, however, this morphological pattern changes completely: dying cells and pro-inflammatory chemokines, particularly CXCL10, are found exclusively at the dermo-epidermal junction in inflamed areas, reflecting CLE-typical interface dermatitis[17]. These pro-inflammatory chemokines (including the CXCR3 ligands CXCL9, CXCL10 and CXCL11) initiate the recruitment of cytotoxic type I immune cells to the lesion via CXCR3 (REF.[76]), which supports lesional keratinocytic cell death, most probably via keratinocyte necroptosis[19]. The dying cells release debris including endogenous immunostimulatory nucleic acids, which can activate innate immune pathways in lesional keratinocytes via different PRRs (including MDA5, RIG-I and cGAS–STING)[21]. Immunostimulatory nucleic acid motifs from dying keratinocytes can accumulate within CLE lesions because of defects in phagocytic or enzymatic DNA clearance (for example, because of genetic or pharmaceutical predisposing factors)[50,77]. These endogenous immunostimulatory nucleic acid motifs can function as ligands for PRRs, and can drive interferon responses (for example, via the cGAS–STING pathway)[21,40,78,79] and activate the inflammasome (most probably via AIM2)[80,81]. 8-OHG-DNA and other DNA motifs are detectable in the cytosol of keratinocytes of patients with CLE, supporting the function of non-TLR cytosolic receptors in these cells in CLE[21]. Extracellular nucleic acid motifs are able to reach the cytosol by lipofection mediated by the antimicrobial peptide cathelicidin, which is present in CLE skin lesions and can function as an endogenous lipofection vector[21,82,83]. The identification of these lesional pathways and the molecular mechanisms of CLE increases the understanding of the function of established treatments in CLE and opens the door to targeted therapy strategies.

Treatment of CLE

Established therapies and guidelines

To date, no drug has been approved specifically for the treatment of CLE. Therefore, established therapeutic strategies are mainly based on a low level of evidence. Existing guidelines focus on the use of topical agents, anti-malarial drugs, glucocorticoids and classic immunosuppressive drugs for the treatment of CLE[25,84,85].

Topical treatment: sunscreen and topical immunosuppressive drugs. As UV light is one of the most important triggers for CLE skin lesions[7], effective sunscreen is vital. Broad-spectrum liposomal sunscreen can prevent the development of skin lesions in patients with CLE[43,86]. Moreover, the use of sun-blocking agents also decreases the expression of type I and type III interferons and associated cytokines and chemokines (such as CXCL10) in the skin, thus reducing systemic inflammation in these patients[75].

Table 2 | **Genetic associations with CLE**

Gene (polymorphism)	Disease association	Potential function	Refs
CLE			
TRIM39–RPP21	CLE	Interferon pathway, DNA damage and cell death	160
MICA	CLE	Cell death	160
MICB	CLE	Cell death	160
MSH5	CLE	DNA repair	160
HLA-DR2 and *HLA-DR3*	CLE	Antigen presentation	160
PSORS1C1	CLE	Unknown function (confers susceptibility to autoimmunity)	160
MUC21	CLE	Mucin glycoprotein	160
CSNK2B	CLE	Ubiquitous protein kinase involved in various signalling cascades	160
FLOT1	CLE	Vesicle trafficking	160
MAS1L	CLE	Modulator of angiotensin responses	160
SCLE			
TNF (308A)	SCLE	Pro-inflammatory cytokine	161
IRF5	SCLE	Interferon pathway	162,163
CCLE			
TYK2	CDLE	Interferon pathway	163
IRF5	CDLE	Interferon pathway	162,163
STAT4	CDLE	Interferon pathway	164
Genes encoding complement components C1q, C1r, C1s, C2 and C4	CDLE	Clearance of cell debris	165–168
ITGAM	CDLE	Leukocyte migration and clearance of cell debris	169,170
CTLA4	CDLE	Immune checkpoint	163
TREX1	Familial chilblain lupus erythematosus	Interferon pathway	37
SLE			
IRF5	Skin disease in SLE	Interferon pathway	162,163
STK17A	Skin disease in SLE	Interferon pathway and cell death	171
LY9	Skin disease in SLE	Lymphocyte function	162
IL21	Skin disease in SLE	Cytokine that can increase antibody production	162
VDR	Skin disease in SLE	Immune regulation	172
UBE2L3	Skin disease in SLE	NF-κB signalling and plasma cell development	162
FCGR2A	Discoid rash in SLE	Clearance of cell debris and cell death	169
ITGAM	Discoid rash in SLE	Leukocyte migration and clearance of cell debris	169,170
TNFAIP3	Malar rash in SLE	Regulation of NF-κB signalling and cell death	173
FCGR3B	Malar rash in SLE	Clearance of cell debris and cell death	174
IFNK	Discoid and malar rash in SLE (and CLE)	Interferon pathway	175

CCLE, chronic CLE; CDLE, chronic discoid lupus erythematosus; CLE, cutaneous lupus erythematosus; NF-κB, nuclear factor-κB; SCLE, subacute CLE; SLE, systemic lupus erythematosus.

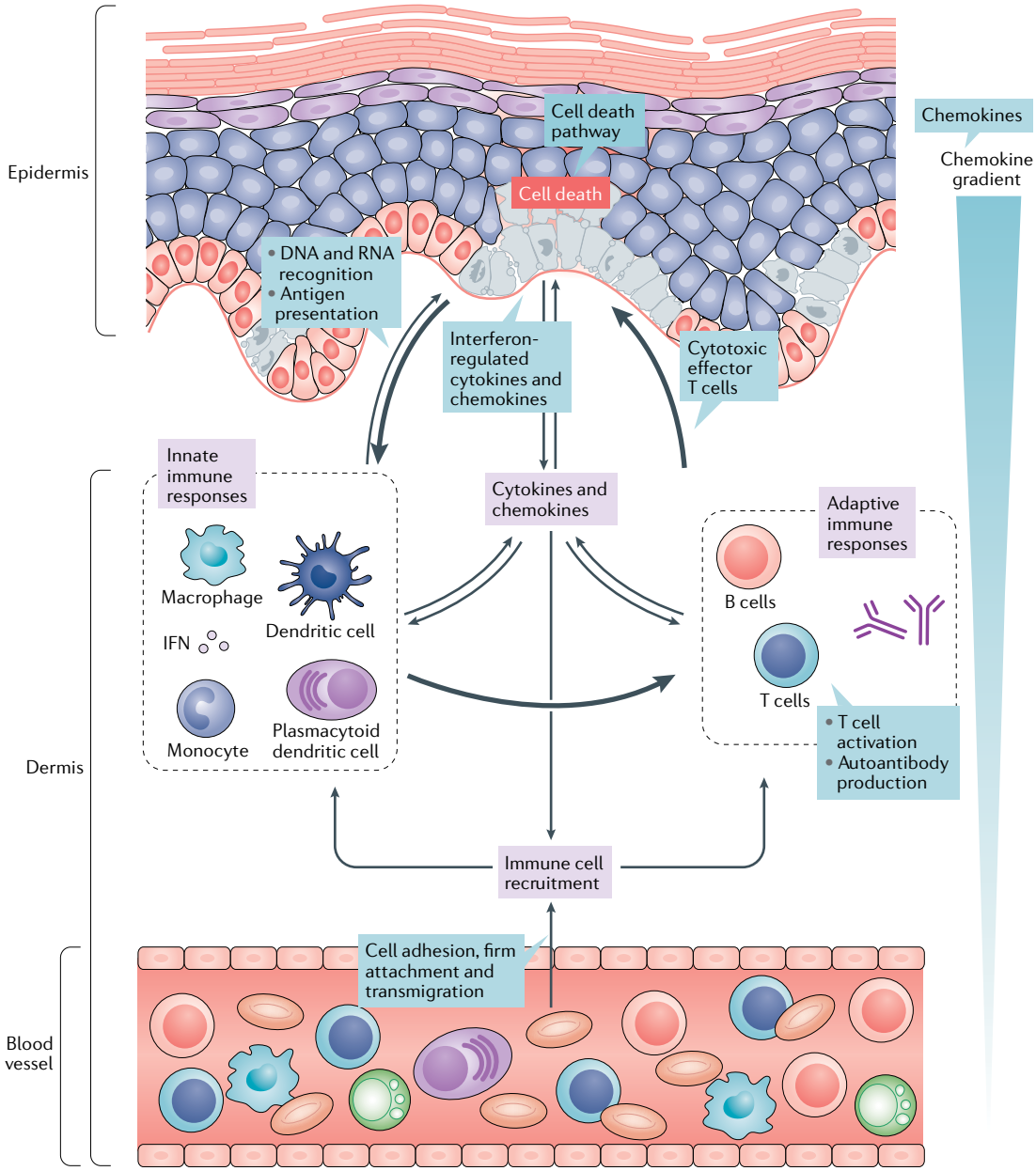

Fig. 3 | **Overview of pro-inflammatory pathways within CLE lesions.** Gene expression analyses have identified multiple immunological markers that are simultaneously expressed in different parts of the cutaneous lupus erythematosus (CLE) skin lesions during active inflammation[21,58]. The figure depicts the complex network of different immune cell types, including T cells, B cells, plasmacytoid dendritic cells and macrophages, highlighted by such analyses; interactions between these cells are orchestrated by a large number of interferon (IFN)-regulated cytokines and chemokines, particularly CXC-chemokine ligand 10 (CXCL10). These pro-inflammatory mediators regulate the adhesion of cells to skin vessel walls and their migration towards the epidermis via a chemokine gradient. Cytotoxic effector cells attack lesional keratinocytes, resulting in keratinocytic cell death as well as the expression of pro-inflammatory cytokines and the release of pro-inflammatory chemokines, overall fuelling the lesional inflammation.

Topical glucocorticoids are the first-line treatment for CLE lesions because of their anti-inflammatory properties[25,45]. The primary indication for topical glucocorticoids is a localized CDLE, but patients with widespread CDLE lesions and other CLE subsets also benefit from topical immunosuppression as an add-on to systemic treatment[85]. Topical calcineurin inhibitors (such as tacrolimus ointment and pimecrolimus cream) are not approved for the treatment of CLE, but are the most established therapeutic alternative to corticosteroids in CLE[25,45]. Unlike corticosteroids, these inhibitors do not induce skin atrophy as an adverse effect, but they are also less effective than corticosteroids[87].

Established systemic treatment in CLE. In current guidelines, antimalarial drugs and glucocorticoids are both recommended as first-line treatment in patients with highly active or widespread lesions[25,84,85]. Antimalarial

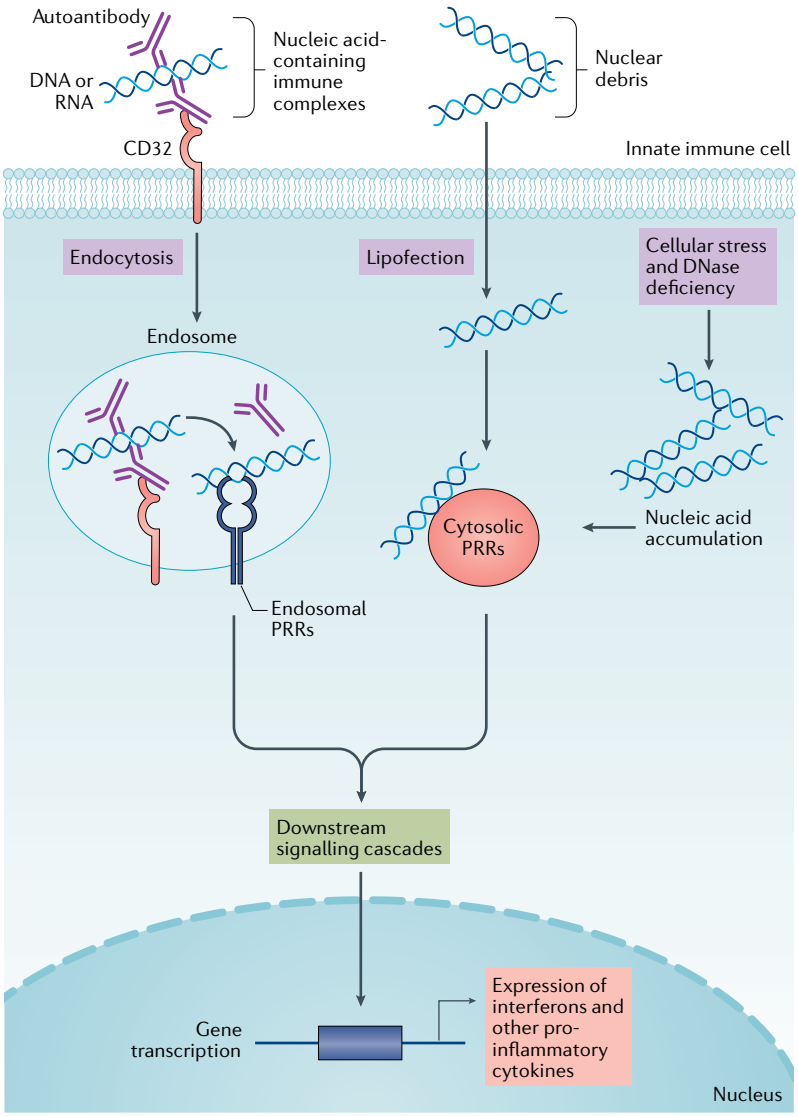

Fig. 4 | **Model for the reactivation of innate pathways in CLE.** Different mechanisms have been shown to be responsible for the chronic reactivation of the innate immune system in cutaneous lupus erythematosus (CLE). These mechanisms are not cell-type-specific and can involve classical immune cells as well as non-immune cells. Immune complexes of nucleic acid motifs and autoantibodies bind to cells via CD32 and activate type I and type III interferon-producing pathways via endosomal Toll-like receptors (such as TLR3, TLR7 and TLR9). This mechanism is particularly important for plasmacytoid dendritic cells. Endogenous nucleic acids, which are released following lesional cell death, can enter a cell by lipofection via natural compounds (such as via the cathelicidin antimicrobial peptide) and induce interferon-producing pathways by activating cytosolic pattern recognition receptor (PRRs), including the cGAS–STING pathway. In specific situations (for example, during cellular stress or DNase deficiency), nucleic acids can accumulate within the cytosol and activate cytosolic PRRs directly. This mechanism is most important in familial chilblain lupus systematosus, which is caused by deficiency in the cytosolic DNase TREX1. Signalling via ubiquitous cytosolic PRR pathways can activate keratinocytes in CLE.

drugs (such as chloroquine, hydroxychloroquine and quinacrine) are the most frequently used systemic drugs in CLE: about 80% of all patients with active CLE were reported to receive either chloroquine or hydroxychloroquine in a large European cohort of >1,000 patients[64]. The mode of action of antimalarial drugs is still under investigation, but all of these antimalarial drugs inhibit type I interferon production by immune-activated peripheral blood mononuclear cells[88]. For chloroquine and hydroxychloroquine, evidence suggests two main mechanisms underlying the therapeutic effects of these drugs in CLE: the inhibition of antigen presentation by dendritic cells and the direct binding of immunostimulatory nucleic acid motifs[89,90]. By contrast, quinacrine inhibits TLR-mediated production of TNF and IL-6 by immune cells[88,91].

The use of systemic glucocorticoids is recommended in severe or widespread active CLE lesions, but should be tapered as soon as possible to minimalize adverse effects[25]. Because of the adverse effects of sun protection (decreased vitamin D production) and corticosteroids (enhanced risk of osteoporosis), the European Academy of Dermatology and Venereology guidelines recommend vitamin D supplementation for all patients with CLE[25].

In patients with long-standing disease or high disease activity the use of other immunosuppressive and immunomodulatory drugs might be indicated[45]. Methotrexate, retinoids and dapsone are considered as second-line treatments[25]. Methotrexate is recommended for use in refractory CLE, primarily SCLE[92], dapsone for recalcitrant CLE and bullous lupus erythematosus[93], and retinoids for selected patients with CLE (particularly patients with hypertrophic CDLE) when they are unresponsive to other treatments[94]. All other drugs, including mycophenolate mofetil and cyclosporine, are currently regarded as third-line therapies because of the lack of clinical studies in CLE[25].

Most of the second-line and third-line therapies are corticosteroid-sparing drugs and inhibit the proliferation of T cells and B cells, but these drugs also have additional effects that might support their efficacy in CLE[45,85]. For example, methotrexate not only downregulates the expression of several adhesion molecules that promote lymphocyte migration into the skin but also reduces antigen presentation, blocks activation of neutrophilic granulocytes[95] and inhibits the JAK–STAT pathway[96].

Targeted therapy strategies in CLE

In parallel to the growing knowledge about the molecular mechanisms within the past decade, several biologic drugs and other targeted drugs have been introduced into the treatment of CLE or are currently being tested in clinical and preclinical studies (TABLE 3). These drugs target either immune cells, particularly B cells and T cells but also pDCs, or pro-inflammatory mediators[97–99] (FIG. 5).

Therapies targeting B cells. B cells, plasma cells and their activation pathways were an early focus of targeted treatment strategies in CLE because of their function in the production of autoantibodies[99]. The first of these studies was performed with rituximab, an anti-CD20 B cell-depleting antibody. Despite rituximab showing some effect on CLE disease activity in initial studies[100], larger studies failed to support the efficacy of this drug in most subtypes of CLE[101]. In specific CLE subsets (including ACLE and bullous lupus erythematosus), rituximab was reported to be effective[99], but the drug also induced new-onset CDLE and SCLE in patients with SLE[102].

Belimumab is a monoclonal antibody against B cell-activating factor (BAFF, also known as BlyS) that

Table 3 | **Ongoing clinical studies in CLE**

Drug name	Mechanisms	Conditions	Phase	Refs
Targeting immune cells				
Hydroxychloroquine	DNA-binding agent	CLE	IV	176
Thalidomide	Immunosuppressive drugs	SLE	IV	176
Fluocinonide (0.05% cream)	Glucocorticoid	CLE	IV	177
Nicotinamide	Anti-inflammatory supplement (amide form of vitamin B_3)	SLE and CLE	II	178
Targeting B cells and T cells				
Belimumab	Anti-BAFF antibody	SLE and CLE	III	105
Autologous polyclonal regulatory T cells	Immunoregulatory cellular therapy	CLE	I	179
Targeting pDCs				
BIIB059	Anti-CD303 antibody	SLE and CLE	II	124
VIB7734	Anti-LILRA4 antibody	SLE and CLE	I	126
Targeting the JAK–STAT pathway and other signalling pathways				
Filgotinib	JAK1 inhibitor	CLE	II	139
BMS-986165	TYK2 inhibitor	SLE and CLE	II	180
Tofacitinib	JAK1 and JAK3 inhibitor	SLE and CLE	II	181
Lanraplenib	SYK inhibitor	CLE	II	139
GSK2646264 (cream)	SYK inhibitor	CLE	I	144
Targeting cytokines				
Ustekinumab	IL-12 and IL-23 inhibitor	SLE and CLE	III	182
Etanercept	TNF inhibitor	CLE	II	153
Secukinumab	Anti-IL-17 antibody	CLE	II	183
Anifrolumab	Anti-IFNAR1 antibody	SLE and CLE	II	184

BAFF, B cell-activating factor; CLE, cutaneous lupus erythematosus; JAK, Janus kinase; LILRA4, leukocyte immunoglobulin-like receptor subfamily A member 4; pDC, plasmacytoid dendritic cell; SLE, systemic lupus erythematosus; STAT, signal transducer and activator of transcription; SYK, spleen tyrosine kinase; TYK2, non-receptor tyrosine-protein kinase TYK2.

was approved for the treatment of SLE by the FDA in 2011 (REF.[99]). The original registration trial in SLE did not include a specific skin score as an outcome, but several case reports and case series have suggested a positive effect of belimumab in CLE[103,104]. The efficacy of belimumab in CLE is also currently being investigated in a phase III clinical trial[105]. BAFF is one of the interferon-regulated cytokines produced by keratinocytes in CLE after stimulation of PRRs and might therefore have an important function in the feedback loop between innate and adaptive immune systems in lesional skin[106].

Atacicept, a TACI-Fc fusion protein that binds to BAFF and TACI, can reduce the severity of flares in patients with SLE and high disease activity, but data on CLE are still lacking[107]. Several other agents that deplete B cells (for example, the humanized anti-CD19 antibody obexelimab (also known as XmAb5871); the anti-CD20 antibodies obinutuzumab and ocrelizumab; and the anti-CD22 antibody epratuzumab) or inhibit B cell activation (for example, the anti-BAFF antibody tabalumab; the bispecific molecule AMG 570 that targets both ICOSL and BAFF; and the TACI antibody fusion protein RC18) are currently under investigation in clinical trials for SLE and might also provide new insights for the treatment of skin lesions[98].

Proteasome inhibitors target plasma cells, which are the source of autoantibodies in SLE and CLE. Two of these drugs, bortezomib and ixazomib, have been investigated in recent clinical trials on SLE and are still under investigation[108,109]. These drugs might be an option for refractory SLE, but need to be combined with targeted B cell therapies for sustained responses[110]. The potential benefit of these drugs in CLE is controversial, as some evidence suggests that a possible adverse effect of bortezomib might be the development of CLE-like lesions[111].

Therapies targeting T cells. SLE has traditionally been classified as a B cell-mediated disease because of its characteristic autoantibody production[33]. B cells, however, need T helper cells to become activated[112]. Effector T cells are responsible for most of the direct cell damage in SLE, and defects of regulatory T cells seem to be responsible for disease progression in many patients[33]. These data suggest T cells as potential targets in SLE[99,113].

Calcineurin inhibitors suppress T cell activation and among these inhibitors, cyclosporine has been used to treat recalcitrant CLE for decades[114]. However, placebo-controlled studies are not available and the use of this drug is limited by its adverse effects (for example, nephrotoxicity and hypertension) and pharmacodynamical variabilities[115]. Cyclosporin is therefore not recommended for the treatment of patients with CLE without systemic organ involvement in current guidelines[25]. Voclosporin, a calcineurin inhibitor with greater metabolic stability than cyclosporin, is effective in treating lupus nephritis, and could also be a potential drug to test in future trials of CLE[116]. In SLE, defects in regulatory T cells lead to unchecked immune responses[113]. The administration of low-dose IL-2 might have the capacity to correct these regulatory T cell defects[117] and is currently under investigation for the treatment of SLE[118] (although the relevance for CLE is as yet unclear).

Targeting B cell and T cell costimulatory molecules. B cells and T cells are co-activated by distinct pairs of stimulatory receptors and their corresponding ligands. Several inhibitors of these receptors or ligands have been investigated in clinical trials or are still under investigation in SLE (for example, BI655064 (an anti-CD40 antibody)[119] and dapirolizumab pegol[120] (a pegylated anti-CD40 ligand Fab′ fragment))[98], and might also be effective in CLE. Abatacept is a CTLA4–IgGFc1 fusion protein that inhibits T cell activation, and is beneficial in treating some patients with refractory SLE[121]. This drug, however, is also reported to induce SCLE in individual cases[122]. The mechanisms behind this reverse phenomenon are unclear, but it might be because of the formation of autoantibodies against the CTLA4 portion of the abatacept molecule during treatment, which directly stimulates T cells in vivo and promotes the autoimmune process[122].

Targeting plasmacytoid dendritic cells. pDCs are the most important cell type of the innate immune system in CLE. These cells are the main producers of type I interferons in the blood and skin lesions and amplify lesional inflammation[68]. In the tissue, pDCs can be

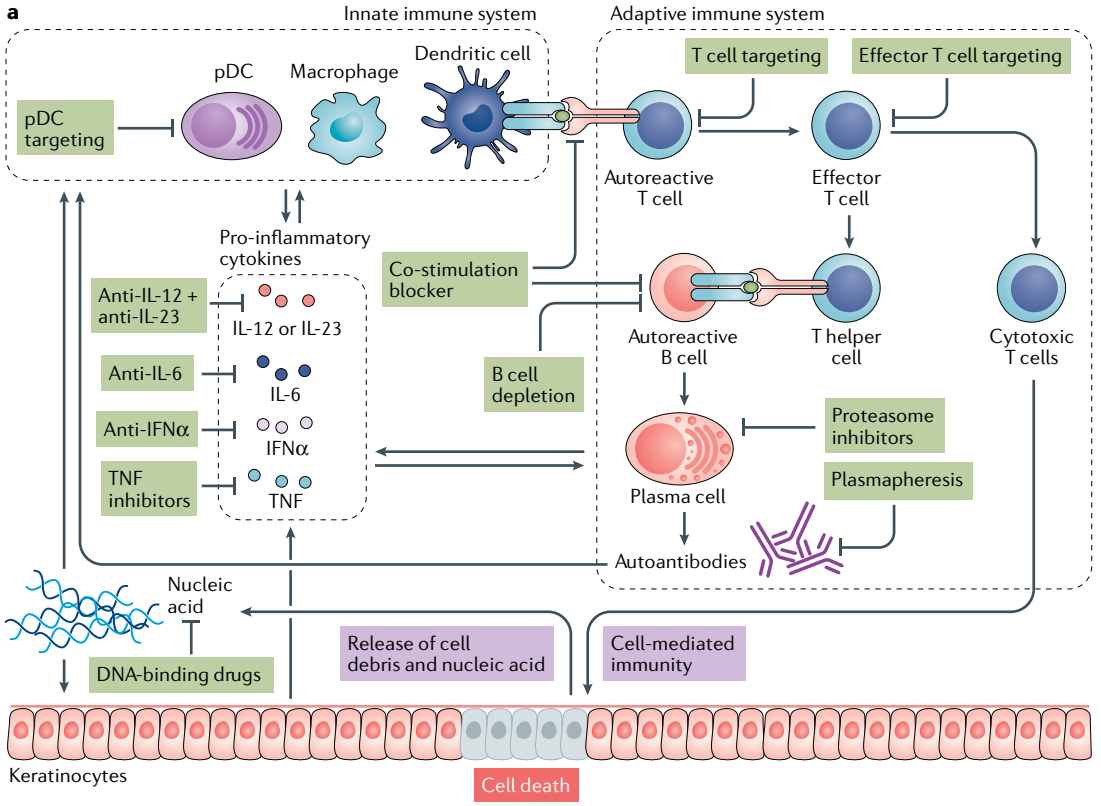
a
Innate immune system
Adaptive immune system
pDC
Macrophage
Dendritic cell
pDC targeting
T cell targeting
Effector T cell targeting
Autoreactive T cell
Effector T cell
Pro-inflammatory cytokines
Co-stimulation blocker
Anti-IL-12 + anti-IL-23
IL-12 or IL-23
Anti-IL-6
IL-6
Anti-IFNα
IFNα
TNF inhibitors
TNF
B cell depletion
Autoreactive B cell
T helper cell
Cytotoxic T cells
Proteasome inhibitors
Plasma cell
Plasmapheresis
Autoantibodies
Nucleic acid
DNA-binding drugs
Release of cell debris and nucleic acid
Cell-mediated immunity
Keratinocytes
Cell death

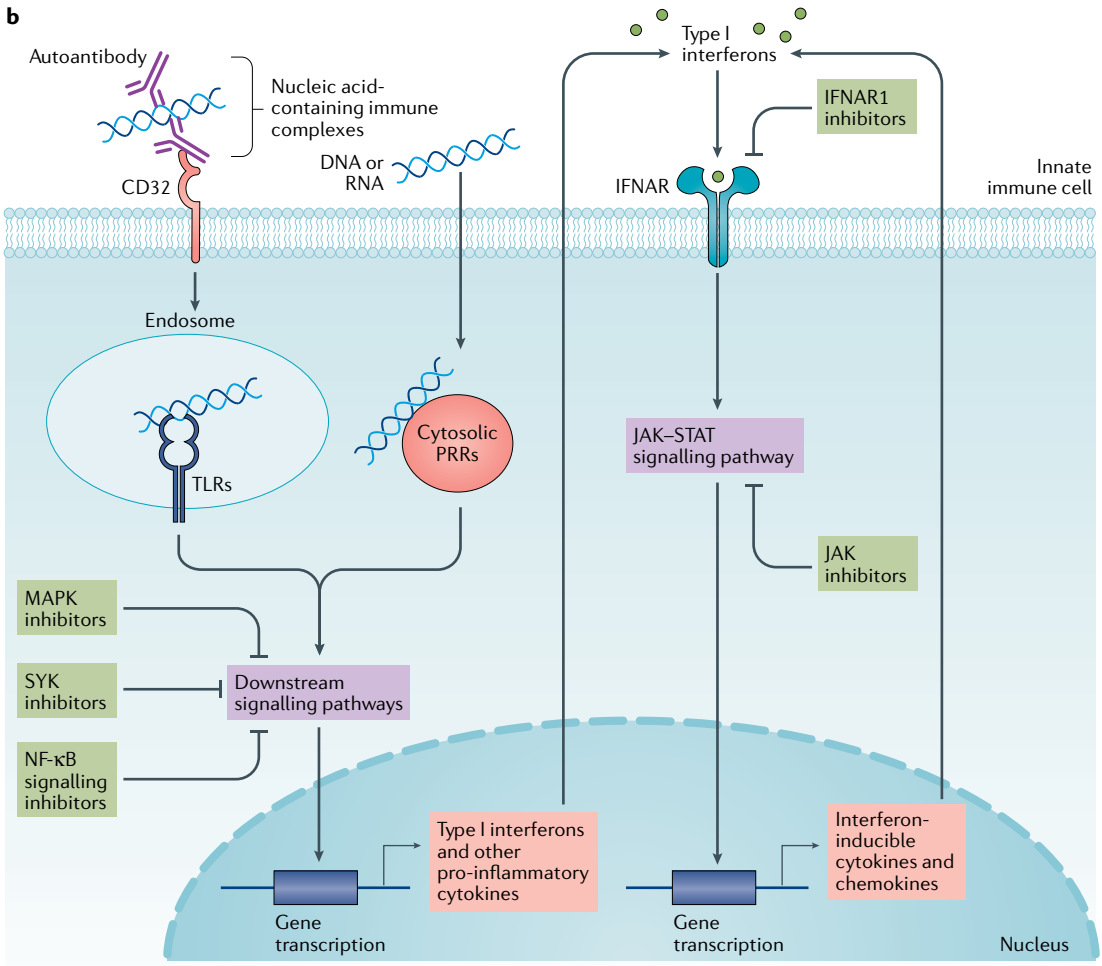
b
Autoantibody
Nucleic acid-containing immune complexes
CD32
DNA or RNA
Type I interferons
IFNAR1 inhibitors
IFNAR
Innate immune cell
Endosome
TLRs
Cytosolic PRRs
JAK–STAT signalling pathway
JAK inhibitors
MAPK inhibitors
SYK inhibitors
NF-κB signalling inhibitors
Downstream signalling pathways
Type I interferons and other pro-inflammatory cytokines
Interferon-inducible cytokines and chemokines
Gene transcription
Gene transcription
Nucleus

Fig. 5 | **Therapeutic targets in CLE.** Overview of the pro-inflammatory pathways of cutaneous lupus erythematosus (CLE) skin lesions and potential therapeutic targets. **a** | Potential therapies include those that target adaptive immune responses, such as B cell-depleting drugs (such as rituximab and belimumab); T cell-targeting drugs (such as voclospririne); inhibitors of B cell and/or T cell activation (for example, the anti-CD40 antibody BI655064, the anti-CD40 ligand antibody dapirolizumab, the anti-ICOS ligand AMG 557 and anti-malarial drugs); proteasome inhibitors (such as bortezomib and ixazomib); drugs that inhibit effector T cells (for example, methotrexate); and plasmapheresis (removal of antibodies from the plasma). Drugs that target innate immune cells, including plasmacytoid dendritic cells (pDCs; for example, BIIB059), are also promising. Another strategy is to target cytokines, such as with anti-IFNα antibodies (for example, sifalimumab and rontalizumab), anti-IFNAR1 antibodies (such as anifrolumab), IL-12 and IL-23 inhibitors (such as ustekinumab), IL-6 inhibitors (such as PF-04236921, sirukumab, MRA003US and vobarilizumab) and TNF inhibitors (such as etanercept and infliximab). Some drugs can bind to DNA (such as antimalarial drugs), which might contribute to their efficacy. **b** | Downstream pathways can also be targeted, such as with inhibitors of the Janus kinase (JAK)–signal transducer and activator of transcription (STAT) pathway (such as ruxolitinib, baricitinib, tofacitinib, filgotinib, BMS-986165 and methotrexate); inhibitors of nuclear factor-κB (NF-κB) signalling (such as iguratimod); mitogen-activated protein kinase (MAPK) inhibitors (such as SB203580 and FR167653); and inhibitors of spleen tyrosine kinase (SYK; such as lanraplenib and GSK2646264). PRR, pattern recognition receptor; TLR, Toll-like receptor.

identified by the expression of their specific receptor CD303 (also known as BDCA2). This receptor, which regulates the production of type I interferons, is the target structure of BIIB059, a monoclonal antibody developed for the treatment of SLE[123]. The efficacy of this drug in CLE is currently under investigation in an ongoing clinical trial[124], with initial results indicating that BIIB059 treatment results in a decline in CLASI activity score[125]. A new phase I trial is also investigating the efficacy of targeting pDCs in CLE and related autoimmune diseases using VIB7734 (formerly known as MEDI-7734)[126]. VIB7734 is a monoclonal antibody against leukocyte immunoglobulin-like receptor subfamily A member 4 (LILRA4, also known as ILT7) that specifically targets pDCs.

Targeting the type I interferon system. Given that a strong type I interferon signature is a hallmark of SLE, interferons (especially IFNαs and IFNβ) and their common receptor (IFNAR) have been a major target in SLE drug development over the past decade. Initial studies focused on targeting IFNα, but the specific anti-IFNα antibodies (for example, sifalimumab and rontalizumab) had only a limited effect on CLE skin lesions, possibly because of the high redundancy of the different type I interferons[22,127,128]. The anti-IFNγ antibody AMG 811 had no notable clinical effect on patients with CDLE[129]. Targeting IFNAR seems to be more effective than targeting the cytokines themselves: the anti-IFNAR1 antibody anifrolumab reduced the CLASI score in patients with SLE in a phase IIb clinical study[130].

Targeting the JAK–STAT pathway. The JAK–STAT pathway is crucial for the autocrine loop of type I interferons and is located upstream of important CLE-associated pathogenic pro-inflammatory cytokines and chemokines, including CXCL10 (FIG. 5). JAK inhibitors were initially developed for the treatment of haemato-oncological diseases caused by JAK mutations, in which these inhibitors (particularly ruxolitinib) had considerable immunosuppressive effects[131]. First clinical observations suggesting a potential efficacy of JAK inhibitors in immunological diseases closely related to CLE were reported for graft-versus-host disease[132] and dermatomyositis[133,134]. The JAK1 and JAK2 inhibitor ruxolitinib improved skin lesions in both conditions. Ruxolitinib inhibits the expression of pro-inflammatory mediators characteristic of CLE (such as CXCl10 and CXCL11) in vitro in keratinocytes and was also effective in treating skin lesions of a patient with ChLE[135,136]. The JAK1 and JAK3 inhibitor tofacitinib was also effective in the treatment of another patient with ChLE[64], and this inhibitor is now under investigation in a clinical trial for the treatment of CDLE[137]. Treatment with baricitinib, another JAK1 and JAK2 inhibitor, improved the proportion of patients with SLE achieving resolution of arthritis or rash, as measured by the SLE Disease Activity Index 2000 score, in a phase II trial; however, this effect was mainly caused by amelioration of arthritis, whereas skin severity (as measured by the CLASI) did not improve[138]. Currently, the JAK1 inhibitor filgotinib is under investigation in a phase II clinical trial for the treatment of female patients with active CLE[139]. The non-receptor tyrosine-protein kinase TYK2 (TYK2) inhibitor BMS-986165 is also being investigated for the treatment of SLE[140].

Targeting spleen tyrosine kinase. Spleen tyrosine kinase (SYK) is a highly conserved tyrosine kinase that mediates several biological functions, including the regulation of innate immune responses[141]. For example, SYK is activated downstream of PRRs to regulate innate immune responses against several pathogens, and is also important for triggering cellular cytotoxicity in lymphocytes and in nuclear factor-κB (NF-κB) signalling-mediated expression of pro-inflammatory cytokines and chemokines[142]. Phosphorylated SYK is strongly expressed in CLE skin lesions[143]. In functional studies, the anti-SYK antibody GSK143 inhibited the expression of CLE-typical pro-inflammatory mediators, including OAS2, CXCL9 and CXCL10, in in vitro models of CLE involving 3D epidermis constructs or keratinocyte cultures[143]. Treatment with another SYK inhibitor, fostamatinib (also known as R788), reduced established skin disease in mouse models of CLE141. The efficacy of a topical SYK inhibitor (GSK2646264) in CLE is currently under investigation in a phase I clinical trial[144], and the oral SYK-inhibitor lanraplenib (GS-9876) is being tested in parallel with filgotinib in a phase II study in female patients with moderate-to-severe CLE[139].

Targeting other intracellular signalling pathways. Intracellular pathways might provide several additional potential therapeutic targets in CLE. These include the NF-κB signalling pathway and the mitogen-activated protein kinase (MAPK) signalling cascade. Iguratimod is a synthetic anti-inflammatory small-molecule drug that inhibits the activation of NF-κB and is currently under investigation for the treatment of lupus nephritis in a phase I clinical trial[145]. Some MAPK inhibitors have beneficial effects in mouse models of SLE (SB203580 and FR167653)[146,147]. Finally, dimethyl fumarate, a drug that blocks NF-κB and MAPK signalling, decreased disease

activity in a small cohort of 11 patients with CLE in a phase II pilot study[148].

Targeting pro-inflammatory cytokines. Several pro-inflammatory cytokines, including TNF, IL-12 and IL-6, are upregulated in the lesional skin of patients with CLE compared with non-lesional skin or the skin of healthy individuals[21,149]. A few case reports have suggested that TNF inhibitors, including infliximab and etanercept, can be efficacious in treating some patients with CLE[150,151], but these drugs can also induce CLE-like skin lesions[152]. Therefore, the efficacy of anti-TNF treatment strategies in CLE is still under debate and is being investigated in a clinical trial with etanercept[153]. Treatment with the IL-12 and IL-23 inhibitor ustekinumab reduced the skin disease activity of patients with SLE who had a high CLASI score (CLASI ≥ 4) in a phase II clinical trial published in 2018 (REF.[154]). This drug has been shown to be effective in treating patients with SCLE[155] and to improve mucocutaneous disease features of SLE[154]. However, another study has reported a case of ustekinumab-induced SCLE in a patient with pre-existing psoriasis[156]. Two IL-6 inhibitors (PF-04236921 (REF.[157]) and sirukumab[158]) and two inhibitors of the IL-6-receptor (MRA003US and vobarilizumab) have been tested in SLE and/or CLE without success[98,159].

Conclusions

Detailed insights into the molecular landscape of CLE, in combination with new advances in the understanding of innate immune response pathways and their interaction with adaptive mechanisms, have revolutionized our understanding of the pathological mechanisms underlying this disease. This new insight has informed the development of new therapeutic strategies such as the modulation of B cell and T cell activation, or the inhibition of the type I interferon pathway by targeting pDCs, IFNAR or JAK–STAT signalling. Several studies of therapies that target other pro-inflammatory pathway molecules are underway and will hopefully provide more in vivo insights. From a dermatological point of view, the development of small molecules with the capacity to penetrate the skin barrier is of particular interest. These drugs might be effective as topical treatment strategies and might thus reduce systemic adverse effects in patients with CLE. Moreover, interdisciplinary cooperation might not only be able to address problems such as the systemic effects of cutaneous inflammation but will also be able to further improve the possibilities for personalized targeted therapies.

Published online 9 August 2019

1. Kuhn, A., Wenzel, J. & Bijl, M. Lupus erythematosus revisited. *Semin. Immunopathol.* **38**, 97–112 (2016).
2. Stannard, J. N. & Kahlenberg, J. M. Cutaneous lupus erythematosus: updates on pathogenesis and associations with systemic lupus. *Curr. Opin. Rheumatol.* **28**, 453–459 (2016).
3. Hejazi, E. Z. & Werth, V. P. Cutaneous lupus erythematosus: an update on pathogenesis, diagnosis and treatment. *Am. J. Clin. Dermatol.* **17**, 135–146 (2016).
4. Kuhn, A., Rondinone, R., Doria, A. & Shoenfeld, Y. 1st international conference on cutaneous lupus erythematosus Düsseldorf, Germany, September 1–5, 2004. *Autoimmun. Rev.* **4**, 66–78 (2005).
5. Gilliam, J. N. & Sontheimer, R. D. Distinctive cutaneous subsets in the spectrum of lupus erythematosus. *J. Am. Acad. Dermatol.* **4**, 471–475 (1981).
6. Grönhagen, C. M., Fored, C. M., Granath, F. & Nyberg, F. Cutaneous lupus erythematosus and the association with systemic lupus erythematosus: a population-based cohort of 1088 patients in Sweden. *Br. J. Dermatol.* **164**, 1335–1341 (2011).
7. Biazar, C. et al. Cutaneous lupus erythematosus: first multicenter database analysis of 1002 patients from the European Society of Cutaneous Lupus Erythematosus (EUSCLE). *Autoimmun. Rev.* **12**, 444–454 (2013).
8. Jarukitsopa, S. et al. Epidemiology of systemic lupus erythematosus and cutaneous lupus erythematosus in a predominantly white population in the United States. *Arthritis Care Res.* **67**, 817–828 (2015).
9. Durosaro, O., Davis, M. D. P., Reed, K. B. & Rohlinger, A. L. Incidence of cutaneous lupus erythematosus, 1965–2005: a population-based study. *Arch. Dermatol.* **145**, 249–253 (2009).
10. Patel, P. & Werth, V. Cutaneous lupus erythematosus: a review. *Dermatol. Clin.* **20**, 373–385 (2002).
11. Lipsker, D. The need to revisit the nosology of cutaneous lupus erythematosus: the current terminology and morphologic classification of cutaneous LE: difficult, incomplete and not always applicable. *Lupus* **19**, 1047–1049 (2010).
12. Lin, J. H., Dutz, J. P., Sontheimer, R. D. & Werth, V. P. Pathophysiology of cutaneous lupus erythematosus. *Clin. Rev. Allergy Immunol.* **33**, 85–106 (2007).
13. Wieczorek, I. T., Propert, K. J., Okawa, J. & Werth, V. P. Systemic symptoms in the progression of cutaneous to systemic lupus erythematosus. *JAMA Dermatol.* **150**, 291–296 (2014).
14. Sticherling, M. Kutaner lupus erythematodes und Hautveränderungen beim systemischen lupus erythematodes [German]. *Z. Rheumatol.* **72**, 429–435 (2013).
15. Kuhn, A. & Landmann, A. The classification and diagnosis of cutaneous lupus erythematosus. *J. Autoimmun.* **48-49**, 14–19 (2014).
16. Uva, L. et al. Cutaneous manifestations of systemic lupus erythematosus. *Autoimmune Dis.* **2012**, 834291 (2012).
17. Wenzel, J. et al. The expression pattern of interferon-inducible proteins reflects the characteristic histological distribution of infiltrating immune cells in different cutaneous lupus erythematosus subsets. *Br. J. Dermatol.* **157**, 752–757 (2007).
18. Wenzel, J. & Tuting, T. An IFN-associated cytotoxic cellular immune response against viral, self-, or tumor antigens is a common pathogenetic feature in "interface dermatitis". *J. Invest. Dermatol.* **128**, 2392–2402 (2008).
19. Lauffer, F. et al. Type I immune response induces keratinocyte necroptosis and is associated with interface dermatitis. *J. Invest. Dermatol.* **38**, 1785–1794 (2018).
20. Obermoser, G., Sontheimer, R. D. & Zelger, B. Overview of common, rare and atypical manifestations of cutaneous lupus erythematosus and histopathological correlates. *Lupus* **19**, 1050–1070 (2010).
21. Scholtissek, B. et al. Immunostimulatory endogenous nucleic acids drive the lesional inflammation in cutaneous lupus erythematosus. *J. Invest. Dermatol.* **137**, 1484–1492 (2017).
22. Sarkar, M. K. et al. Photosensitivity and type I IFN responses in cutaneous lupus are driven by epidermal-derived interferon kappa. *Ann. Rheum. Dis.* **77**, 1653–1664 (2018).
23. Zahn, S. et al. Evidence for a pathophysiological role of keratinocyte-derived type III interferon (IFNλ) in cutaneous lupus erythematosus. *J. Invest. Dermatol.* **131**, 133–140 (2011).
24. Wenzel, J., Zahn, S., Bieber, T. & Tuting, T. Type I interferon-associated cytotoxic inflammation in cutaneous lupus erythematosus. *Arch. Dermatol. Res.* **301**, 83–86 (2009).
25. Kuhn, A. et al. S2k guideline for treatment of cutaneous lupus erythematosus-guided by the European Dermatology Forum (EDF) in cooperation with the European Academy of Dermatology and Venereology (EADV). *J. Eur. Acad. Dermatol. Venereol.* **31**, 389–404 (2017).
26. Filotico, R. & Mastrandrea, V. Cutaneous lupus erythematosus: clinico-pathologic correlation. *G. Ital. Dermatol. Venereol.* **153**, 216–229 (2018).
27. Sunderkötter, C. H. et al. Nomenclature of cutaneous vasculitis: dermatologic addendum to the 2012 revised International Chapel Hill Consensus Conference nomenclature of vasculitides. *Arthritis Rheumatol.* **70**, 171–184 (2018).
28. Udompanich, S., Chanprapaph, K. & Suchonwanit, P. Hair and scalp changes in cutaneous and systemic lupus erythematosus. *Am. J. Clin. Dermatol.* **19**, 679–694 (2018).
29. Reich, A., Meurer, M., Viehweg, A. & Muller, D. J. Narrow-band UVB-induced externalization of selected nuclear antigens in keratinocytes: implications for lupus erythematosus pathogenesis. *Photochem. Photobiol.* **85**, 1–7 (2009).
30. Casciola-Rosen, L. & Rosen, A. Ultraviolet light-induced keratinocyte apoptosis: a potential mechanism for the induction of skin lesions and autoantibody production in LE. *Lupus* **6**, 175–180 (1997).
31. Zhang, Y.-P., Wu, J., Han, Y.-F., Shi, Z.-R. & Wang, L. Pathogenesis of cutaneous lupus erythema associated with and without systemic lupus erythema. *Autoimmun. Rev.* **16**, 735–742 (2017).
32. Wenzel, J. et al. Scarring skin lesions of discoid lupus erythematosus are characterized by high numbers of skin-homing cytotoxic lymphocytes associated with strong expression of the type I interferon-induced protein MxA. *Br. J. Dermatol.* **153**, 1011–1015 (2005).
33. Mak, A. & Kow, N. Y. The pathology of T cells in systemic lupus erythematosus. *J. Immunol. Res.* **2014**, 419029 (2014).
34. Grassi, M., Capello, F., Bertolino, L., Seia, Z. & Pippione, M. Identification of granzyme B-expressing CD-8-positive T cells in lymphocytic inflammatory infiltrate in cutaneous lupus erythematosus and in dermatomyositis. *Clin. Exp. Dermatol.* **34**, 910–914 (2009).
35. Herrada, A. A. et al. Innate immune cells' contribution to systemic lupus erythematosus. *Front. Immunol.* **10**, 772 (2019).
36. Sestak, A. L., Fürnrohr, B. G., Harley, J. B., Merrill, J. T. & Namjou, B. The genetics of systemic lupus erythematosus and implications for targeted therapy. *Ann. Rheum. Dis.* **70**, i37–i43 (2011).
37. Peschke, K. et al. Deregulated type I IFN response in TREX1-associated familial chilblain lupus. *J. Invest. Dermatol.* **134**, 1456–1459 (2014).
38. Hersh, A. O., Arkin, L. M. & Prahalad, S. Immunogenetics of cutaneous lupus erythematosus. *Curr. Opin. Pediatr.* **28**, 470–475 (2016).
39. Foering, K. et al. Characterization of clinical photosensitivity in cutaneous lupus erythematosus. *J. Am. Acad. Dermatol.* **69**, 205–213 (2013).

40. Gehrke, N. et al. Oxidative damage of DNA confers resistance to cytosolic nuclease TREX1 degradation and potentiates STING-dependent immune sensing. *Immunity* **39**, 482–495 (2013).
41. Kaczmarczyk-Sekuła, K. et al. Mast cells in systemic and cutaneous lupus erythematosus. *Pol. J. Pathol.* **4**, 397–402 (2015).
42. Gerl, V. et al. The intracellular 52-kd Ro/SSA autoantigen in keratinocytes is up-regulated by tumor necrosis factor α via tumor necrosis factor receptor I. *Arthritis Rheum.* **52**, 531–538 (2005).
43. Patsinakidis, N. et al. Suppression of UV-induced damage by a liposomal sunscreen: a prospective, open-label study in patients with cutaneous lupus erythematosus and healthy controls. *Exp. Dermatol.* **21**, 958–961 (2012).
44. Katayama, S. et al. Delineating the healthy human skin UV response and early induction of interferon pathway in cutaneous lupus erythematosus. *J. Invest. Dermatol.* https://doi.org/10.1016/j.jid.2019.02.035 (2019).
45. Chang, J. & Werth, V. P. Therapeutic options for cutaneous lupus erythematosus: recent advances and future prospects. *Expert Rev. Clin. Immunol.* **12**, 1109–1121 (2016).
46. Piette, E. W. et al. Impact of smoking in cutaneous lupus erythematosus. *Arch. Dermatol.* **148**, 317–322 (2012).
47. White, P. C. et al. Cigarette smoke modifies neutrophil chemotaxis, neutrophil extracellular trap formation and inflammatory response-related gene expression. *J. Periodont. Res.* **53**, 525–535 (2018).
48. Vaglio, A. et al. Drug-induced lupus: traditional and new concepts. *Autoimmun. Rev.* **17**, 912–918 (2018).
49. Sandholdt, L. H., Laurinaviciene, R. & Bygum, A. Proton pump inhibitor-induced subacute cutaneous lupus erythematosus. *Br. J. Dermatol.* **170**, 342–351 (2014).
50. Biermann, M. H. C. et al. The role of dead cell clearance in the etiology and pathogenesis of systemic lupus erythematosus: dendritic cells as potential targets. *Expert Rev. Clin. Immunol.* **10**, 1151–1164 (2014).
51. Shovman, O., Tamar, S., Amital, H., Watad, A. & Shoenfeld, Y. Diverse patterns of anti-TNF-α-induced lupus: case series and review of the literature. *Clin. Rheumatol.* **37**, 563–568 (2018).
52. Levine, D., Switlyk, S. A. & Gottlieb, A. Cutaneous lupus erythematosus and anti-TNF-α therapy: a case report with review of the literature. *J. Drugs Dermatol.* **9**, 1283–1287 (2010).
53. Fiorentino, D. F. The Yin and Yang of TNF-α inhibition. *Arch. Dermatol.* **143**, 233–236 (2007).
54. Arrue, I., Saiz, A., Ortiz-Romero, P. L. & Rodríguez-Peralto, J. L. Lupus-like reaction to interferon at the injection site: report of five cases. *J. Cutan. Pathol.* **34**, 18–21 (2007).
55. Curran, C. S., Gupta, S., Sanz, I. & Sharon, E. PD-1 immunobiology in systemic lupus erythematosus. *J. Autoimmun.* **97**, 1–9 (2018).
56. Sinha, A. A. & Dey-Rao, R. Genomic investigation of lupus in the skin. *J. Invest. Dermatol. Symp. Proc.* **18**, S75–S80 (2017).
57. Dey-Rao, R. & Sinha, A. A. Genome-wide transcriptional profiling data from skin of chronic cutaneous lupus erythematosus (CCLE) patients. *Data Brief* **4**, 47–49 (2015).
58. Zahn, S. et al. Interferon-α stimulates TRAIL expression in human keratinocytes and peripheral blood mononuclear cells: implications for the pathogenesis of cutaneous lupus erythematosus. *Br. J. Dermatol.* **165**, 1118–1123 (2011).
59. Muskardin, T. L. W. & Niewold, T. B. Type I interferon in rheumatic diseases. *Nat. Rev. Rheumatol.* **14**, 214–228 (2018).
60. Yin, Q. et al. Ultraviolet B irradiation induces skin accumulation of plasmacytoid dendritic cells: a possible role for chemerin. *Autoimmunity* **47**, 185–192 (2014).
61. Liu, L., Xu, G., Dou, H. & Deng, G.-M. The features of skin inflammation induced by lupus serum. *Clin. Immunol.* **165**, 4–11 (2016).
62. Dudhgaonkar, S. et al. Selective IRAK4 inhibition attenuates disease in murine lupus models and demonstrates steroid sparing activity. *J. Immunol.* **198**, 1308–1319 (2017).
63. Mande, P. et al. Fas ligand promotes an inducible TLR-dependent model of cutaneous lupus-like inflammation. *J. Clin. Invest.* **128**, 2966–2978 (2018).
64. König, N. et al. Familial chilblain lupus due to a gain-of-function mutation in STING. *Ann. Rheum. Dis.* **76**, 468–472 (2017).
65. Sabrautzki, S. et al. An ENU mutagenesis-derived mouse model with a dominant *Jak1* mutation resembling phenotypes of systemic autoimmune disease. *Am. J. Pathol.* **183**, 352–368 (2013).
66. Means, T. K. et al. Human lupus autoantibody-DNA complexes activate DCs through cooperation of CD32 and TLR9. *J. Clin. Invest.* **115**, 407–417 (2005).
67. Eloranta, M.-L. et al. Regulation of the interferon-α production induced by RNA-containing immune complexes in plasmacytoid dendritic cells. *Arthritis Rheum.* **60**, 2418–2427 (2009).
68. Saadeh, D., Kurban, M. & Abbas, O. Update on the role of plasmacytoid dendritic cells in inflammatory/autoimmune skin diseases. *Exp. Dermatol.* **25**, 415–421 (2016).
69. Liu, Z. & Davidson, A. Taming lupus — a new understanding of pathogenesis is leading to clinical advances. *Nat. Med.* **18**, 871–882 (2012).
70. Rönnblom, L. The type I interferon system in the etiopathogenesis of autoimmune diseases. *Ups. J. Med. Sci.* **116**, 227–237 (2011).
71. Kalali, B. N. et al. Double-stranded RNA induces an antiviral defense status in epidermal keratinocytes through TLR3-, PKR-, and MDA5/RIG-I-mediated differential signaling. *J. Immunol.* **181**, 2694–2704 (2008).
72. Skouboe, M. K. et al. STING agonists enable antiviral cross-talk between human cells and confer protection against genital herpes in mice. *PLOS Pathog.* **14**, e1006976 (2018).
73. Stannard, J. N. et al. Lupus skin is primed for IL-6 inflammatory responses through a keratinocyte-mediated autocrine type I interferon loop. *J. Invest. Dermatol.* **137**, 115–122 (2017).
74. Liu, Y. et al. TWEAK/Fn14 activation participates in Ro52-mediated photosensitization in cutaneous lupus erythematosus. *Front. Immunol.* **8**, 651 (2017).
75. Zahn, S. et al. Ultraviolet light protection by a sunscreen prevents interferon-driven skin inflammation in cutaneous lupus erythematosus. *Exp. Dermatol.* **23**, 516–518 (2014).
76. Wenzel, J. et al. Enhanced type I interferon signalling promotes Th1-biased inflammation in cutaneous lupus erythematosus. *J. Pathol.* **205**, 435–442 (2005).
77. Kuhn, A. et al. Accumulation of apoptotic cells in the epidermis of patients with cutaneous lupus erythematosus after ultraviolet irradiation. *Arthritis Rheum.* **54**, 939–950 (2006).
78. Kuechle, M. K. & Elkon, K. B. Shining light on lupus and UV. *Arthritis Res. Ther.* **9**, 101 (2007).
79. Mistry, P. & Kaplan, M. J. Cell death in the pathogenesis of systemic lupus erythematosus and lupus nephritis. *Clin. Immunol.* **185**, 59–73 (2017).
80. Wang, D., Drenker, M., Eiz-Vesper, B., Werfel, T. & Wittmann, M. Evidence for a pathogenetic role of interleukin-18 in cutaneous lupus erythematosus. *Arthritis Rheum.* **58**, 3205–3215 (2008).
81. Caneparo, V., Landolfo, S., Gariglio, M. & De Andrea, M. The absent in melanoma 2-like receptor IFN-inducible protein 16 as an inflammasome regulator in systemic lupus erythematosus: the dark side of sensing microbes. *Front. Immunol.* **9**, 1180 (2018).
82. Kreuter, A. et al. Expression of antimicrobial peptides in different subtypes of cutaneous lupus erythematosus. *J. Am. Acad. Dermatol.* **65**, 125–133 (2011).
83. Chamilos, G. et al. Cytosolic sensing of extracellular self-DNA transported into monocytes by the antimicrobial peptide LL37. *Blood* **120**, 3699–3707 (2012).
84. Drake, L. A. et al. Guidelines of care for cutaneous lupus erythematosus. American Academy of Dermatology. *J. Am. Acad. Dermatol.* **34**, 830–836 (1996).
85. Kuhn, A., Landmann, A. & Wenzel, J. Advances in the treatment of cutaneous lupus erythematosus. *Lupus* **25**, 830–837 (2016).
86. Kuhn, A. et al. Photoprotective effects of a broad-spectrum sunscreen in ultraviolet-induced cutaneous lupus erythematosus: a randomized, vehicle-controlled, double-blind study. *J. Am. Acad. Dermatol.* **64**, 37–48 (2011).
87. Kuhn, A. et al. Efficacy of tacrolimus 0.1% ointment in cutaneous lupus erythematosus: a multicenter, randomized, double-blind, vehicle-controlled trial. *J. Am. Acad. Dermatol.* **65**, 54–64.e2 (2011).
88. Alves, P. et al. Quinacrine suppresses tumor necrosis factor-α and IFN-α in dermatomyositis and cutaneous lupus erythematosus. *J. Investig. Dermatol. Symp. Proc.* **18**, S57–S63 (2017).
89. Kuznik, A. et al. Mechanism of endosomal TLR inhibition by antimalarial drugs and imidazoquinolines. *J. Immunol.* **186**, 4794–4804 (2011).
90. Yokogawa, N. et al. Effects of hydroxychloroquine in patients with cutaneous lupus erythematosus: a multicenter, double-blind, randomized, parallel-group trial. *Arthritis Rheumatol.* **69**, 791–799 (2017).
91. Zeidi, M., Kim, H. J. & Werth, V. P. Increased myeloid dendritic cells and TNF-α expression predicts poor response to hydroxychloroquine in cutaneous lupus erythematosus. *J. Invest. Dermatol.* **139**, 324–332 (2019).
92. Wenzel, J. Methotrexate in systemic lupus erythematosus. *Lupus* **14**, 569 (2005).
93. Klebes, M., Wutte, N. & Aberer, E. Dapsone as second-line treatment for cutaneous lupus erythematosus? A retrospective analysis of 34 patients and a review of the literature. *Dermatology* **232**, 91–96 (2016).
94. Shornick, J. K., Formica, N. & Parke, A. L. Isotretinoin for refractory lupus erythematosus. *J. Am. Acad. Dermatol.* **24**, 49–52 (1991).
95. Chan, E. S. L. & Cronstein, B. N. Methotrexate—how does it really work? *Nat. Rev. Rheumatol.* **6**, 175–178 (2010).
96. Thomas, S. et al. Methotrexate is a JAK/STAT pathway inhibitor. *PLOS ONE* **10**, e0130078 (2015).
97. Klaeschen, A. S. & Wenzel, J. Upcoming therapeutic targets in cutaneous lupus erythematosus. *Expert Rev. Clin. Pharmacol.* **9**, 567–578 (2016).
98. Felten, R. et al. The 2018 pipeline of targeted therapies under clinical development for systemic lupus erythematosus: a systematic review of trials. *Autoimmun. Rev.* **17**, 781–790 (2018).
99. Presto, J. K., Hejazi, E. Z. & Werth, V. P. Biological therapies in the treatment of cutaneous lupus erythematosus. *Lupus* **26**, 115–118 (2017).
100. Hofmann, S. C., Leandro, M. J., Morris, S. D. & Isenberg, D. A. Effects of rituximab-based B-cell depletion therapy on skin manifestations of lupus erythematosus—report of 17 cases and review of the literature. *Lupus* **22**, 932–939 (2013).
101. Berghen, N., Vulsteke, J.-B., Westhovens, R., Lenaerts, J. & De Langhe, E. Rituximab in systemic autoimmune rheumatic diseases: indications and practical use. *Acta Clin. Belg.* **74**, 272–279 (2018).
102. Vital, E. M. et al. Brief report: responses to rituximab suggest B cell-independent inflammation in cutaneous systemic lupus erythematosus. *Arthritis Rheumatol.* **67**, 1586–1591 (2015).
103. Vashisht, P., Borghoff, K. & O'Dell, J. R. Hearth-Holmes, M. Belimumab for the treatment of recalcitrant cutaneous lupus. *Lupus* **26**, 857–864 (2017).
104. Iaccarino, L. et al. Effects of belimumab on flare rate and expected damage progression in patients with active systemic lupus erythematosus. *Arthritis Care Res. (Hoboken)* **69**, 115–123 (2017).
105. European Medicines Agency. *EU Clinical Trials Register* https://www.clinicaltrialsregister.eu/ctr-search/trial/2017-003051-35/DE (2018).
106. Wenzel, J., Landmann, A., Vorwerk, G. & Kuhn, A. High expression of B lymphocyte stimulator in lesional keratinocytes of patients with cutaneous lupus erythematosus. *Exp. Dermatol.* **27**, 95–97 (2018).
107. Merrill, J. T. et al. Efficacy and safety of atacicept in patients with systemic lupus erythematosus: results of a twenty-four-week, multicenter, randomized, double-blind, placebo-controlled, parallel-arm, phase IIb study. *Arthritis Rheumatol.* **70**, 266–276 (2018).
108. Kohler, S. et al. Bortezomib in antibody-mediated autoimmune diseases (TAVAB): study protocol for a unicentric, non-randomised, non-placebo controlled trial. *BMJ Open* **9**, e024523 (2019).
109. Shirley, M. Ixazomib: first global approval. *Drugs* **76**, 405–411 (2016).
110. Alexander, T. et al. Proteasome inhibition with bortezomib induces a therapeutically relevant depletion of plasma cells in SLE but does not target their precursors. *Eur. J. Immunol.* **48**, 1573–1579 (2018).
111. Aguayo-Leiva, I., Vano-Galvan, S., Carrillo-Gijon, R. & Jaén-Olasolo, P. Lupus tumidus induced by bortezomib not requiring discontinuation of the drug. *J. Eur. Acad. Dermatol. Venereol.* **24**, 1363–1364 (2010).
112. Gensous, N. et al. T follicular helper cells in autoimmune disorders. *Front. Immunol.* **9**, 1637 (2018).
113. Katsuyama, T., Tsokos, G. C. & Moulton, V. R. Aberrant T cell signaling and subsets in systemic lupus erythematosus. *Front. Immunol.* **9**, 1088 (2018).
114. Dehesa, L., Abuchar, A., Nuno-Gonzalez, A., Vitiello, M. & Kerdel, F. A. The use of cyclosporine in dermatology. *J. Drugs Dermatol.* **11**, 979–987 (2012).
115. Wu, Q. & Kuca, K. Metabolic pathway of cyclosporine A and its correlation with nephrotoxicity. *Curr. Drug Metab.* **20**, 84–90 (2018).

116. Sin, F. E. & Isenberg, D. An evaluation of voclosporin for the treatment of lupus nephritis. *Expert Opin. Pharmacother.* **19**, 1613–1621 (2018).
117. Spee-Mayer, C. Von et al. Low-dose interleukin-2 selectively corrects regulatory T cell defects in patients with systemic lupus erythematosus. *Ann. Rheum. Dis.* **75**, 1407–1415 (2016).
118. US National Library of Medicine. *ClinicalTrials.gov* https://clinicaltrials.gov/ct2/show/NCT03312335 (2018).
119. US National Library of Medicine. *ClinicalTrials.gov* https://clinicaltrials.gov/ct2/show/NCT02770170 (2019).
120. US National Library of Medicine. *ClinicalTrials.gov* https://clinicaltrials.gov/ct2/show/NCT02804763 (2019).
121. Danion, F. et al. Efficacy of abatacept in systemic lupus erythematosus: a retrospective analysis of 11 patients with refractory disease. *Lupus* **25**, 1440–1447 (2016).
122. Tarazi, M., Aiempanakit, K. & Werth, V. P. Subacute cutaneous lupus erythematosus and systemic lupus erythematosus associated with abatacept. *JAAD Case Rep.* **4**, 698–700 (2018).
123. Biliouris, K. et al. A pre-clinical quantitative model predicts the pharmacokinetics/pharmacodynamics of an anti-BDCA2 monoclonal antibody in humans. *J. Pharmacokinet. Pharmacodyn.* **45**, 817–827 (2018).
124. US National Library of Medicine. *ClinicalTrials.gov* https://clinicaltrials.gov/ct2/show/NCT02847598 (2019).
125. Furie, R. et al. BIIB059, a monoclonal antibody targeting BDCA2, shows evidence of biological activity and early clinical proof of concept in subjects with active cutaneous LE. *Ann. Rheum. Dis.* **76**, (Suppl. 2), 857 (2017).
126. US National Library of Medicine. *ClinicalTrials.gov* https://clinicaltrials.gov/ct2/show/NCT03817424 (2019).
127. Kalunian, K. C. et al. A phase II study of the efficacy and safety of rontalizumab (rhuMAb interferon-α) in patients with systemic lupus erythematosus (ROSE). *Ann. Rheum. Dis.* **75**, 196–202 (2016).
128. Merrill, J. T. et al. Safety profile and clinical activity of sifalimumab, a fully human anti-interferon α monoclonal antibody, in systemic lupus erythematosus: a phase I, multicentre, double-blind randomised study. *Ann. Rheum. Dis.* **70**, 1905–1913 (2011).
129. Werth, V. P. et al. Brief report: pharmacodynamics, safety, and clinical efficacy of AMG 811, a human anti-interferon-γ antibody, in patients with discoid lupus erythematosus. *Arthritis Rheumatol.* **69**, 1028–1034 (2017).
130. Furie, R. et al. Anifrolumab, an anti-interferon-α receptor monoclonal antibody, in moderate-to-severe systemic lupus erythematosus. *Arthritis Rheumatol.* **69**, 376–386 (2017).
131. Santos, F. P. S. & Verstovsek, S. Efficacy of ruxolitinib for myelofibrosis. *Expert Opin. Pharmacother.* **15**, 1465–1473 (2014).
132. Spoerl, S. et al. Activity of therapeutic JAK 1/2 blockade in graft-versus-host disease. *Blood* **123**, 3832–3842 (2014).
133. Hornung, T. et al. Remission of recalcitrant dermatomyositis treated with ruxolitinib. *N. Engl. J. Med.* **371**, 2537–2538 (2014).
134. Hornung, T., Wolf, D. & Wenzel, J. More on remission of recalcitrant dermatomyositis treated with ruxolitinib. *N. Engl. J. Med.* **372**, 1273–1274 (2015).
135. Klaeschen, A. S., Wolf, D., Brossart, P., Bieber, T. & Wenzel, J. JAK inhibitor ruxolitinib inhibits the expression of cytokines characteristic of cutaneous lupus erythematosus. *Exp. Dermatol.* **26**, 728–730 (2017).
136. Wenzel, J. et al. JAK1/2 inhibitor ruxolitinib controls a case of chilblain lupus erythematosus. *J. Invest. Dermatol.* **136**, 1281–1283 (2016).
137. US National Library of Medicine. *ClinicalTrials.gov* https://clinicaltrials.gov/ct2/show/NCT03159936 (2019).
138. Wallace, D. J. et al. Baricitinib for systemic lupus erythematosus: a double-blind, randomised, placebo-controlled, phase 2 trial. *Lancet* **392**, 222–231 (2018).
139. US National Library of Medicine. *ClinicalTrials.gov* https://clinicaltrials.gov/ct2/show/NCT03134222 (2019).
140. US National Library of Medicine. *ClinicalTrials.gov* https://clinicaltrials.gov/ct2/show/NCT03920267 (2019).
141. Deng, G.-M., Liu, L., Bahjat, F. R., Pine, P. R. & Tsokos, G. C. Suppression of skin and kidney disease by inhibition of spleen tyrosine kinase in lupus-prone mice. *Arthritis Rheum.* **62**, 2086–2092 (2010).
142. Deng, G.-M. & Tsokos, G. C. The role of Syk in cutaneous lupus erythematosus. *Exp. Dermatol.* **25**, 674–675 (2016).
143. Braegelmann, C. et al. Spleen tyrosine kinase (SYK) is a potential target for the treatment of cutaneous lupus erythematosus patients. *Exp. Dermatol.* **25**, 375–379 (2016).
144. US National Library of Medicine. *ClinicalTrials.gov* https://clinicaltrials.gov/ct2/show/NCT02927457 (2019).
145. US National Library of Medicine. *ClinicalTrials.gov* https://clinicaltrials.gov/ct2/show/NCT02936375 (2018).
146. Iwata, Y. et al. p38 mitogen-activated protein kinase contributes to autoimmune renal injury in MRL-Fas lpr mice. *J. Am. Soc. Nephrol.* **14**, 57–67 (2003).
147. Jin, N. et al. The selective p38 mitogen-activated protein kinase inhibitor, SB203580, improves renal disease in MRL/lpr mouse model of systemic lupus. *Int. Immunopharmacol.* **11**, 1319–1326 (2011).
148. Kuhn, A. et al. Fumaric acid ester treatment in cutaneous lupus erythematosus (CLE): a prospective, open-label, phase II pilot study. *Lupus* **25**, 1357–1364 (2016).
149. Dey-Rao, R., Smith, J. R., Chow, S. & Sinha, A. A. Differential gene expression analysis in CCLE lesions provides new insights regarding the genetics basis of skin vs. systemic disease. *Genomics* **104**, 144–155 (2014).
150. Norman, R., Greenberg, R. G. & Jackson, J. M. Case reports of etanercept in inflammatory dermatoses. *J. Am. Acad. Dermatol.* **54**, S139–S142 (2006).
151. Drosou, A., Kirsner, R. S., Welsh, E., Sullivan, T. P. & Kerdel, F. A. Use of infliximab, an anti-tumor necrosis α antibody, for inflammatory dermatoses. *J. Cutan. Med. Surg.* **7**, 382–386 (2003).
152. Aringer, M. & Smolen, J. S. Efficacy and safety of TNF-blocker therapy in systemic lupus erythematosus. *Expert Opin. Drug Saf.* **7**, 411–419 (2008).
153. European Medicines Agency. *EU Clinical Trials Register* https://www.clinicaltrialsregister.eu/ctr-search/trial/2015-001602-33/GB (2015).
154. Van Vollenhoven, R. F. et al. Efficacy and safety of ustekinumab, an IL-12 and IL-23 inhibitor, in patients with active systemic lupus erythematosus: results of a multicentre, double-blind, phase 2, randomised, controlled study. *Lancet* **392**, 1330–1339 (2018).
155. Souza, A., De Ali-Shaw, T., Strober, B. E. & Franks, A. G. Successful treatment of subacute lupus erythematosus with ustekinumab. *Arch. Dermatol.* **147**, 896–898 (2011).
156. Tierney, E., Kirthi, S., Ramsay, B. & Ahmad, K. Ustekinumab-induced subacute cutaneous lupus. *JAAD Case Rep.* **5**, 271–273 (2019).
157. US National Library of Medicine. *ClinicalTrials.gov* https://clinicaltrials.gov/ct2/show/NCT01405196 (2017).
158. US National Library of Medicine. *ClinicalTrials.gov* https://clinicaltrials.gov/ct2/show/NCT01702740 (2012).
159. US National Library of Medicine. *ClinicalTrials.gov* https://clinicaltrials.gov/ct2/show/NCT02437890 (2019).
160. Kunz, M. et al. Genome-wide association study identifies new susceptibility loci for cutaneous lupus erythematosus. *Exp. Dermatol.* **24**, 510–515 (2015).
161. Millard, T. P. et al. A candidate gene analysis of three related photosensitivity disorders: cutaneous lupus erythematosus, polymorphic light eruption and actinic prurigo. *Br. J. Dermatol.* **145**, 229–236 (2001).
162. Ruiz-Larrañaga, O. et al. Genetic association study of systemic lupus erythematosus and disease subphenotypes in European populations. *Clin. Rheumatol.* **35**, 1161–1168 (2016).
163. Järvinen, T. M. et al. Tyrosine kinase 2 and interferon regulatory factor 5 polymorphisms are associated with discoid and subacute cutaneous lupus erythematosus. *Exp. Dermatol.* **19**, 123–131 (2010).
164. Skonieczna, K. et al. Genetic similarities and differences between discoid and systemic lupus erythematosus patients within the Polish population. *Postepy Dermatol. Alergol.* **34**, 228–232 (2017).
165. Levy, S. B., Pinnell, S. R., Meadows, L., Snyderman, R. & Ward, F. E. Hereditary C2 deficiency associated with cutaneous lupus erythematosus: clinical, laboratory, and genetic studies. *Arch. Dermatol.* **115**, 57–61 (1979).
166. Agnello, V., Gell, J. & Tye, M. J. Partial genetic deficiency of the C4 component of complement in discoid lupus erythematosus and urticaria/angioedema. *J. Am. Acad. Dermatol.* **9**, 894–898 (1983).
167. Racila, D. M. et al. Homozygous single nucleotide polymorphism of the complement *C1QA* gene is associated with decreased levels of C1q in patients with subacute cutaneous lupus erythematosus. *Lupus* **12**, 124–132 (2003).
168. Lipsker, D. & Hauptmann, G. Cutaneous manifestations of complement deficiencies. *Lupus* **19**, 1096–1106 (2010).
169. Sanchez, E. et al. Phenotypic associations of genetic susceptibility loci in systemic lupus erythematosus. *Ann. Rheum. Dis.* **70**, 1752–1757 (2011).
170. Järvinen, T. M. et al. Polymorphisms of the *ITGAM* gene confer higher risk of discoid cutaneous than of systemic lupus erythematosus. *PLOS ONE* **5**, e14212 (2010).
171. Da Silva Fonseca, A. M. et al. Polymorphisms in *STK17A* gene are associated with systemic lupus erythematosus and its clinical manifestations. *Gene* **527**, 435–439 (2013).
172. Azevêdo Silva, J. De et al. Vitamin D receptor (*VDR*) gene polymorphisms and susceptibility to systemic lupus erythematosus clinical manifestations. *Lupus* **22**, 1110–1117 (2013).
173. Zhong, H. et al. Replicated associations of *TNFAIP3*, *TNIP1* and *ETS1* with systemic lupus erythematosus in a southwestern Chinese population. *Arthritis Res. Ther.* **13**, R186 (2011).
174. Vigato-Ferreira, I. C. C. et al. FcγRIIa and FcγRIIIb polymorphisms and associations with clinical manifestations in systemic lupus erythematosus patients. *Autoimmunity* **47**, 451–458 (2014).
175. Harley, I. T. W. et al. The role of genetic variation near interferon-kappa in systemic lupus erythematosus. *J. Biomed. Biotechnol.* **2010**, 706825 (2010).
176. US National Library of Medicine. *ClinicalTrials.gov* https://clinicaltrials.gov/ct2/show/NCT03122431 (2018).
177. US National Library of Medicine. *ClinicalTrials.gov* https://clinicaltrials.gov/ct2/show/NCT02176148 (2018).
178. US National Library of Medicine. *ClinicalTrials.gov* https://clinicaltrials.gov/ct2/show/NCT03260166 (2017).
179. US National Library of Medicine. *ClinicalTrials.gov* https://clinicaltrials.gov/ct2/show/NCT02428309 (2019).
180. European Medicines Agency. *EU Clinical Trials Register* https://www.clinicaltrialsregister.eu/ctr-search/trial/2017-001203-79/HU (2017).
181. US National Library of Medicine. *ClinicalTrials.gov* https://clinicaltrials.gov/ct2/show/NCT03288324 (2019).
182. US National Library of Medicine. *ClinicalTrials.gov* https://clinicaltrials.gov/ct2/show/NCT03517722 (2019).
183. US National Library of Medicine. *ClinicalTrials.gov* https://clinicaltrials.gov/ct2/show/NCT03866317 (2019).
184. European Medicines Agency. *EU Clinical Trials Register* https://www.clinicaltrialsregister.eu/ctr-search/trial/2016-003246-93/PL (2016).

Competing interests

J.W. declares that he has received financial support from GSK (for clinical studies, investigator-initiated trials and advisory board fees), Incyte (for investigator-initiated trials), Spirig (for an investigator-initiated trial), Medac (for advisory board fees), Actelion (for advisory board fees), Celgene (for advisory board fees), Biogen (for advisory board fees), Roche (for advisory board fees and clinical studies), Leo (for advisory board fees and clinical studies), Merck Serono (for clinical studies) and ArrayBio (for clinical studies).

Peer review information

Nature Reviews Rheumatology thanks M. Caproni, F. Furukawa and the other, anonymous, reviewer(s) for their contribution to the peer review of this work.

Supplementary information

Supplementary information is available for this paper at https://doi.org/10.1038/s41584-019-0272-0.

Next-generation imaging of the skeletal system and its blood supply

*Anika Grüneboom[1], Lasse Kling[2,3], Silke Christiansen[2,3], Leonid Mill[2,4], Andreas Maier[4], Klaus Engelke[1,5], Harald H. Quick[6,7], Georg Schett[1] and Matthias Gunzer[8]**

Abstract | Bone is organized in a hierarchical 3D architecture. Traditionally, analysis of the skeletal system was based on bone mass assessment by radiographic methods or on the examination of bone structure by 2D histological sections. Advanced imaging technologies and big data analysis now enable the unprecedented examination of bone and provide new insights into its 3D macrostructure and microstructure. These technologies comprise ex vivo and in vivo methods including high-resolution computed tomography (CT), synchrotron-based imaging, X-ray microscopy, ultra-high-field magnetic resonance imaging (MRI), light-sheet fluorescence microscopy, confocal and intravital two-photon imaging. In concert, these techniques have been used to detect and quantify a novel vascular system of trans-cortical vessels in bone. Furthermore, structures such as the lacunar network, which harbours and connects osteocytes, become accessible for 3D imaging and quantification using these methods. Next-generation imaging of the skeletal system and its blood supply are anticipated to contribute to an entirely new understanding of bone tissue composition and function, from macroscale to nanoscale, in health and disease. These insights could provide the basis for early detection and precision-type intervention of bone disorders in the future.

Haversian system
Structural unit of bone consisting of a central Haversian canal, which surrounds blood vessels and nerves, surrounded by concentric rings called lamellae.

In vertebrates, the skeleton is an essential structure as it mechanically supports the body, protects the inner organs, permits movement and locomotion, serves as a reservoir for minerals, growth factors and cytokines, and provides an environment for haematopoiesis and haematopoietic stem cell homeostasis within bone marrow compartments[1–3]. Skeletal bone is a highly dynamic tissue that adapts its mass and morphology to functional demands and ultimately repairs and remodels itself throughout a person's lifespan[1,4]. The continuous remodelling of bone depends on the balance of bone formation, via osteoblasts, and osteoclast-mediated bone resorption[5,6]. In adults, bone resorption takes ~10 days and re-formation ~3 months; through these coupled processes, ~5–10% of skeletal tissue is replaced every year[7,8]. Imbalances in the remodelling process can produce a variety of skeletal disorders[7]. The most common bone disorder, osteoporosis, is defined by reduced bone density, structural bone changes and increased fracture risk[8]. Today, osteoporosis affects more than 27 million people in Europe and the incidence of osteoporotic fractures is 3.5 million per year[9]. The cost of osteoporosis, including pharmacological intervention, was estimated at €37 billion in the European Union in 2010 (REF.[9]). Since osteoporosis primarily affects elderly individuals[10], the number of osteoporosis-associated fractures is predicted to quadruple within the next 20–30 years as the population ages; accordingly, medical research is increasingly focused on bone disorders[9].

Owing to the highly complex structure of bone, however, analysis of this tissue is challenging. Bone is hierarchically organized and contains structures from the macroscale, measured in centimetres and millimetres, to the nanoscale[4] (FIG. 1). Cortical bone, the outer hard shell of bone, consists of both inorganic minerals, mostly hydroxyapatite, and organic components, mainly type I collagen. In long bones such as the femur or tibia, the diaphysis primarily consists of cortical bone, whereas the metaphysis and epiphysis also contain trabecular bone (also known as cancellous bone), comprising a honeycomb-like meshwork of plates and rods. Irregular and flat bones, such as the sternum or the vertebrae, do not have such clear morphological separations; in these bones, the bone marrow is entirely filled with trabeculae, which are connected to the cortical bone in a lamellar pattern[2]. Cortical bone surrounds the bone marrow and is highly vascularized by the Haversian system in humans. This system of channels and blood vessels connects the outer peripheral circulation to the inner bone marrow, not only supplying nutrients but also providing an exit for haematopoietic cells formed in the bone marrow compartment. Like cortical bone, the blood

*e-mail: matthias.gunzer@uni-due.de

https://doi.org/10.1038/s41584-019-0274-y

Key points

- Bone is a complex tissue that has functional elements at size scales spanning five orders of magnitude.
- Studying all the different structures of bone is necessary to comprehensively understand bone function in health and disease in experimental and clinical settings.
- Comprehensive analysis of bone requires an array of different imaging approaches, including X-ray, magnetic resonance, and optical and electron microscopy imaging modalities.
- Fundamental improvements of methodology in all these imaging approaches now enable a completely new view of bone, resulting in novel insights into its function and blood supply.
- Massive amounts of imaging data emerging from such analyses require innovative image reconstruction algorithms, such as machine vision and deep learning, to extract meaningful information.

Lacuno-canalicular network (LCN). A system of sub-micrometre-sized channels (canaliculi) inside cortical bone that form a network with osteocyte-containing lacunae, through which osteocyte membrane processes make contact with other osteocytes or endothelial cells of trans-cortical blood vessels.

Pixels
Elements (or 'picture elements') of a 2D digital image, typically numbering in the hundreds of thousands or millions and arranged in rows and columns. Each pixel has a level of brightness (grey level) and, for coloured images, a combination of several (typically three) colour components.

Voxels
Similar to a pixel, a voxel (or 'volume pixel') is an image element in a 3D image such as a tomographic scan.

vessel canals also undergo osteoclast-mediated remodelling[11]. The cortical bone next to blood vessels contains abundant osteocytes, which develop from osteoblasts that become confined within the cortical bone matrix in lacunae. During osteocytogenesis, the trapped cells generate dendritic processes that penetrate the cortical bone through canaliculi and connect to other osteocytes and also endothelial cells, thereby forming the lacuno-canalicular network (LCN) of cortical bone[12–14]. Several osteocyte-specific proteins are critical for bone mineral homeostasis, and minerals such as phosphates can be released to the bone marrow or vascular system through canaliculi[11,13]. Furthermore, canaliculi are filled with interstitial fluid that can activate the tethering elements of osteocytes in response to increased fluid flow under mechanical load. Hence, osteocytes act as mechanosensors and mechanotransductors that can orchestrate bone remodelling processes: based on Wnt/β-catenin signalling, they transfer signals of mechanical loading to cells on the inner bone surface and can thereby orchestrate osteoblast and osteoclast function[14–18].

Studying and understanding all these hierarchical levels of bone tissue, from the organ level to the molecular level, requires multi-scale imaging techniques. Whereas traditionally the investigation of the skeletal system was based on bone mass assessment by radiographic methods or the examination of bone structure by 2D histological sections, today, multiple innovative imaging approaches are available that can address one or even several of the described hierarchical levels at one time (FIG. 1; see also Supplementary Fig. 1). In this Review, we give an overview of the latest advances in bone imaging and demonstrate how the use of novel technologies and methods can provide exciting new insights into bone biology.

Author addresses

[1]Department of Internal Medicine 3 – Rheumatology and Immunology, Friedrich-Alexander-University Erlangen-Nuremberg (FAU) and Universitätsklinikum Erlangen, Erlangen, Germany.
[2]Max Planck Institute for the Science of Light, Christiansen Research Group, Erlangen, Germany.
[3]Helmholtz-Zentrum Berlin für Materialien und Energie, Berlin, Germany.
[4]Pattern Recognition Lab, Department of Computer Science, Friedrich-Alexander-University Erlangen-Nuremberg, Erlangen, Germany.
[5]Institute of Medical Physics, Friedrich-Alexander-University Erlangen-Nuremberg (FAU), Universitätsklinikum Erlangen, Erlangen, Germany.
[6]Erwin L. Hahn Institute for Magnetic Resonance Imaging, University Duisburg-Essen, Essen, Germany.
[7]High-Field and Hybrid MR Imaging, University Hospital, University Duisburg-Essen, Essen, Germany.
[8]Institute for Experimental Immunology and Imaging, University Hospital, University Duisburg-Essen, Essen, Germany.

General concepts of imaging

Fundamentally, 'imaging' means the generation of a picture or video of an object of interest. Throughout this Review, we use the term imaging to refer to the visualization of structures that are not directly discernible to the human eye, either because they are too small to see or because they are hidden within opaque tissue. Both of these factors are inherent to bone and hence have driven the development of imaging technologies to overcome this 'invisibility' hurdle. Supplementary Fig. 2 provides a timeline for the development of different imaging modalities.

To the human eye, which is optimized to detect light within the 'visible range' (that is, ~400–700 nm wavelength), bones naturally appear opaque and are not visible from outside the body. Since the late nineteenth century, however, it has been known that X-rays, which have much shorter wavelengths, can pass through the body. They can be used to generate images of internal structures using a film, screen or camera containing X-ray-sensitive material[19]. X-ray imaging, which includes modern 3D applications termed computed tomography (CT), is excellent for investigating hard tissue such as solid bone, but not for discriminating soft tissue such as muscle or blood vessels. For clinical purposes, imaging of soft tissues is best achieved with magnetic resonance imaging (MRI). Unlike X-ray-based imaging, MRI does not have known lasting adverse effects and hence is ideally suited for frequent or longitudinal studies of patients (FIG. 2; TABLE 1).

However, although these clinical imaging approaches enable non-invasive imaging of bone, they achieve little more resolution (BOX 1) than the naked eye: pixels from 2D X-ray images or voxels from CT or MRI tomograms are within the range 50–80 µm in lateral length (FIG. 1); thus, smaller structures are not visualized. Better resolution is achieved by µCT, synchrotron-based imaging and X-ray microscopy (XRM), which can generate voxel sizes within the nanometre range[20,21]. As these modalities apply enormous amounts of radiation to the sample, however, they are not suitable for clinical imaging.

Visualization of microscale and nanoscale bone morphology, such as cellular structures, requires optical imaging with microscopes. Microscopes shine visible or infrared light onto a sample and use refractive optics consisting of glass-based lenses to generate highly magnified and well-resolved images that can be directly detected by the eye or by digital imaging devices. Optical imaging of bone achieves resolution as fine as 200 nm (REF.[22]), but the opacity of the tissue means that physical sectioning is normally required to visualize the inner structure. However, developments in imaging have been made that either make intact bones transparent or use near-infrared light, which can cross opaque bone at

Synchrotron-based imaging
Imaging modality comprising X-ray-based CT coupled to a powerful source of X-rays (synchrotron).

least to a certain extent. A specific version of optical imaging is fluorescence microscopy[23], which reveals specific structures in bones by the use of fluorescent dyes that are often linked to specific targeting molecules such as antibodies. Present-day installations of fluorescence microscopes (FIG. 2) are often confocal laser scanning microscopy (CLSM) or two-photon laser scanning microscopy (TPLSM) systems. Particularly useful for bone imaging is light-sheet fluorescence microscopy (LSFM).

In the following sections we provide an overview of the features of each of these technologies and their application to the imaging of bone and its blood supply (TABLE 1).

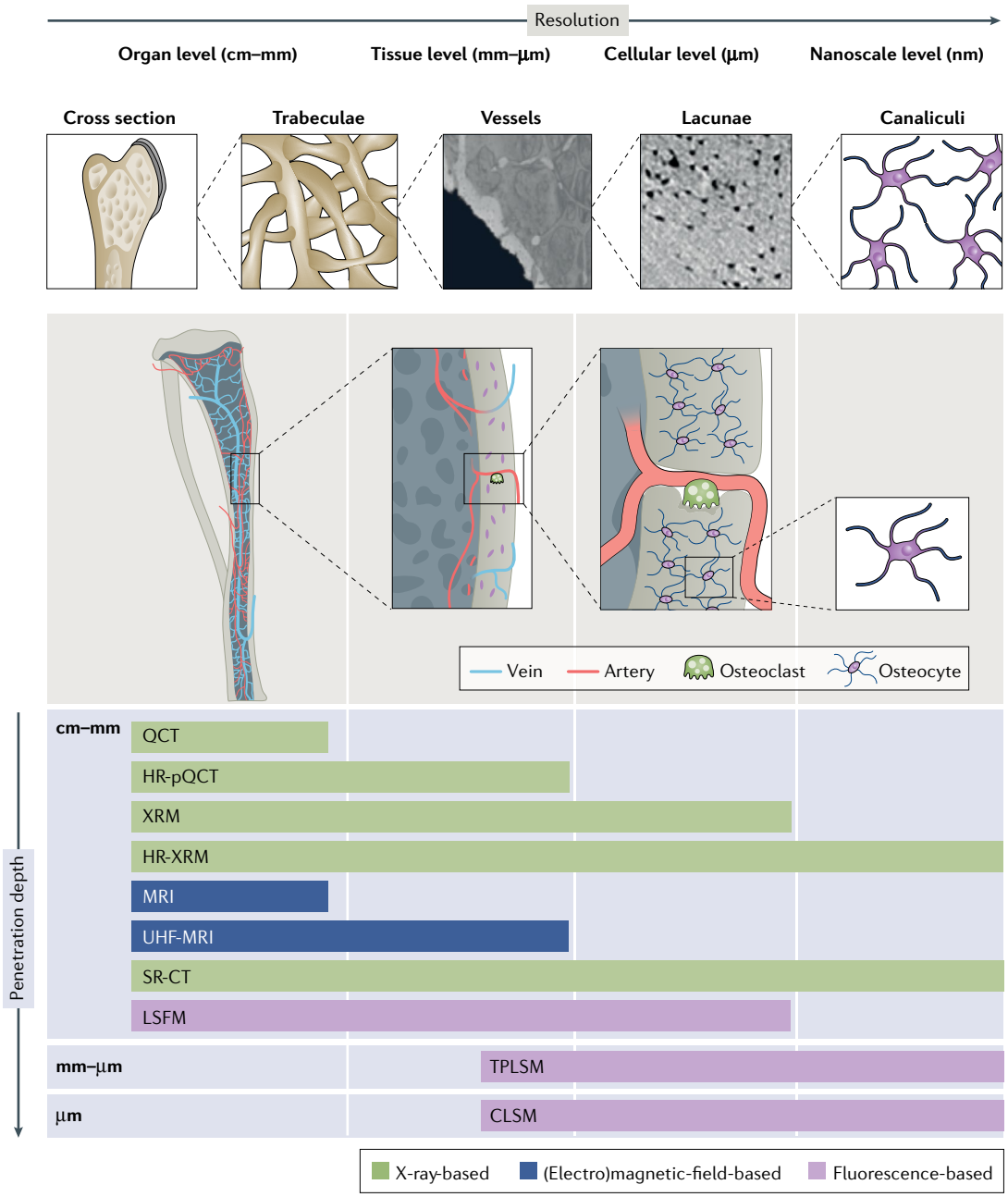

Fig. 1 | **Imaging the multi-scale architecture of bone.** Bone is a complex tissue that contains structures ranging from the macroscale organ level (measured in centimetres or millimetres) down to the nanoscale level. In osteoporosis, macrostructures in the centimetre to millimetre range, including cortical bone and trabeculae, are reduced in thickness and strength. Studying and understanding all the hierarchical levels of bone tissue requires multi-scale imaging techniques, which vary in their imaging resolution and penetration depth. Quantitative computed tomography (QCT), high-resolution peripheral QCT (HR-pQCT) and MRI are used for clinical imaging. X-ray microscopy (XRM), synchrotron radiation CT (SR-CT), high-resolution XRM (HR-XRM) and light-sheet fluorescence microscopy (LSFM) are not compatible with in vivo imaging, and two-photon laser scanning microscopy (TPLSM) and confocal laser scanning microscopy (CLSM) are only suitable for imaging bone in experimental animals. UHF-MRI, ultra-high-field MRI. Image of vessels and lacunae adapted from REF.[11], Springer Nature Limited.

Absorption coefficient
Describes how easily a tissue can be penetrated by X-ray radiation, expressed as the fraction of an X-ray beam that is absorbed or scattered per unit of thickness.

Clinical computed tomography

CT is an X-ray-based imaging technology. Compared with soft tissues (such as skin or muscle), dense tissues (such as bone) absorb much more X-ray energy and thus substantially reduce the intensity of radiation reaching the X-ray-sensitive material. On the earliest X-ray images, soft tissue appeared bright whereas bone appeared dark; today, however, the degree of absorption is measured by the absorption coefficient (also referred to as the attenuation coefficient); thus, on modern X-ray images, bone appears bright (high coefficient) and soft tissue appears dark (low coefficient). Unlike plain

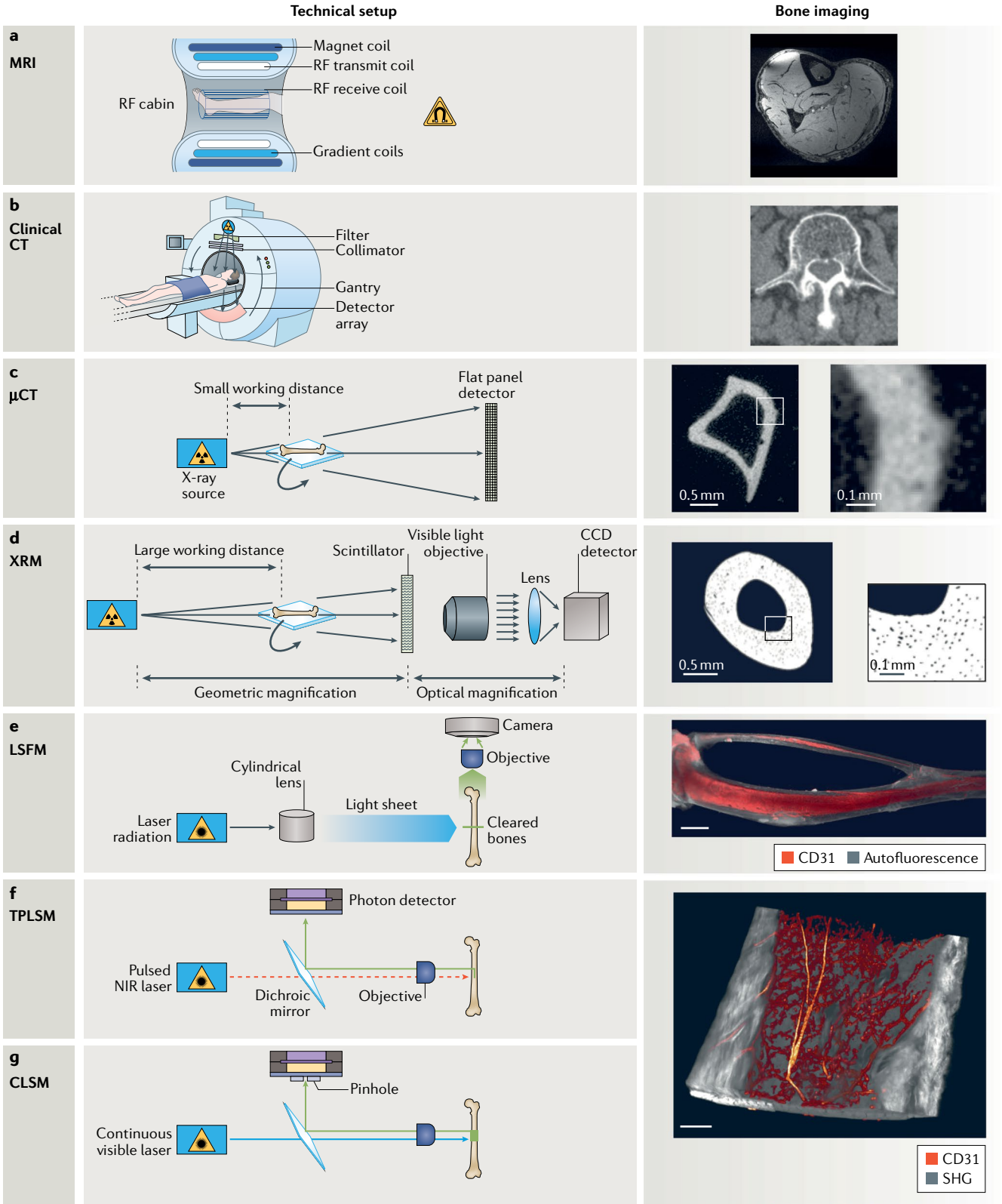

Hounsfield units
(HU). Values representing linearly transformed absorption coefficients, used to standardize CT scanners; by definition, the radiodensity of water is zero HU and air negative 1,000 HU. Bone is between +500 and +1,500 HU and fat is negative ~100 HU.

Calibration phantom
An object containing artificial materials with known physical density and X-ray absorption behaviour that is imaged by CT together with a patient to enable precise assessment of these properties in the patient´s tissue.

Areal BMD
A measurement of bone mineral content, determined by dividing the amount of bone mineral (in grams) by the area of the 2D bone site scanned (in square centimetres).

Kernels
In the context of CT image reconstruction, a special function that can be varied within a certain range in order to tune the pixel noise and the geometrical resolution.

radiographs, which are 2D projections of 3D tissue, CT combines X-ray measurements of a sample taken at different angles (FIG. 2) to produce a cross-sectional image; this image represents a map of the CT values of the sample measured in Hounsfield units.

If the patient or sample is continuously moved at right angles to the X-ray beams during image acquisition (as with helical or spiral CT), 3D images are obtained; in the clinic, this is achieved by rotating the CT system around the patient (FIG. 2).

CT has a number of clinical applications in the study of bone. Quantitative CT (QCT), for example, can rapidly (within 10–20 s) measure bone mineral density (BMD) and bone geometry at the spine or hip[24], and finite element analysis (FEA), a computational technique, can be applied to assess bone strength[25–27]. Additionally, high-resolution peripheral QCT (HR-pQCT) can provide information about trabecular architecture and cortical porosity at the distal forearm and tibia, to supplement central QCT measurements, and can also be used to assess bone erosions of the hand[28]. Opportunistic screening using clinical CT could help to identify patients at a high risk of osteoporotic fracture[29,30], and clinical CT imaging is also now being used to assess muscle and soft-tissue parameters to improve fracture risk prediction[31]. We discuss these developments in more detail in this section.

Quantitative CT

QCT of the spine and hip is widely used in research studies and clinical trials of osteoporosis. QCT quantifies BMD via a second calibration from CT to volumetric BMD values (measured in mg/cm^3)[24], usually using an in-scan calibration phantom (FIG. 3). In clinical applications, precision errors are comparable with those of dual X-ray absorptiometry (DXA)[25,32,33], the clinical gold standard in osteodensitometry[34]. DXA is widely used for the diagnosis of osteoporosis, but it is a projectional technique that provides only areal BMD (measured in g/cm^2). A key feature of QCT is that, unlike DXA, it distinguishes the trabecular and cortical bone compartments. Trabecular bone, in particular of the vertebrae, is metabolically more active than cortical bone; therefore, changes in trabecular BMD, for example, induced by anti-osteoporotic medication, can be detected with QCT earlier than with DXA[35]. The separate assessment of cortical bone is important because of its independent contribution to bone strength and fracture risk, as well as its importance to understanding age-related changes of bone geometry and density and to exploring differential effects of pharmaceutical interventions[36].

State-of-the-art spiral CT offers almost isotropic spatial resolution (that is, the same resolution in all three dimensions of space; see also BOX 1) of up to 0.5 mm (REF.[37]). Standard clinical QCT, however, uses a slice thickness of 1 mm or 1.25 mm (REF.[38]), and specific reconstruction kernels are used to balance image noise and radiation exposure. At this resolution, the assessment of the thin (200–500 µm) cortical shell of the vertebral body or thin portions of cortical bone in the femoral neck are associated with partial volume artefacts. As a consequence, cortical thickness is overestimated and cortical BMD is underestimated[39,40]. Defining the endosteal border is also difficult, because the transition from the cortical to the trabecular compartment, which is characterized by increasing porosity, is continuous[41]. Several advanced cortical segmentation methods developed over the past few years have reduced accuracy errors of cortical thickness and BMD measurements[42–45].

QCT is the basis for in-vivo FEA, a computer-based simulation of the strains and stresses induced by mechanical loading of an object (such as bone)[46]. Using this method, bone is described as a connected set of small geometrical elements to which constant elastic properties are assigned. The elastic properties of each element are derived from the corresponding BMD values from the QCT scan. FEA integrates bone density and geometry and is used to calculate an integral parameter of bone strength: if the bone strength is too low for a given external load, the bone will fracture. Mechanical experiments in which bones are loaded until they fracture have indeed shown that bone strength at the hip or vertebra as determined by FEA is a better predictor of failure load than corresponding DXA or QCT measurements of BMD[25]. In vivo, however, similar to QCT, FEA only showed better fracture prediction than DXA at the spine and not at the hip[26,27].

Interestingly, several QCT studies found a BMD-independent contribution of cortical geometry to hip fracture risk[25,47–52]. Although to our knowledge a multivariate analysis of BMD, cortical thickness and strength has not been published yet, FEA might not be required in addition to combined BMD and cortical geometry data. Also, vertebral compressive strength has been estimated as a linear combination of integral BMD and

Fig. 2 | **Technical principles of bone imaging modalities. a** | Magnetic resonance imaging (MRI) is based on the application of a strong static magnetic field for polarization of hydrogen molecules, switching of magnetic gradient fields for spatial signal encoding and application of radiofrequency (RF) waves to excite magnetic spins in the sample. RF receive coils detect the RF signal from the sample. The entire MRI system is contained in an RF-shielded cabin. Contrast in MRI results from the density of hydrogen molecules and other magnetic tissue properties in the sample. Solid bone appears hypointense, and muscle, bone marrow and blood vessels have high positive contrast. **b** | CT is a 3D imaging modality based on the absorption of X-ray radiation. In clinical CT, an X-ray source together with beam-optimizing elements (filter and collimator) and a detector array are arranged in a rotating gantry to collect projections from a large number of angles, from which the final images are reconstructed using a mathematical process. As in standard radiographs, bone appears white, soft tissue appears grey and air appears black. **c** | µCT is CT with a spatial resolution below 100 µm. Several different geometries exist. In the example shown, the sample rotates while the detector and X-ray source are at rest. **d** | In contrast to conventional µCT, X-ray microscopy (XRM) uses a secondary optical resolution of the primary X-ray image, which is achieved by transforming the scattered X-rays into visible light via a scintillation screen. This primary image is optically magnified by a second stage. **e** | With light-sheet fluorescence microscopy (LSFM), excitation laser beams of defined wavelengths are formed optically into a sheet of light that generates fluorescence in the sample, which is detected from a 90° angle by a camera. **f** | Two-photon laser scanning microscopy (TPLSM) uses a femtosecond pulsed laser to produce near infrared radiation (NIR) that excites fluorophores within tissues. **e** | With LSFM, entire bone can be visualized with autofluorescence. **f** | With TPLSM, cortical bone can be visualized by second harmonic generation (SHG) signals (a specific intrinsic contrast mechanism; grey). **g** | Confocal laser scanning microscopy (CLSM) uses constant wave visible lasers for specific fluorophore excitation. The light emitted from the sample is channelled through a narrow pinhole to ensure that only in-focus light is detected. In CLSM, visualization of cortical bone can be done by reflection contrast. In LSFM, TPLSM and CLSM, staining with specific fluorescently labelled antibodies enables visualization of defined structures; here, blood vessels are labelled with anti-CD31 (red). Scale bar (parts **f** and **g**): 100 µm. CCD, charge coupled device.

Table 1 | **Methods for imaging bone and its blood supply**

Method	Imaging applications	Advantages	Disadvantages	Refs
X-ray-based imaging				
Clinical CT	• Hard-tissue contrast • Intravital/in-vivo bone imaging • Ex-vivo bone imaging	• Isotropic resolution of 0.5 mm • Short scan time (10–20 s) • Quantitative CT provides measurement of BMD at the spine and hip, and enables separate assessment of cortical and trabecular bone • Whole-body clinical CT is routinely used for radiological diagnosis	• Lower soft-tissue contrast than MRI • Radiation exposure	24,36,72
HR-pQCT	• Hard-tissue contrast • Intravital/in-vivo bone imaging • Ex-vivo bone imaging	• Isotropic resolution of ~100 µm • Enables 3D imaging of bone microarchitecture and volumetric BMD in vivo • Provides information about trabecular architecture and cortical porosity at the distal forearm and tibia	• Lower soft-tissue contrast than MRI • Radiation exposure • Limited to scanning extremities • Long scan times (~2–3 min) • Access to scanners is limited	24,36,72
SR-CT	• Hard-tissue contrast • Ex vivo bone imaging	Use of a high-brilliance X-ray source (from a synchrotron) provides very high spatial resolution in bone, as fine as a few tens of nanometres	• Building and maintaining a particle accelerator ring incurs high costs • Radiation damage due to high-energy X-rays • Very limited beamtime (i.e. time available at large SR beam installations)	20,87,90
XRM	• Hard-tissue contrast • Ex vivo bone imaging	• Laboratory-based, non-synchrotron imaging • Achieves sub-micrometre resolution at a long working distance	• High radiation dose • Sensitive to motion • Not suitable for use in humans	11,20,82,212
Magnetic resonance imaging				
MRI	• Soft-tissue contrast • Intravital/in-vivo imaging • Ex-vivo imaging • 2D tomographic views and 3D imaging data can be reconstructed	• Excellent soft-tissue contrast • Imaging of cartilage and bone marrow with high spatial resolution (100 µm) • Structural and functional information on vasculature and blood flow • Suitable for clinical use • Non-invasive, non-ionizing • Whole-body imaging is possible • Can be used for repeated measurements in longitudinal studies	• Limited spatial and limited temporal resolution compared with the other imaging methods in this table • Long data acquisition times	11,101, 104,112,116, 121,123,129
UHF-MRI	• Soft-tissue contrast • Intravital/in-vivo imaging • Ex-vivo imaging • 2D tomographic views and 3D imaging data can be reconstructed	• Higher sensitivity and improved image contrast compared with MRI at lower field strengths when imaging bone and cartilage microarchitecture • Non-invasive, non-ionizing • Visualization of blood flow and determination of flow direction and flow rate • Suitable for use in humans • Improved resolution over MRI (50–80 µm)	• UHF-MRI of bone requires the use of dedicated radiofrequency antennas and sequences (because trabecular and cortical bone provides only a low MRI signal) • Long data acquisition times	11,101, 104,112,116, 121,123,129
Microscopy				
LSFM	• Soft-tissue contrast • Multi-colour imaging • Ex-vivo bone imaging	• Very fast 3D reconstruction with very good resolution (1–5 µm) • Mesoscopic imaging of whole organs (of small animals) or small human tissue sections (e.g. lymph nodes or bone fragments) • Multi-colour immunofluorescence	• Requires clearing with complex treatments to achieve tissue transparency • No live imaging possible (in animals or humans) • Requires tissue fixation • Shrinkage of soft tissue occurs with solvent-based clearing	11,136, 137,213,214
CLSM	• Hard-tissue contrast • Soft-tissue contrast • Multi-colour imaging • Ex-vivo bone imaging • 3D imaging	• Deep penetration into live tissue • High-resolution 3D imaging (200 nm) • High contrast of bone • High spatial and temporal resolution of live cells and blood flow	• Invasive procedures are required for imaging • Not suitable for clinical use • Not suitable for long-term live cell imaging in bones • Sectioning is required to study bone internal structure	11,157, 183–191, 193,197
TPLSM	• Hard-tissue contrast • Soft-tissue contrast • Multi-colour imaging • Intravital/in-vivo imaging • Ex-vivo imaging	• Deep penetration into live and fixed tissue • High contrast of bone • High spatial resolution (down to 200 nm) and temporal resolution of live cells and blood flow	• Invasive procedures are required for imaging • Not suitable for clinical use	11,157, 183–191, 193,197

BMD, bone mineral density; CLSM, confocal laser scanning microscopy; HR-pQCT, high-resolution peripheral quantitative CT; LSFM, light sheet fluorescence microscopy; SR-CT, synchrotron radiation CT; TPLSM, two-photon LSM; UHF-MRI, ultra-high-field MRI; XRM, X-ray microscopy

Box 1 | **Resolution**

Resolution is the ability of an imaging system to optically separate two contrasting items in close vicinity. The maximum resolution defines the closest distance between two items while still being distinguishable. The naked human eye has a resolution of down to 150 µm at a distance of 25 cm. Classical microscopes have a maximal resolution of ~200 nm. Other imaging modalities discussed in this Review have resolutions down to 1 nm (for example, electron microscopy) or only tens of micrometres (for example, magnetic resonance imaging). The range of possible resolutions by the different imaging modalities is summarized in FIG. 3. For comparison, the Hubble space telescope has a maximum resolution of 85 m on the surface of the Moon (too low to see the remnants of the Apollo missions).

Isotropic spatial resolution describes identical spatial resolution in X and Y directions (2D) or X, Y and Z directions (3D). This term is often falsely used if an image has square pixels or cubic voxels. For example, CT scanners and also optical microscopes typically have an isotropic in-plane resolution of the reconstructed images (X–Y plane), but in the scan direction (in CT) or along the imaging axis into the depth of the sample (in microscopy), the spatial resolution usually differs.

cross-sectional area, two parameters that can easily be determined from QCT alone[53,54]. A new promising research topic is the combined analysis of bone and soft-tissue parameters from CT scans[31,55–58]. In a 2018 study, the combination of relative volume of adipose tissue in the upper thigh and a parameter describing the distribution of extramyocellular lipids within the thigh muscles discriminated between patients with and those without hip fracture with the same accuracy as trochanteric trabecular BMD combined with cortical thickness of the femoral neck[31].

Routine clinical CT scans have been used to assess BMD and fracture risk[29,30]. This technique is termed opportunistic screening, and could be useful in identifying patients at a high risk of fracture. One challenge of opportunistic screening is the lack of calibration phantoms in routine CT examinations. A number of alternative calibration options have been proposed, such as asynchronous calibration, in which a BMD standard is scanned separately from the patient, and internal calibration, which uses air, internal organs and the aorta as reference materials for calibration. Good agreement between simultaneous and scanner-specific internal calibration was reported in a 2017 study, but the exact details of the methods used were not published[59].

Clinical high-resolution CT

For imaging bone, the primary aim of clinical HR-pQCT is the assessment of the trabecular structure (FIG. 4) and, increasingly, of cortical porosity. The accuracy of cortical thickness measurements also increases with higher spatial resolution. The XtremeCT I (Scanco Medical, Brüttisellen, Switzerland) device was introduced for high-resolution in-vivo scanning at the forearm and tibia[60–62]. This device uses an isotropic voxel size of 82 µm, resulting in a spatial resolution of ~120 µm, with a scan time of 3 min (for a 1-cm scan)[63]. The second-generation XtremeCT II provides higher spatial resolution, using a voxel size of 61 µm and a reduced scan time of 2 min[64]. The long scan times require patients to be carefully positioned and instructed in order to avoid motion artefacts, which occur if the arm or leg is moved by 100 µm during the scan.

Partial volume artefacts
Occur when a CT voxel encompasses tissues with different absorptions, so that the beam attenuation represents the average value of these tissues.

With XtremeCT I, histomorphometric parameters are determined from a measurement of bone volume fraction and apparent trabecular number[65]. The higher spatial resolution of the XtremeCT II allows for a direct quantification of the trabecular structure independent of trabecular BMD[66].

HR-pQCT can directly detect large cortical pores of ~40 µm in diameter (FIG. 4). When mineralization is stable, a decrease in cortical BMD is largely attributable to an increase in the number and size of pores[67]. Porosity increases with age[68] and is increased in patients with type 2 diabetes mellitus[69,70]. However, whether porosity-related parameters, such as pore size and distribution, provide clinical information not obtainable from a simple cortical BMD measurement is unknown. Furthermore, most cortical pores are small and therefore cannot be detected directly, even with HR-pQCT.

Currently, HR-pQCT is predominantly used as a research tool in osteoporosis, since fewer than 100 scanners are active worldwide[71]. Clinical imaging of bone microarchitecture with HR-pQCT has been reviewed elsewhere[62,72]. Another interesting application of HR-pQCT is the quantification of bone erosions of the metacarpal and phalangeal joints (FIG. 4)[28]. Erosions emerge early in the course of rheumatoid arthritis (RA) and changes in their size are associated with the progression of RA[73]. Owing to the high spatial resolution of HR-pQCT, erosion-volume estimation is much more accurate with HR-pQCT than with radiography or MRI[74]. Also, erosion shapes can be assessed[75].

Cone beam CT (CBCT) scanners, originally developed for dental applications, use large flat-panel detectors and offer a spatial resolution between that of clinical whole-body CT and HR-pQCT devices[76]. Dedicated CBCT scanners have been developed for scanning of the peripheral skeleton[77]. One interesting application is knee CT in a standing position[78]. Bone structure analysis using CBCT has mostly been reported in the dentomaxillofacial field, but, owing to excellent spatial resolution and short scan times, CBCT is highly relevant to peripheral bone microstructure analysis. Initial promising results have now been reported[79].

Experimental X-ray imaging

Experimental high-resolution X-ray-based tomographic imaging has been applied to the imaging of biological tissues, particularly bone, since the 1990s[80]. Until the advent of this approach, tomographic imaging in laboratory environments was carried out either with QCT systems at low resolution and using large samples or with scanning electron microscopy, which can use an additional focused ion beam for slicing and subsequent tomographic imaging of very small samples at high resolution[81–84].

Use of these systems left a 'resolution gap'; that is, bone features of sizes ~50 nm to 10 µm could not be assessed in the laboratory. Although clinical QCT systems are invaluable for the investigation of trabecular bone architecture[36,85,86], their resolution greatly limits their use for the visualization of finer structures within bone, such as the LCN or bone vascular systems (FIG. 1).

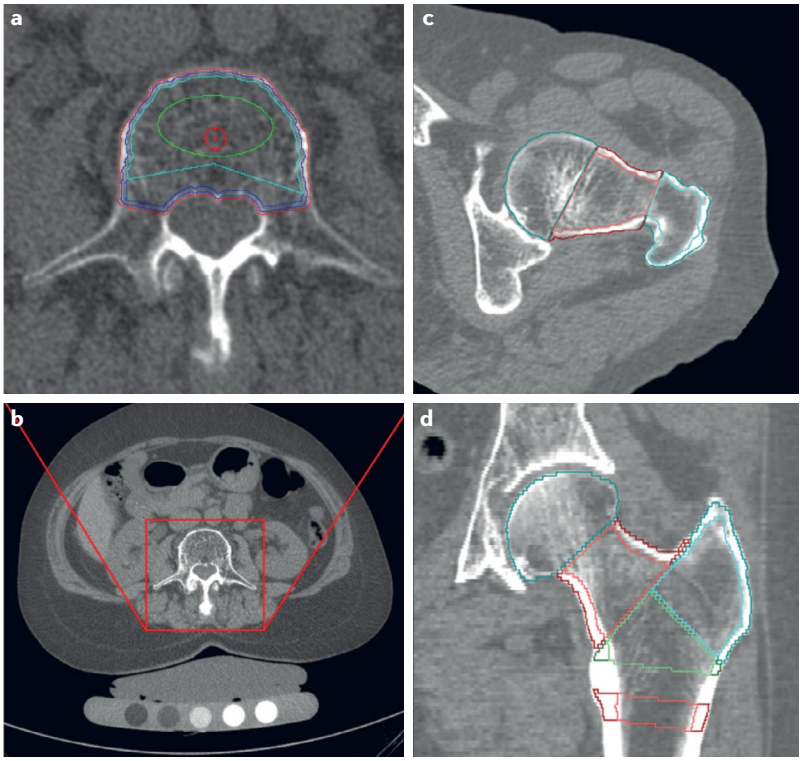

Fig. 3 | **QCT in the clinic.** Analysis of the spine (**a** and **b**) and the hip (**c** and **d**) using quantitative CT. **a** | Reconstruction of the scan in the red square in **b**, centred on the vertebral body showing the periosteal surface (red contour), the endosteal surface, which defines the cortical compartment (outer blue contour), the border between the subcortical and trabecular compartments (inner blue contour), and traditional elliptical and osteo-trabecular volumes of interest (VOIs) (green and cyan contours) excluding posterior vessels. 3D segmentation by Medical Image Analysis Framework software (MIAF; University of Erlangen). **b** | Axial image of the spine. A calibration phantom is positioned below the patient. **c** | Axial and **d** | coronal reformations of a CT scan of the femur (calibration phantom not included in this reconstruction) showing periosteal and endosteal surfaces of head, neck, trochanter, intertrochanter and shaft VOIs. 3D segmentation by MIAF.

Until ~10 years ago, the resolution required to assess such structures could only be achieved by use of synchrotron radiation CT (SR-CT). Given the enormous complexity of this method (TABLE 1), information on the fine structure of bone was limited to a small set of SR-CT studies[87,88]. With the introduction of XRM, this situation has fundamentally changed (see below). However, the few examples available make it obvious that experimental high-resolution X-ray-based imaging has enormous potential to visualize the 3D ultrastructure of calcified bone with unprecedented detail. This approach is expected to provide new insights into the physiology of bone under physiological and disease conditions. In particular, bony compartments for cells or blood vessels are likely to be understood in greater detail with respect to their overall shape and dynamics in response to environmental perturbations.

Synchrotron-based imaging

SR-CT uses X-ray-based CT coupled with a powerful source of X-rays and allows for microscopic X-ray imaging with resolutions as fine as a few tens of nanometers[87]. Thus, SR-CT studies have made essential contributions to a more comprehensive understanding of the fine structure of bone. Further development of this approach led to scanning coherent diffraction microscopy (also called ptychography), which can achieve a spatial resolution of 10 nm[89]. This ultra-high-resolution imaging relies on the use of hard X-ray irradiation (that is, high-photon energy X-rays with extra-short wavelengths) and cannot, therefore, be applied to in-vivo analyses owing to a very high local radiation dose within the studied material. For ex-vivo studies, however, synchrotron-based imaging has been used to obtain a multifaceted picture of the fine structure of bone[90]. These techniques have been used to produce detailed images of the LCN or bone vascular networks and the interdigitated osteocyte lacunae within these networks[82,87,91]. Moreover, SR-CT analyses have contributed to a detailed understanding of additional bone features, such as the size and position of acellular mineral particles in bone[92], as well as the distribution of collagen fibrils and their orientation and deformation mechanisms[90,93,94].

Nanoscale X-ray microscopy

In-depth analyses of the hierarchical architecture of bone, as pioneered in SR-CT studies, can now be achieved in routine analyses following the advent of laboratory-based XRM. XRM bridges the aforementioned resolution gap between QCT and scanning electron microscopy, while at the same time enabling the non-destructive 3D imaging of large specimens. X-ray microscopes are now available that provide the means of quantitatively assessing features such as the vascular and osteocyte systems with resolutions as fine as 700 nm (for samples sized ~10 cm^3 to <1 mm^3)[11], and features such as the LCN can be assessed using X-ray microscopes that can achieve resolutions as fine as 50 nm (for samples up to 1 mm^3 volume, see FIG. 1)[84]. The resolution gain of XRM in comparison with QCT systems is attributable to geometrical magnification, which determines QCT resolution, as well as an additional optical magnification (FIG. 2).

The integration of these advanced X-ray optics overcomes the standard trade-off between sample size and resolution in conventional QCT instrumentation[95,96]. The introduction of Fresnel zone plates to focus X-ray radiation permits laboratory-scale XRM that features resolutions previously provided only by SR-CT[12,96–100]. XRM maintains sub-micrometre resolution and high contrast at a large working distance (that is, the distance between the X-ray source and the object being investigated) (FIG. 2), which enables the use of in-situ and in-vivo testing capacities such as environmental chambers or mechanical challenging units[97]. Hence, in the future it might be possible to investigate bone under stress or physiological conditions with XRM-level resolution.

Laboratory-based XRM has been used to investigate the vascular system in cortical bone[11] and even the LCN. In a preliminary XRM study, statistical size quantification of >1,000,000 osteolacunae in wild-type mice and mice genetically predisposed to developing osteoporosis indicated that changes in the fine structure of bone (namely, a substantially larger overall volume of osteolacunae) were apparent in osteoporotic mice at a very

Fresnel zone plate
A device to focus X-rays, consisting of a group of radially symmetrical, alternately opaque and transparent rings (zones); an X-ray wave hitting the zone plate diffracts around the opaque zones, and the zones can be engineered in such a way that the waves are focused.

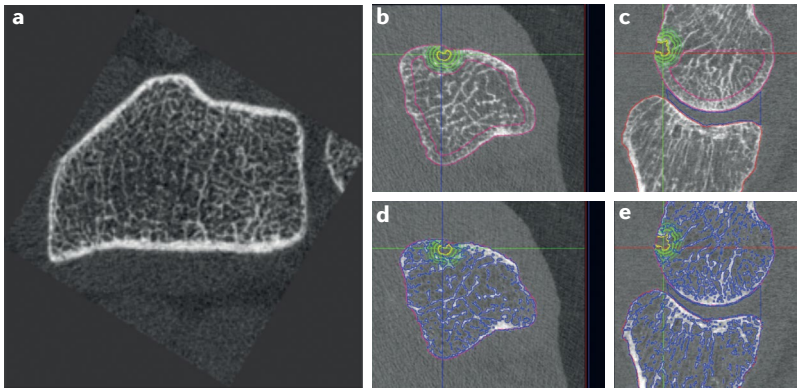

Fig. 4 | **HR-pQCT in the clinic.** Analysis of the distal radius (**a**) and metacarpophalangeal (MCP) joints (**b**–**e**) showing bone erosions in a patient with rheumatoid arthritis using high-resolution peripheral quantitative CT (HR-pQCT). **a** | Selected axial slice demonstrating the excellent spatial resolution achieved with HR-pQCT, which is adequate for structural analysis of the trabecular network. **b** | Axial and **c** | coronal reconstructions of the second MCP joint, selected from a standard scan that included second to fourth MCP joints. Periosteal bone contours (pink), the trabecular volume of interest (VOI) of the metacarpal head (red) and joint space VOI (blue) are visible. The contour of the erosion is highlighted in yellow. Contours of four concentric VOIs around the erosion are used to measure bone mineral density of the sclerotic rim of the erosion. **d** | and **e** | Reconstruction of the same scans as shown in **c** and **d**, showing the contours of individual trabeculae (blue).

early stage of disease, prior to any macroscopic bone alterations such as bone loss (A.G., L.K., S.C. and G.S., unpublished data).

Magnetic resonance imaging

As an in-vivo, whole-body imaging modality, MRI is routinely used in clinical diagnostic imaging and can, in principle, provide 2D and 3D imaging of all joints in the human body. Whereas CT can provide high-resolution, high-contrast cross-sectional images of bone structure, the strength of MRI in imaging the musculoskeletal system is that it provides excellent contrast of soft tissues, such as muscle, adipose tissue, tendons and cartilage, and also delivers structural and functional information on vasculature and blood flow[101].

Unlike CT, which uses ionizing radiation (X-rays), MRI employs strong magnetic fields measured in Tesla (T) and radiofrequency (RF) waves to excite ^{1}H protons (or other nuclei) in the tissue under evaluation (FIG. 2). Clinical MRI today is mostly performed using systems operating at a static magnetic-field strength of 1.5 T and 3 T. The achievable spatial resolution of 3-T MRI can be comparable with clinical CT applications[102]. With further developments in superconducting magnet technology, ultra-high-field (UHF) MRI systems operating at 7 T or even 9.4 T have been realized for use in human imaging research[103]. Depending on the specific application, the spatial resolution of UHF-MRI can even surpass that of whole-body clinical CT. The first 7-T MRI system for human use was installed in 1999; today, about 70 installations are operational around the world[104].

Ultra-high-field MRI

The rationale behind the trend towards UHF-MRI is that the signal-to-noise ratio (SNR) in MRI increases with the strength of the magnetic field that is used for polarization of the sample; therefore, the inherently high SNR of UHF-MRI can support MRI with high spatial resolution while reducing image noise and maintaining high image quality[101]. UHF-MRI thus provides higher sensitivity and improved image contrast compared with MRI at lower field strengths. These inherent advantages of UHF-MRI, however, come at the expense of the increased technical challenges associated with magnet construction. An additional physical challenge of UHF-MRI is associated with non-uniform RF excitation in body tissue, which limits signal penetration depth and image homogeneity[101]. As a consequence, multi-channel RF coils need to be developed for selected purposes and body regions to obtain the best possible SNR, spatial resolution and image quality.

UHF-MRI in imaging of the musculoskeletal system. 7-T UHF-MRI has demonstrated increased spatial resolution and image contrast, beyond that of routine MRI applications, when imaging cartilage and bone microarchitecture[105]. UHF-MRI of the hip joint[106] and the knee[107] has achieved spatial resolution of $230 \times 230 \times 1{,}000\ \mu m^3$ (REF.[106]). Lazik et al.[108] have investigated 7-T quantitative UHF-MRI of the hip in healthy volunteers and have optimized a multi-contrast T1, T2 and T2* mapping MRI protocol (BOX 2) to provide structural and quantitative evaluation of hip cartilage[108]. This protocol has also been applied to the assessment of patients with hip cartilage transplants and, when compared with 3-T MRI, provided superior image quality, assessment of cartilage transplants and contrast[109]. Quantitative 7-T MRI with T2 mapping has also been used to show compositional differences between ankle and knee cartilage[110].

With a focus on high-resolution MRI of the trabecular bone microarchitecture, 7-T UHF-MRI was used to investigate the trabecular structure of tibiae in healthy volunteers[111,112]. In a subsequent study that used 7-T MRI to investigate trabecular bone microarchitecture of the distal radius in 24 healthy individuals[113], achieving a spatial resolution of $169 \times 169 \times 1{,}000\ \mu m^3$, 7-T UHF-MRI detected age-related differences in trabecular microarchitecture, suggesting the potential to investigate fracture risk or treatment response[113].

Expanding on the structural aspects of trabecular bone microarchitecture, 7-T UHF-MRI in vivo studies of tibial bone have combined high-resolution imaging information with subsequent micro-FEA[114,115], to provide insight into structural and mechanical parameters and how they affect bone competence in vivo. In the context of osteoporosis, UHF-MRI and FEA studies might enable earlier detection of disease-based or treatment-based effects on bone[114].

Direct imaging of bone structure with MRI is hampered by the low water content in bone and very fast T2* signal decay[116,117]. Therefore, work in the aforementioned studies[111–114] and efforts to depict bone microarchitecture by MRI have relied on negative trabecular contrast. In MRI, trabecular bone provides only very low signal intensity, whereas bone marrow in the trabecular spaces, interstitial fluids and tissue provides high signal intensity, resulting in the indirect visualization of the trabecular structures, rendering trabecular bone dark and surrounded by brighter signals[111–114,116,118,119].

Tesla
(T). An SI unit that describes the strength of a magnetic field. 1 Tesla is ~20,000 times larger than Earth's natural magnetic field.

Signal-to-noise ratio
(SNR). Describes the ratio of the power of an anticipated signal to the power of background noise.

Box 2 | **Quantitative MRI**

In magnetic resonance imaging (MRI), the term relaxation describes how the spin magnetization in tissues changes over time. Following spin excitation in an MRI experiment, relaxation is determined by how quickly the excited protons in different tissues return from the excited state to the equilibrium state. Relaxation can be described by one of three different time constants: T1, T2 or T2*. Water protons in different tissues have different T1, T2 and T2* values, which are the main determinants of tissue contrast on magnetic resonance images[215].

The dominating contrast on T1-weighted MRI is the effect of the longitudinal (or spin-lattice) T1 relaxation of different substances. On T1-weighted images, tissues with short T1 times, such as fat or bone marrow, are shown with a high signal intensity. On T2-weighted MRI, the dominating contrast is the effect of the transverse (or spin–spin) T2 relaxation of different tissues. T2-weighted images show high signal intensity for substances with long T2 times, such as cerebrospinal fluid or oedema. T2* contrast also describes the transverse relaxation, but reflects minor heterogeneities in the magnetic field. For most MRI experiments, this 'real' T2* relaxation dominates the spin–spin relaxation. The T2* relaxation time is always shorter than the T2 relaxation time. MRI sequences with T2* contrast use short echo times (that is, short time intervals between spin excitation by radiofrequency signals and signal (echo) readout in the MRI sequence) to capture the fast T2* signal decay of tissues such as trabecular bone, tendons and menisci.

T1, T2 and T2* mapping is a quantitative MRI technique to determine and measure the T1, T2 and T2* relaxation times of different tissues for each given pixel or voxel. Such quantitative mapping provides greater sensitivity for the detection and measurement of even small changes in relaxation times than conventional T1-, T2- and T2*-weighted MRI sequences.

For direct imaging of bone, a new group of MRI sequences has been developed to provide very fast signal readout to capture magnetic resonance signals from cortical and trabecular bone, despite their fast T2* signal decay. The application of ultra-short echo time[120,121] and zero echo time[116] techniques with UHF-MRI provides very high spatial resolution and high contrast of bone microstructure.

As well as the use of special MRI sequences, RF coils are a key component in UHF-MRI of the skeletal system and bone structure. The design and quality of transmit–receive RF coils in UHF-MRI critically determine how much SNR, signal penetration depth and signal homogeneity can be provided at the region of interest to support high spatial resolution and high-quality MRI. Several designs for such coils have been developed. One example is an eight-channel transmit–receive body RF array coil. This 7-T MRI coil for imaging of the abdomen and pelvis consists of eight independent transmit–receive antenna elements that form an array antenna and it has been applied to investigate hip cartilage[108,109,122]. Likewise, a Helmholtz pair coil has been suggested for 7-T imaging of the distal tibia[112] and an eight-channel transmit–15-channel receive array has been developed and evaluated for 7-T UHF-MRI of the shoulder[123].

UHF-MRI in imaging of bone blood supply. Although imaging of the trabecular microstructure and cartilage has been an active field of MRI research over the past decade, imaging of the blood supply of the skeletal system is a rather new discipline[11]. In a 2019 study, 7-T UHF-MRI was used to explicitly visualize blood vessels in human long bones[11], using 7-T whole-body MRI with an eight-channel transmit–receive/7-channel receive RF array. For high-resolution imaging, T1-weighted, fat-saturated pulse sequences were acquired in 2D and 3D. Additionally, a time-of-flight magnetic resonance angiography (TOF MRA)[124] sequence was used to visualize and distinguish the direction of blood flow. This study enabled the main internal and external blood supply of long bones to be shown using UHF-MRI at a spatial resolution of $140 \times 140 \times 500\,\mu m^3$ for the first time, to our knowledge[11].

Outlook for UHF-MRI in imaging the musculoskeletal system and its blood supply. From the work described in the previous section[11] and a 2017 study demonstrating very-high-resolution ($150 \times 150 \times 150\,\mu m^3$) TOF MRA of human intracranial vessels obtained using 7-T UHF-MRI with prospective motion correction[125], it seems that the spatial resolution needed for the visualization of the capillary blood supply of human bones is within reach. Fundamentally, UHF-MRI systems with even higher magnetic field strengths provide better SNR to further increase the spatial resolution while maintaining high image quality and not being limited by image noise. Presently, experimental UHF-MRI systems with a small central opening (bore) operate at field strengths up to 21.1 T (900MHz resonance frequency)[126], enabling spatial resolutions as fine as $50 \times 50 \times 50\,\mu m^3$ (REF.[127]). The current limit for human UHF-MRI is 10.5 T; two MRI systems operating at 11.7 T are under construction[103]. Theoretical considerations, simulations and scientific evidence suggest that 14-T and 20-T human MRI systems might be the next feasible targets[101,128,129]. Once MRI systems at these magnetic field strengths are realized, one can expect further improvements in spatial resolution, sensitivity and image contrast. However, physiological limits, such as unpleasant temporary effects on the neuronal system (for example, induction of vertigo or nausea or optical phenomena within the magnetic field), will ultimately limit the maximum magnetic field strength that will be tolerated by humans[101,103,128].

In the future, MRI together with X-ray-based imaging will be instrumental in obtaining a detailed map of static structures and dynamic processes in both hard and soft components of bones within experimental animals and humans.

Optical imaging

So far, we have discussed approaches that use X-rays and magnetic fields as frequently used methods for bone imaging. Another key approach involves the application of low-energy visible photons for optical microscopy, which is also the only way to produce multicolour images and hence offers great versatility for targeted imaging in the analysis of bone and its blood supply. Whereas X-ray-based imaging and MRI are important for visualizing the main architecture of bones and their blood vessel systems, optical imaging enables visualization of single cells and subcellular structures. Together, these techniques make it possible for us to describe the functions of bone, bone marrow and their cellular constituents from the macroscale to the nanoscale.

Microscopy is the most widespread method of scientific imaging. It uses visible light to illuminate a sample

Ultra-short echo time
Technique used in MRI sequences that enables visualization of tissues with very short transverse relaxation times by starting spatial encoding and data acquisition as soon as possible after the radiofrequency pulse.

Zero echo time
Technique used in MRI sequences that enables visualization of tissues with very short transverse relaxation times by starting spatial encoding before the radiofrequency pulse and starting data acquisition as soon as possible after the radiofrequency pulse.

Time-of-flight magnetic resonance angiography
(TOF MRA). An MRI technique used for high-resolution imaging of blood vessels, based on the principle that, when using short echo times, unsaturated blood entering the imaging slice gives a much higher (brighter) signal than the surrounding static tissue, which is saturated and thus remains dark.

Refractive index
(RI). A descriptor of how fast light propagates through a material, expressed as the ratio of the velocity of light in a vacuum to its velocity in that material.

and refractive optics to generate a highly magnified image with ~1,000× better resolution than the naked human eye[130]; advanced systems with super-resolution can achieve resolutions that are >10,000× better[131,132]. As natural tissue has very little endogenous contrast, distinguishing different structures requires samples to be stained, typically using fluorescent dyes (fluorescence microscopy)[23].

As with other imaging modalities, optical imaging involves a variety of technical concepts. As discussed in this section, LSFM and CLSM can be used to visualize the vascular system, and intravital TPLSM can be used to analyse the blood flow and cells in bone.

Light-sheet fluorescence microscopy

Owing to its high imaging speed, high penetration depth, and minimal light exposure, LSFM has emerged as a powerful tool for 3D imaging by the intrinsic optical sectioning of large biological samples[133]. The generation of a thin, focused light sheet perpendicular to the detection axis allows for high spatiotemporal resolution, high background rejection and low phototoxicity in the focal plane, thus facilitating long-term imaging of biological samples at the subcellular level (FIG. 2).

Since the first report of fluorescent imaging via LSFM in 1993, multiple technical improvements have been made[134]. Modern LSFM generates a sheet of light, for example, by using cylindrical lenses, which provide lower numerical apertures than conventional microscope objective lenses (FIG. 2). This improves the homogeneity of the light sheet over the entire sample, providing a larger field of view (FOV) and also enabling deep penetration[133,135]. Thus, the sample is illuminated from the side and imaged by, for example, a digital camera attached to magnifying optics at a 90° angle (that is, from the top). Excellent optical sectioning, even in thick specimens, is obtained by the selective illumination via the thin light sheet. 3D tomographic series are generated by moving the sample up or down in a fixed light sheet and taking a digital image at each new height. LSFM allows for the simultaneous detection of several fluorescent colours, hence enabling the fast multi-colour and high-resolution reconstruction of tissues[136,137]. LSFM is a rapidly evolving field with new approaches aimed at improving image resolution, speed of acquisition or sample size (reviewed elsewhere[138]). There are different ways of producing a light sheet. Digital scanned laser LSFM generates a sheet of light by rapidly scanning a laser vertically through the sample. As the laser is focused into a single diffraction-limited spot, no further optical elements are required to shape its intensity profile[135,139,140]. A scanned sheet of light has excellent resolution in the Z-plane, yet is limited in its optical sectioning capabilities and FOV, hence only allowing imaging of small samples such as single cells[133,140–142].

3D imaging of mesoscopic-scale samples (1 mm^3 to 1 cm^3 volume) requires a large FOV and deep imaging, but only moderate spatial resolution. Thus, studies of entire murine organs, for example, mainly use LSFM systems with cylindrical lenses for light-sheet generation (FIG. 2), resulting in centimetre-sized FOVs. The optical penetration depth in biological samples is mainly affected by light scattering and aberrations due to heterogeneities in the refractive index (RI) at the intracellular and inter-cellular levels[143], which lead to the opacity of most vertebrate tissues. Hence, the application of LSFM for mesoscopic imaging requires complex treatments to render organs transparent, collectively called 'clearing'[136,144]. Chemical clearing, based on RI matching, enables the imaging of large, fixed samples with high spatiotemporal resolution[137,145,146]. Numerous clearing protocols are available to achieve tissue transparency by using high-RI aqueous solutions, hyperhydrating liquids or organic solvents[136].

The RI of murine bone ranges from 1.555 to 1.564, dependent on mineralization, and the fastest way to yield clear bones suitable for LSFM analysis is to use organic solvents[136,143,147]. Organic solvent-based clearing techniques enable optical clearing of entire organs and bones within hours to a few days[136,137,148].

However, many organic solvents are difficult to use because of their toxicity. Moreover, endogenous fluorescent proteins are bleached during the clearing process or their fluorescence is preserved for only a few days[11,136,148–151]. Developments to address these problems include the identification of a potent non-toxic clearing reagent[137] and improvements in protocols to enable the long-term preservation of endogenously expressed fluorescent proteins[152]. Additionally, newly established staining strategies (as alternatives to classical whole-mount immunochemistry) have now made hard-tissue samples, such as bones and teeth, accessible for total fluorescence labelling[137,145,146]. This development is noteworthy, as antibodies fail to penetrate the hard cortical bone tissue in classical whole-mount setups. Hence, most LSFM studies of bones were restricted to flushed bone marrow plugs or thick tissue sections[153–155], and thorough LSFM investigation of intact long bones and their closed circulatory loop through the hard bone shell was impossible.

Applying the latest technical advances in bone clearing and LSFM, a vascular system in the cortical bone tissue of mice and humans that was previously incompletely described or overlooked has now been identified and characterized. This system, which has also been assumed to exist in rat bones[156], consists of hundreds of arterial and venous capillaries that directly connect the periosteum with the endosteum through the cortical bone; these capillaries are termed transcortical vessels (TCVs)[11] (FIG. 5). Similar structures have been found in the skull bone[157]. The TCV system is an important addition to the prevailing concepts of bone vascularization, which exclusively describe transitions between bone-marrow arteries and sinusoids with few entry or exit sites, while largely ignoring the morphological and functional characteristics of trans-cortical flow[158–160].

Although these findings substantiate the capability of LSFM for skeletal imaging, its mesoscopic imaging capacity does not enable the analysis of subcellular or molecular structures. Studies of direct cell–cell interactions or intracellular processes require much higher resolution, which can be achieved by use of laser scanning microscopes.

Confocal laser scanning microscopy

CLSM constructs images by scanning a laser across the specimen and detecting fluorescent light emitted from the sample. Use of a pinhole ensures that only light from the focal point reaches the detectors, hence enabling optical sectioning (FIG. 2). Successive imaging at different depths generates 3D volumes of the sample[161,162]. The high spatiotemporal resolution and multi-colour labelling of tissue structures makes CLSM an attractive and widely used tool for biological imaging. In bone research, CLSM can be used to study the vasculature and stem cell interactions in bone marrow[163]. The high-resolution 3D imaging achieved with CLSM enabled the identification of a new capillary subtype in specific areas of murine bones, which couples angiogenesis with osteogenesis[164]. Elegant studies identified a mechanism of endothelial cell proliferation and vessel growth in postnatal long bones[165] and facilitated the localization of adult haematopoietic stem cells, mainly in a perisinusoidal niche within the bone marrow[154,166]. A variation of confocal imaging was recently used to define a new type of skeletal stem cell[167].

However, CLSM has several disadvantages for bone imaging. First, the penetration depth is limited to a few tens of micrometres owing to scattering[168]. Physical sectioning is therefore required to study the internal structures of bones, which results in fragmentation and does not allow for the analysis of entire 3D structures (which can be achieved using LSFM)[169]. Furthermore, the necessary tissue fixation precludes the analysis of dynamic biological processes within bones and intense photobleaching limits detailed 3D imaging. Thus, CLSM is not well suited for long-term live-cell imaging in bones[139,168]. To overcome these limitations, TPLSM imaging is widely used and has become the gold standard for intravital studies of biological processes over the past few decades[170–172].

Two-photon laser scanning microscopy

Intravital imaging has become a workhorse approach for investigating cell function and physiological responses within a living organism. The main technology for this purpose is TPLSM (FIG. 2), which enables very good spatial and temporal resolution, functional imaging and deep penetration into natural tissue[173,174]. TPLSM exploits a physical effect in fluorescent molecules that only occurs at extremely high photon fluxes. Under these conditions, fluorophores can be excited by strongly

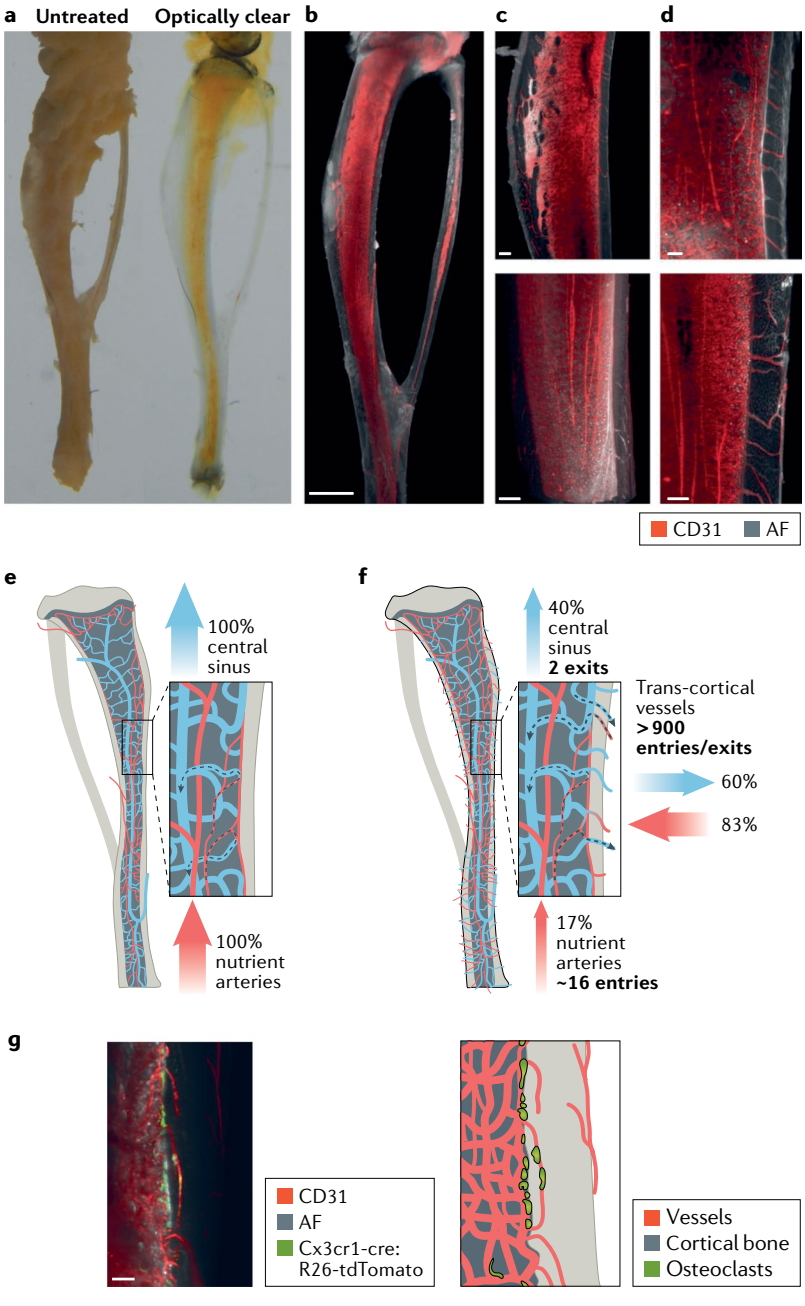

Fig. 5 | **3D whole-bone vascular analysis with LSFM.** **a** | Light-sheet fluorescence microscopy (LSFM) imaging of bones requires optical clearing to achieve tissue transparency. Here, a murine tibia before and after optical clearing based on ethyl cinnamate[137] is shown. **b** | CD31 labelling (red) enables the analysis of vessel organization in entire bones (autofluorescence (AF); grey). Scale bar: 500 µm. **c** | and **d** | Variable magnifications of the light-sheet microscope enable more detailed structural analysis of the bone vascularization. CD31-high arteries run longitudinally through the bone marrow and CD31-low sinusoids form a vascular meshwork in the bone marrow compartment. The cortical bone is crossed by trans-cortical vessels (TCVs), directly connecting the bone marrow with the periosteal vascularization. Shown in **c** is the dense bone marrow vascularization in two different areas of the tibia (upper and lower halves of the tibia; scalebar 200 µm) and in **d** the different organization of TCVs in the same areas of the tibia are shown (scalebar 100 µm). **e** | In the classical concept of bone vascularization, blood enters the bone at the metaphysis and the posterior diaphysis via nutrient arteries (red), and exits the bone at the anterior diaphysis and the posterior metaphysis via the central venous sinus (turquoise). **f** | LSFM studies of entire bones revealed a much more complex vascular system, whereby the main blood supply is not provided by the nutrient arteries and central venous sinus but by >900 TCVs, which transport ~83% of arterial and ~60% of venous blood through bone[11]. **g** | The cortical bone (AF, grey) as well as TCVs (CD31, red) are constantly remodelled by osteoclasts (Cx3cr1-cre:R26-tdTomato, green). Scalebar 100 µm. Images in parts **d–f** adapted from REF.[11], Springer Nature Limited.

Excitation maximum
A fluorophore fluoresces when its electrons absorb incoming photons (excitation) and then return to their original energy level, releasing excess energy in the form of a red-shifted photon; the excitation maximum is the optimal energy (i.e. wavelength or colour) that incoming photons must have to make this process most effective.

red-shifted, low-energy photons, whereas typically they would only respond to high-energy blue–green photons. In high photon flux, a chromophore can absorb two photons instead of one within an extremely short time frame. The energy of these photons then combines and the fluorophore reacts as if hit by one photon of roughly double the energy. As a result, it is possible to excite dyes characterized by excitation maxima within the blue–green range (for example, GFP or fluorescein isothiocyanate, a popular fluorescence molecule that has an excitation maximum of 488 nm), or with red-shifted photons of wavelengths beyond 800 nm, within the near infrared range (NIR[175]). NIR imaging has the advantage of superior tissue penetration compared with shorter wavelengths and, in variants with multi-photon excitation, can reach even deeper tissue levels[176].

Another advantage of TPLSM imaging is that it produces non-linear optical effects, termed second harmonic generation (SHG) and third harmonic generation (THG)[172,177]. In contrast to signal generation via fluorophores, the generation of SHG and THG signals enables label-free imaging without bleaching or heating artefacts[178]. In bone imaging, SHG signals enable the analysis of the composition, orientation and arrangement of mineralized collagen fibrils of the cortical bone, and THG signals are used for analysing the LCN[179,180]. SHG imaging can also be used for the visualization of bone-associated collagen-rich tissues, thus facilitating the analysis of articular cartilage damage in patients with osteoarthritis[181].

In addition to SHG and THG imaging, TPLSM with fluorescent labelling has been used to investigate the migration and function of immune cells within a multitude of soft tissues[182]. However, bone presents particular challenges owing to its mostly opaque hard shell, even when imaging in the NIR window. Nevertheless, methods have been developed to overcome these limitations and a wealth of information is available on the function of bone marrow and the cells within as well as blood flow[157,183–191]. However, the majority of these studies investigated a small patch of bone marrow in the murine skull, a flat bone with a blood supply different from that of long bones[192], which make up the majority of the skeletal system[193]. Whether haematopoietic functions of flat versus long bones also differ is the subject of intense discussions[194–196].

Intravital imaging for use in murine tibiae, developed to study neutrophil mobilization from haematopoietic stem cells in the marrow[186,188,193,197], showed that neutrophils, when mobilized by systemic injection of granulocyte colony-stimulating factor, entered blood vessels on the endosteal surface of the tibia and were flushed away within seconds through the cortex[188] through what appeared to be blood vessels directly crossing the entire compact bone. This observation served as the starting point for the discovery of the TCV system by LSFM (FIG. 5).

Image processing for in-vivo imaging

In-vivo imaging of bone at resolutions of 20 µm and below in humans is difficult. First and foremost, body motion during clinical imaging limits resolution to ~5 µm[198]. In interventional applications, a broad body of methods exists to tackle motion compensation, ranging from data-driven metrics[199] to novel machine-learning-based approaches[200]. These methods make it possible to compensate for motion of ~2 cm, thereby allowing for reconstruction of images with a resolution of ~400 µm[201]. The second major limitation, which applies to in-vivo applications of X-ray-based imaging, is the excessive radiation dose[198]. Again, methods from macroscopic imaging such as compressive sensing[202] and deep-learning image reconstruction[203,204] seem to be well suited to tackle this problem. Compressive sensing enables severe under-sampling of the CT acquisition, resulting in effective dose reduction of up to 60%. Used in combination with deep learning, even much higher dose reductions seem feasible. This is because in compressive sensing, the number of required measurements is drastically reduced on the basis of the assumption that relevant objects consist of only a few distinct materials[202]. For image formation using deep learning[203,204], the entire process of image generation is expressed as a trainable neural network: the network's structure can either be guided by physical properties of the image formation[62] or be driven by the similarity of a new image to previous measurements of the same type of object[63]. A third class of deep-learning reconstruction methods is aimed at reducing image artefacts[205]. Note that entire compressive sensing algorithms can also be expressed as neural networks[206]. Compressive sensing is the state-of-the-art approach in most CT or MRI settings. Deep learning and compressive sensing are thus compatible.

There is a general trend towards applying machine-learning methods for the quantification of bone images, with applications including the determination of skeletal age[207], analysis of metastases[208] and the prediction of other parameters that might not be immediately discernible to the human eye[209]. Hence, we expect more such correlated factors to be identified in the future using deep-learning techniques[210]. A major limitation for the application of deep-learning methods is the need for large amounts of data. This problem might be alleviated by the use of precision learning[211], which is a novel theory that allows the mixing of traditional signal processing and pattern recognition with deep learning.

Conclusions

The ultimate goal of any imaging approach in the biomedical field is to determine the position of every relevant element at any given time, with the spatial resolution required to answer all the scientific questions posed. As such, the measurement should ideally not interfere with the observed process. At present, no single technology is able to fulfil all these requirements. For example, intravital TPLSM has very good spatial and temporal resolution, yet requires highly invasive processes to enable observation of bone marrow; these processes induce inflammatory responses that change the observed phenomena. By contrast, LSFM and XRM can be used only on fixed tissues. Hence, the development of optical systems that avoid invasive procedures for intra-bone imaging[176] is highly desirable. UHF-MRI does not seem to influence the biological system, but

provides relatively poor resolution, even when pushed to its reasonably obtainable technical limits, while still being acceptable for human use. As well as further developments in imaging hardware, an important contribution to the above-defined goal might be the application of advanced approaches for the analysis of newly generated data.

All of these developments should ideally work in concert to enable ever deeper insight into the biology of bone in the future. The large societal burden attributable to diseases of the skeletal system is a strong impetus for such advances.

Published online 8 August 2019

1. Sommerfeldt, D. W. & Rubin, C. T. Biology of bone and how it orchestrates the form and function of the skeleton. *Eur. Spine J.* **10** (Suppl. 2), S86–S95 (2001).
2. Clarke, B. Normal bone anatomy and physiology. *Clin. J. Am. Soc. Nephrol.* **3** (Suppl. 3), S131–S139 (2008).
3. Agas, D., Marchetti, L., Douni, E. & Sabbieti, M. G. The unbearable lightness of bone marrow homeostasis. *Cytokine Growth Factor Rev.* **26**, 347–359 (2015).
4. McKee, M. D. & Cole, W. G. (ed.) *Bone Matrix and Mineralization*. 2 edn (Elsevier, 2012).
5. Sims, N. A. & Martin, T. J. Coupling the activities of bone formation and resorption: a multitude of signals within the basic multicellular unit. *Bonekey Rep.* **3**, 481 (2014).
6. Bozec, A. & Zaiss, M. M. T. Regulatory cells in bone remodelling. *Curr. Osteoporos. Rep.* **15**, 121–125 (2017).
7. Parra-Torres, A. Y., Valdés-Flores, M., Orozco, L. & Velázquez-Cruz, R. In *Topics in Osteoporosis*. https://doi.org/10.5772/54905 (InTech Open, 2013).
8. Shetty, S., Kapoor, N., Bondu, J. D., Thomas, N. & Paul, T. V. Bone turnover markers: emerging tool in the management of osteoporosis. *Indian J. Endocrinol. Metab.* **20**, 846–852 (2016).
9. Hernlund, E. et al. Osteoporosis in the European Union: medical management, epidemiology and economic burden. *Arch. Osteoporos.* **8**, 136 (2013).
10. Suen, P. K. & Qin, L. Sclerostin, an emerging therapeutic target for treating osteoporosis and osteoporotic fracture: a general review. *J. Orthop. Translat.* **4**, 1–13 (2016).
11. Grüneboom, A. et al. A network of trans-cortical capillaries as mainstay for blood circulation in long bones. *Nat. Metab.* **1**, 236–250 (2019).
12. Andrews, J. C. et al. A high resolution, hard x-ray bio-imaging facility at SSRL. *Synchrotron Radiat. News* **21**, 17–26 (2008).
13. Arboleya, L. & Castañedab, S. Osteoimmunology: the study of the relationship between the immune system and bone tissue. *Reumatol. Clin.* **9**, 303–315 (2014).
14. Bach-Gansmo, F. L. et al. Osteocyte lacunar properties and cortical microstructure in human iliac crest as a function of age and sex. *Bone* **91**, 11–19 (2016).
15. Florencio-Silva, R., Sasso, G. R., Sasso-Cerri, E., Simoes, M. J. & Cerri, P. S. Biology of bone tissue: structure, function, and factors that influence bone cells. *Biomed. Res. Int.* **2015**, 421746 (2015).
16. Dallas, S. L. & Bonewald, L. F. Dynamics of the transition from osteoblast to osteocyte. *Ann. N. Y. Acad. Sci.* **1192**, 437–443 (2010).
17. Cardoso, L., Fritton, S. P., Gailani, G., Benalla, M. & Cowin, S. C. Advances in assessment of bone porosity, permeability and interstitial fluid flow. *J. Biomech.* **46**, 253–265 (2013).
18. Bonewald, L. F. & Johnson, M. L. Osteocytes, mechanosensing and Wnt signaling. *Bone* **42**, 606–615 (2008).
19. Röntgen, W. C. Ueber eine neue Art von Strahlen. Vorläufige Mitteilung. *Sitzungsberichte der Würzburger Physik.-medic. Gesellschaft*, 137–147 (1895).
20. Zhu, Y., Zhang, J., Li, A., Zhang, Y. & Fan, C. Synchrotron-based X-ray microscopy for sub-100nm resolution cell imaging. *Curr. Opin. Chem. Biol.* **39**, 11–16 (2017).
21. Varga, P. et al. Synchrotron X-ray phase nano-tomography-based analysis of the lacunar-canalicular network morphology and its relation to the strains experienced by osteocytes in situ as predicted by case-specific finite element analysis. *Biomech. Model Mechanobiol.* **14**, 267–282 (2015).
22. Sanderson, M. J., Smith, I., Parker, I. & Bootman, M. D. Fluorescence microscopy. *Cold Spring Harb. Protoc.* **2014**, https://doi.org/10.1101/pdb.top071795 (2014).
23. Wolf, D. E. Fundamentals of fluorescence and fluorescence microscopy. *Methods Cell Biol.* **81**, 63–91 (2007).
24. Engelke, K. et al. Clinical use of quantitative computed tomography and peripheral quantitative computed tomography in the management of osteoporosis in adults: The 2007 ISCD official positions. *J. Clin. Densitom.* **11**, 123–162 (2008).
25. Museyko, O., Bousson, V., Adams, J., Laredo, J. D. & Engelke, K. QCT of the proximal femur – which parameters should be measured to discriminate hip fracture? *Osteoporos. Int.* **27**, 1137–1147 (2016).
26. Wang, X. et al. Prediction of new clinical vertebral fractures in elderly men using finite element analysis of CT scans. *J. Bone Miner. Res.* **27**, 808–816 (2012).
27. Imai, K., Ohnishi, I., Matsumoto, T., Yamamoto, S. & Nakamura, K. Assessment of vertebral fracture risk and therapeutic effects of alendronate in postmenopausal women using a quantitative computed tomography-based nonlinear finite element method. *Osteoporos. Int.* **20**, 801–810 (2009).
28. Figueiredo, C. P. et al. Methods for segmentation of rheumatoid arthritis bone erosions in high-resolution peripheral quantitative computed tomography (HR-pQCT). *Semin. Arthritis Rheum.* **47**, 611–618 (2017).
29. Engelke, K. et al. Clinical use of quantitative computed tomography-based advanced techniques in the management of osteoporosis in adults: the 2015 ISCD official positions-part III. *J. Clin. Densitom.* **18**, 393–407 (2015).
30. Gausden, E. B., Nwachukwu, B. U., Schreiber, J. J., Lorich, D. G. & Lane, J. M. Opportunistic use of CT imaging for osteoporosis screening and bone density assessment: A qualitative systematic review. *J. Bone Joint Surg. Am.* **99**, 1580–1590 (2017).
31. Muhlberg, A. et al. Three-dimensional distribution of muscle and adipose tissue of the thigh at CT: association with acute hip fracture. *Radiology* **290**, 426–434 (2018).
32. Engelke, K. et al. Reanalysis precision of 3D quantitative computed tomography (QCT) of the spine. *Bone* **44**, 566–572 (2009).
33. Lang, T. F. et al. Volumetric quantitative computed tomography of the proximal femur: precision and relation to bone strength. *Bone* **21**, 101–108 (1997).
34. Gluer, C. C. 30 years of DXA technology innovations. *Bone* **104**, 7–12 (2017).
35. Engelke, K. et al. Quantitative computed tomography (QCT) of the forearm using general purpose spiral whole-body CT scanners: accuracy, precision and comparison with dual-energy X-ray absorptiometry (DXA). *Bone* **45**, 110–118 (2009).
36. Engelke, K. Quantitative computed tomography – current status and new developments. *J. Clin. Densitom.* **20**, 309–321 (2017).
37. Lin, E. & Alessio, A. What are the basic concepts of temporal, contrast, and spatial resolution in cardiac CT? *J. Cardiovasc. Comput. Tomogr.* **3**, 403–408 (2009).
38. Li, Y. et al. CT slice thickness and convolution kernel affect performance of a radiomic model for predicting EGFR status in non-small cell lung cancer: a preliminary study. *Sci. Rep.* **8**, 17913 (2018).
39. Dougherty, G. & Newman, D. Measurement of thickness and density of thin structures by computed tomography: a simulation study. *Med. Phys.* **26**, 1341–1348 (1999).
40. Newman, D. L., Dougherty, G., al Obaid, A. & al Hajrasy, H. Limitations of clinical CT in assessing cortical thickness and density. *Phys. Med. Biol.* **43**, 619–626 (1998).
41. Zebaze, R. M. et al. Intracortical remodelling and porosity in the distal radius and post-mortem femurs of women: a cross-sectional study. *Lancet* **375**, 1729–1736 (2010).
42. Museyko, O., Gerner, B. & Engelke, K. A new method to determine cortical bone thickness in CT images using a hybrid approach of parametric profile representation and local adaptive thresholds: accuracy results. *PLOS ONE* **12**, e0187097 (2017).
43. Treece, G. M. & Gee, A. H. Independent measurement of femoral cortical thickness and cortical bone density using clinical CT. *Med. Image Anal.* **20**, 249–264 (2015).
44. Treece, G. M., Poole, K. E. & Gee, A. H. Imaging the femoral cortex: thickness, density and mass from clinical CT. *Med. Image Anal.* **16**, 952–965 (2012).
45. Damm, T. et al. Improved accuracy in the assessment of vertebral cortical thickness by quantitative computed tomography using the Iterative Convolution OptimizatioN (ICON) method. *Bone* **120**, 194–203 (2018).
46. Zysset, P. et al. Clinical use of quantitative computed tomography-based finite element analysis of the hip and spine in the management of osteoporosis in adults: the 2015 ISCD official positions – part II. *J. Clin. Densitom.* **18**, 359–392 (2015).
47. Bousson, V. D. et al. In vivo discrimination of hip fracture with quantitative computed tomography: results from the prospective European Femur Fracture Study (EFFECT). *JBMR* **26**, 881–893 (2011).
48. Chappard, C. et al. Prediction of femoral fracture load: cross-sectional study of texture analysis and geometric measurements on plain radiographs versus bone mineral density. *Radiology* **255**, 536–543 (2010).
49. Cheng, X., Li, J., Lu, Y., Keyak, J. & Lang, T. Proximal femoral density and geometry measurements by quantitative computed tomography: association with hip fracture. *Bone* **40**, 169–174 (2007).
50. Yang, L. et al. Association of incident hip fracture with the estimated femoral strength by finite element analysis of DXA scans in the Osteoporotic Fractures in Men (MrOS) study. *Osteoporos. Int.* **29**, 643–651 (2017).
51. Yang, L., Udall, W. J., McCloskey, E. V. & Eastell, R. Distribution of bone density and cortical thickness in the proximal femur and their association with hip fracture in postmenopausal women: a quantitative computed tomography study. *Osteoporos. Int.* **25**, 251–263 (2014).
52. Borggrefe, J. et al. Association of 3D geometric measures derived from quantitative computed tomography with hip fracture risk in older men. *J. Bone Miner. Res.* **31**, 1550–1558 (2016).
53. Bouxsein, M. L. et al. Age- and sex-specific differences in the factor of risk for vertebral fracture: a population-based study using QCT. *J. Bone Miner. Res.* **21**, 1475–1482 (2006).
54. Bruno, A. G. et al. Vertebral size, bone density, and strength in men and women matched for age and areal spine BMD. *J. Bone Miner. Res.* **29**, 562–569 (2014).
55. Hahn, M. H. & Won, Y. Y. Bone mineral density and fatty degeneration of thigh muscles measured by computed tomography in hip fracture patients. *J. Bone. Metab.* **23**, 215–221 (2016).
56. Lang, T. et al. Computed tomographic measurements of thigh muscle cross-sectional area and attenuation coefficient predict hip fracture: the health, aging, and body composition study. *J. Bone Miner. Res.* **25**, 513–519 (2010).
57. Lang, T. et al. Pelvic body composition measurements by quantitative computed tomography: association with recent hip fracture. *Bone* **42**, 798–805 (2008).
58. Wong, A. K. et al. Bone-muscle indices as risk factors for fractures in men: the Osteoporotic Fractures in Men (MrOS) Study. *J. Musculoskelet. Neuronal Interact.* **14**, 246–254 (2014).
59. Lee, D. C., Hoffmann, P. F., Kopperdahl, D. L. & Keaveny, T. M. Phantomless calibration of CT scans for measurement of BMD and bone strength-Inter-operator reanalysis precision. *Bone* **103**, 325–333 (2017).
60. Boutroy, S., Bouxsein, M. L., Munoz, F. & Delmas, P. D. In vivo assessment of trabecular bone microarchitecture by high-resolution peripheral quantitative computed tomography. *J. Clin. Endocrinol. Metab.* **90**, 6508–6515 (2005).
61. Burghardt, A. J., Link, T. M. & Majumdar, S. High-resolution computed tomography for clinical imaging of bone microarchitecture. *Clin. Orthop. Relat. Res.* **469**, 2179–2193 (2011).

62. Nishiyama, K. K. & Shane, E. Clinical imaging of bone microarchitecture with HR-pQCT. *Curr. Osteoporos. Rep.* **11**, 147–155 (2013).
63. Burghardt, A. J. et al. Multicenter precision of cortical and trabecular bone quality measures assessed by high-resolution peripheral quantitative computed tomography. *J. Bone Miner. Res.* **28**, 524–536 (2013).
64. Manske, S. L., Davison, E. M., Burt, L. A., Raymond, D. A. & Boyd, S. K. The estimation of second-generation HR-pQCT from first-generation HR-pQCT using in vivo cross-calibration. *J. Bone Miner. Res.* **32**, 1514–1524 (2017).
65. Laib, A. & Ruegsegger, P. Calibration of trabecular bone structure measurements of in vivo three-dimensional peripheral quantitative computed tomography with 28-microm-resolution microcomputed tomography. *Bone* **24**, 35–39 (1999).
66. Manske, S. L., Zhu, Y., Sandino, C. & Boyd, S. K. Human trabecular bone microarchitecture can be assessed independently of density with second generation HR-pQCT. *Bone* **79**, 213–221 (2015).
67. Tjong, W., Nirody, J., Burghardt, A. J., Carballido-Gamio, J. & Kazakia, G. J. Structural analysis of cortical porosity applied to HR-pQCT data. *Med. Phys.* **41**, 013701 (2014).
68. Bousson, V. et al. Distribution of intracortical porosity in human midfemoral cortex by age and gender. *J. Bone Miner. Res.* **16**, 1308–1317 (2001).
69. Paccou, J. et al. Bone microarchitecture in men and women with diabetes: the importance of cortical porosity. *Calcif. Tissue Int.* **98**, 465–473 (2016).
70. Patsch, J. M. et al. Increased cortical porosity in type 2 diabetic postmenopausal women with fragility fractures. *J. Bone Miner. Res.* **28**, 313–324 (2013).
71. Cheung, A. M. et al. High-resolution peripheral quantitative computed tomography for the assessment of bone strength and structure: a review by the Canadian Bone Strength Working Group. *Curr. Osteoporos. Rep.* **11**, 136–146 (2013).
72. Nishiyama, K., Dal'Ara, E. & Engelke, K. In *Advanced Techniques of Bone Mass Measurements in Adults* (Bilezikian, J. P., ed.) (Wiley, 2018).
73. Schett, G. & Gravallese, E. Bone erosion in rheumatoid arthritis: mechanisms, diagnosis and treatment. *Nat. Rev. Rheumatol.* **8**, 656–664 (2012).
74. Regensburger, A. et al. A comparative analysis of magnetic resonance imaging and high-resolution peripheral quantitative computed tomography of the hand for the detection of erosion repair in rheumatoid arthritis. *Rheumatology* **54**, 1573–1581 (2015).
75. Bhatnagar, S., Krishnamurthy, V. & Pagare, S. S. Diagnostic efficacy of panoramic radiography in detection of osteoporosis in post-menopausal women with low bone mineral density. *J. Clin. Imaging Sci.* **3**, 23 (2013).
76. de Charry, C. et al. Clinical cone beam computed tomography compared to high-resolution peripheral computed tomography in the assessment of distal radius bone. *Osteoporos. Int.* **27**, 3073–3082 (2016).
77. Posadzy, M., Desimpel, J. & Vanhoenacker, F. Cone beam CT of the musculoskeletal system: clinical applications. *Insights Imaging* **9**, 35–45 (2018).
78. Nardi, C. et al. The role of cone beam CT in the study of symptomatic total knee arthroplasty (TKA): a 20 cases report. *Br. J. Radiol.* **90**, 20160925 (2017).
79. Mys, K., Stockmans, F., Vereecke, E. & van Lenthe, G. H. Quantification of bone microstructure in the wrist using cone-beam computed tomography. *Bone* **114**, 206–214 (2018).
80. Paulus, M. J., Gleason, S. S., Kennel, S. J., Hunsicker, P. R. & Johnson, D. K. High resolution X-ray computed tomography: an emerging tool for small animal cancer research. *Neoplasia* **2**, 62–70 (2000).
81. Schneider, P., Meier, M., Wepf, R. & Müller, R. Serial FIB/SEM imaging for quantitative 3D assessment of the osteocyte lacuno-canalicular network. *Bone* **49**, 304–311 (2011).
82. Langer, M. et al. X-Ray phase nanotomography resolves the 3D human bone ultrastructure. *PLOS ONE* **7**, e35691 (2012).
83. Hasegawa, T. et al. Three-dimensional ultrastructure of osteocytes assessed by focused ion beam-scanning electron microscopy (FIB-SEM). *Histochem. Cell Biol.* **149**, 423–432 (2018).
84. Carl Zeiss Microscopy GmbH. Multi-length Scale Imaging Bridging the 3D Resolution Gap. *Zeiss.de* https://www.zeiss.de/content/dam/Microscopy/us/download/pdf/technical-notes/x-ray-microscopy/multi-length-scale-imaging.pdf (2013).
85. Bonse, U. (ed.) *Developments in X-ray Tomography III*. Vol. 4503, 1–386 (SPIE Press, 2002).
86. Langer, M. & Peyrin, F. 3D X-ray ultra-microscopy of bone tissue. *Osteoporos. Int.* **27**, 441–455 (2016).
87. Muller, R. Hierarchical microimaging of bone structure and function. *Nat. Rev. Rheumatol.* **5**, 373–381 (2009).
88. Schneider, P. et al. Simultaneous 3D visualization and quantification of murine bone and bone vasculature using micro-computed tomography and vascular replica. *Microsc. Res. Tech.* **72**, 690–701 (2009).
89. Schropp, A. et al. Hard x-ray scanning microscopy with coherent radiation: beyond the resolution of conventional x-ray microscopes. *Appl. Phys. Lett.* **100**, 253112–253112 (2012).
90. Ma, S. et al. Synchrotron imaging assessment of bone quality. *Clin. Rev. Bone Miner. Metab.* **14**, 150–160 (2016).
91. Paul, G. R., Malhotra, A. & Muller, R. Mechanical stimuli in the local in vivo environment in bone: computational approaches linking organ-scale loads to cellular signals. *Curr. Osteoporos. Rep.* **16**, 395–403 (2018).
92. Zizak, I. et al. Characteristics of mineral particles in the human bone/cartilage interface. *J. Struct. Biol.* **141**, 208–217 (2003).
93. Gupta, H. S. et al. Nanoscale deformation mechanisms in bone. *Nano Lett.* **5**, 2108–2111 (2005).
94. Hammond, M. A., Gallant, M. A., Burr, D. B. & Wallace, J. M. Nanoscale changes in collagen are reflected in physical and mechanical properties of bone at the microscale in diabetic rats. *Bone* **60**, 26–32 (2013).
95. Gelb, J. Functionality to failure: materials engineering in the 4th dimension. *Adv. Mater. Process.* **170**, 14–18 (2012).
96. Tkachuk, A. et al. X-ray computed tomography in Zernike phase contrast mode at 8 keV with 50-nm resolution using Cu rotating anode X-ray source. *Z. Kristallogr.* **222**, 650–655 (2007).
97. Gelb, J. *et al*. Non-destructive local X-ray tomography for multi-length scale analysis of reservoir rocks: validations and observations. in *Int. Symposium of the Society of Core Analysts*. 1–6 (2012).
98. Wang, J. et al. Automated markerless full field hard x-ray microscopic tomography at sub-50 nm 3-dimension spatial resolution. *Appl. Phys. Lett.* **100**, 143107 (2012).
99. Tian, Y. et al. High resolution hard x-ray microscope on a second generation synchrotron source. *Rev. Sci. Instrum.* **79**, 103708/103701 (2008).
100. Chu, Y. S. et al. Hard-x-ray microscopy with Fresnel zone plates reaches 40 nm Rayleigh resolution. *Appl. Phys. Lett.* **92**, 103119 (2008).
101. Ladd, M. E. et al. Pros and cons of ultra-high-field MRI/MRS for human application. *Progr. Nucl. Magn. Reson. Spectrosc.* **109**, 1–50 (2018).
102. van Wijk, D. F. et al. Increasing spatial resolution of 3T MRI scanning improves reproducibility of carotid arterial wall dimension measurements. *MAGMA* **27**, 219–226 (2014).
103. Nowogrodzki, A. The world's strongest MRI machines are pushing human imaging to new limits. *Nature* **563**, 24–26 (2018).
104. Kraff, O. & Quick, H. H. 7T: Physics, safety, and potential clinical applications. *J. Magn. Reson. Imaging* **46**, 1573–1589 (2017).
105. Krug, R., Stehling, C., Kelley, D. A. C., Majumdar, S. & Link, T. M. Imaging of the musculoskeletal system in vivo using ultra-high field magnetic resonance at 7 T. *Invest. Radiol.* **44**, 613–618 (2009).
106. Chang, G. et al. MRI of the hip at 7T: feasibility of bone microarchitecture, high-resolution cartilage, and clinical imaging. *J. Magn. Reson. Imaging* **39**, 1384–1393 (2014).
107. Chang, G. et al. 7T MRI detects deterioration in subchondral bone microarchitecture in subjects with mild knee osteoarthritis as compared with healthy controls. *J. Magn. Reson. Imaging* **41**, 1311–1317 (2015).
108. Lazik, A. et al. 7 Tesla quantitative hip MRI: T1, T2 and T2* mapping of hip cartilage in healthy volunteers. *Eur. Radiol.* **26**, 1245–1253 (2015).
109. Lazik-Palm, A. et al. Morphological and quantitative 7 T MRI of hip cartilage transplants in comparison to 3 T – initial experiences. *Invest. Radiol.* **51**, 552–559 (2016).
110. Juras, V. et al. The compositional difference between ankle and knee cartilage demonstrated by T2 mapping at 7 Tesla MR. *Eur. J. Radiol.* **85**, 771–777 (2016).
111. Krug, R. et al. In vivo ultra-high-field magnetic resonance imaging of trabecular bone microarchitecture at 7 T. *J. Magn. Reson. Imaging* **27**, 854–859 (2008).
112. Wright, A. C. et al. Helmholtz-pair transmit coil with integrated receive array for high-resolution MRI of trabecular bone in the distal tibia at 7T. *J. Magn. Reson.* **210**, 113–122 (2011).
113. Griffin, L. M. et al. 7T MRI of distal radius trabecular bone microarchitecture: how trabecular bone quality varies depending on distance from end-of-bone. *J. Magn. Reson. Imaging* **45**, 872–878 (2016).
114. Bhagat, Y. A. et al. Performance of μMRI-based virtual bone biopsy for structural and mechanical analysis at the distal tibia at 7T field strength. *J. Magn. Reson. Imaging* **33**, 372–381 (2011).
115. Chang, G. et al. In vivo estimation of bone stiffness at the distal femur and proximal tibia using ultra-high-field 7-Tesla magnetic resonance imaging and micro-finite element analysis. *J. Bone Miner. Metab.* **30**, 243–251 (2011).
116. Weiger, M., Stampanoni, M. & Pruessmann, K. P. Direct depiction of bone microstructure using MRI with zero echo time. *Bone* **54**, 44–47 (2013).
117. Wehrli, F. W. & Fernandez-Seara, M. A. Nuclear magnetic resonance studies of bone water. *Ann. Biomed. Eng.* **33**, 79–86 (2005).
118. Jara, H., Wehrli, F. W., Chung, H. & Ford, J. C. High-resolution variable flip angle 3D MR imaging of trabecular microstructure in vivo. *Magn. Reson. Med.* **29**, 528–539 (1993).
119. Liu, X. S. et al. Accuracy of high-resolution in vivo micro magnetic resonance imaging for measurements of microstructural and mechanical properties of human distal tibial bone. *J. Bone Miner. Res.* **25**, 2039–2050 (2010).
120. Anumula, S., Wehrli, S. L., Magland, J., Wright, A. C. & Wehrli, F. W. Ultra-short echo-time MRI detects changes in bone mineralization and water content in OVX rat bone in response to alendronate treatment. *Bone* **46**, 1391–1399 (2010).
121. Krug, R. et al. Ultrashort echo time MRI of cortical bone at 7 Tesla field strength: a feasibility study. *J. Magn. Reson. Imaging* **34**, 691–695 (2011).
122. Lazik-Palm, A. et al. Morphological imaging and T2 and T2* mapping of hip cartilage at 7 Tesla MRI under the influence of intravenous gadolinium. *Eur. Radiol.* **26**, 3923–3931 (2016).
123. Rietsch, S. H. G. et al. An 8-channel transceiver 7-channel receive RF coil setup for high SNR ultrahigh-field MRI of the shoulder at 7T. *Med. Phys.* **44**, 6195–6208 (2017).
124. Johst, S., Wrede, K. H., Ladd, M. E. & Maderwald, S. Time-of-flight magnetic resonance angiography at 7 T using venous saturation pulses with reduced flip angles. *Invest. Radiol.* **47**, 445–450 (2012).
125. Mattern, H. et al. Prospective motion correction enables highest resolution time-of-flight angiography at 7T. *Magn. Reson. Med.* **80**, 248–258 (2017).
126. Fu, R. et al. Ultra-wide bore 900MHz high-resolution NMR at the national high magnetic field laboratory. *J. Magn. Reson.* **177**, 1–8 (2005).
127. Schepkin, V. D., Brey, W. W., Gor'kov, P. L. & Grant, S. C. Initial in vivo rodent sodium and proton MR imaging at 21.1 T. *Magn. Reson. Imaging* **28**, 400–407 (2010).
128. Budinger, T. F. & Bird, M. D. MRI and MRS of the human brain at magnetic fields of 14 T to 20 T: technical feasibility, safety, and neuroscience horizons. *NeuroImage* **168**, 509–531 (2018).
129. Budinger, T. F. et al. Toward 20 T magnetic resonance for human brain studies: opportunities for discovery and neuroscience rationale. *Magn. Reson. Mater. Phys. Biol. Med.* **29**, 617–639 (2016).
130. Schulz, R. B. & Semmler, W. Fundamentals of optical imaging *Handb. Exp. Pharmacol.* **185**, 3–22 (2008).
131. Hell, S. W. Far-field optical nanoscopy. *Science* **316**, 1153–1158 (2007).
132. Sigal, Y. M., Zhou, R. & Zhuang, X. Visualizing and discovering cellular structures with super-resolution microscopy. *Science* **361**, 880–887 (2018).
133. Adams, M. W., Loftus, A. F., Dunn, S. E., Joens, M. S. & Fitzpatrick, J. A. Light sheet fluorescence microscopy (LSFM). *Curr. Protoc. Cytom.* **71**, 12 37 11–12 37 15 (2015).
134. Santi, P. A. Light sheet fluorescence microscopy: a review. *J. Histochem. Cytochem.* **59**, 129–138 (2011).
135. Keller, P. J. & Stelzer, E. H. Quantitative in vivo imaging of entire embryos with digital scanned laser light sheet fluorescence microscopy. *Curr. Opin. Neurobiol.* **18**, 624–632 (2008).
136. Richardson, D. S. & Lichtman, J. W. Clarifying tissue clearing. *Cell* **162**, 246–257 (2015).

137. Klingberg, A. et al. Fully automated evaluation of total glomerular number and capillary tuft size in nephritic kidneys using lightsheet microscopy. *J. Am. Soc. Nephrol.* **28**, 452–459 (2017).
138. Chatterjee, K., Pratiwi, F. W., Wu, F. C. M., Chen, P. & Chen, B. C. Recent progress in light sheet microscopy for biological applications. *Appl. Spectrosc.* **72**, 1137–1169 (2018).
139. Keller, P. J., Schmidt, A. D., Wittbrodt, J. & Stelzer, E. H. Digital scanned laser light-sheet fluorescence microscopy (DSLM) of zebrafish and *Drosophila* embryonic development. *Cold Spring Harb. Protoc.* **2011**, 1235–1243 (2011).
140. Kromm, D., Thumberger, T. & Wittbrodt, J. An eye on light-sheet microscopy. *Methods Cell Biol.* **133**, 105–123 (2016).
141. Dean, K. M. & Fiolka, R. Uniform and scalable light-sheets generated by extended focusing. *Opt. Express* **22**, 26141–26152 (2014).
142. Dean, K. M., Roudot, P., Welf, E. S., Danuser, G. & Fiolka, R. Deconvolution-free subcellular imaging with axially swept light sheet microscopy. *Biophys. J.* **108**, 2807–2815 (2015).
143. Genina, E. A., Bashkatov, A. N. & Tuchin, V. V. Optical clearing of cranial bone. *Adv. Opt. Technol.* **2008**, 1–8 (2008).
144. Vigouroux, R. J., Belle, M. & Chedotal, A. Neuroscience in the third dimension: shedding new light on the brain with tissue clearing. *Mol. Brain* **10**, 33 (2017).
145. Zundler, S. et al. Three-dimensional cross-sectional light-sheet microscopy imaging of the inflamed mouse gut. *Gastroenterology* **153**, 898–900 (2017).
146. Männ, L. et al. CD11c.DTR mice develop a fatal fulminant myocarditis after local or systemic treatment with diphtheria toxin. *Eur. J. Immunol.* **46**, 2028–2042 (2016).
147. Tuchin, V. V. Optical clearing of tissues and blood using the immersion method. *J. Phys. D: Appl. Phys.* **38**, 2497–2518 (2005).
148. Ariel, P. A beginner's guide to tissue clearing. *Int. J. Biochem. Cell Biol.* **84**, 35–39 (2017).
149. Renier, N. et al. iDISCO: a simple, rapid method to immunolabel large tissue samples for volume imaging. *Cell* **159**, 896–910 (2014).
150. Becker, K., Jahrling, N., Saghafi, S., Weiler, R. & Dodt, H. U. Chemical clearing and dehydration of GFP expressing mouse brains. *PLOS ONE* **7**, e33916 (2012).
151. Becker, K., Jahrling, N., Kramer, E. R., Schnorrer, F. & Dodt, H. U. Ultramicroscopy: 3D reconstruction of large microscopical specimens. *J. Biophotonics* **1**, 36–42 (2008).
152. Schwarz, M. K. et al. Fluorescent-protein stabilization and high-resolution imaging of cleared, intact mouse brains. *PLOS ONE* **10**, e0124650 (2015).
153. Zukor, K. A., Kent, D. T. & Odelberg, S. J. Fluorescent whole-mount method for visualizing three-dimensional relationships in intact and regenerating adult newt spinal cords. *Dev. Dyn.* **239**, 3048–3057 (2010).
154. Acar, M. et al. Deep imaging of bone marrow shows non-dividing stem cells are mainly perisinusoidal. *Nature* **526**, 126–130 (2015).
155. Chen, J. Y. et al. Hoxb5 marks long-term haematopoietic stem cells and reveals a homogenous perivascular niche. *Nature* **530**, 223–227 (2016).
156. de Saint-Georges, L. & Miller, S. C. The microcirculation of bone and marrow in the diaphysis of the rat hemopoietic long bones. *Anat. Rec.* **233**, 169–177 (1992).
157. Herisson, F. et al. Direct vascular channels connect skull bone marrow and the brain surface enabling myeloid cell migration. *Nat. Neurosci.* **21**, 1209–1217 (2018).
158. Augustin, H. G. & Koh, G. Y. Organotypic vasculature: from descriptive heterogeneity to functional pathophysiology. *Science* **357**, eaal2379 (2017).
159. Ramasamy, S. K. et al. Blood flow controls bone vascular function and osteogenesis. *Nat. Commun.* **7**, 13601 (2016).
160. Ramasamy, S. K. Structure and functions of blood vessels and vascular niches in bone. *Stem Cells Int.* **2017**, 5046953 (2017).
161. Jonkman, J. & Brown, C. M. Any way you slice it – a comparison of confocal microscopy techniques. *J. Biomol. Tech.* **26**, 54–65 (2015).
162. Takaku, T. et al. Hematopoiesis in 3 dimensions: human and murine bone marrow architecture visualized by confocal microscopy. *Blood* **116**, e41–e55 (2010).
163. Morrison, S. J. & Scadden, D. T. The bone marrow niche for haematopoietic stem cells. *Nature* **505**, 327–334 (2014).
164. Kusumbe, A. P., Ramasamy, S. K. & Adams, R. H. Coupling of angiogenesis and osteogenesis by a specific vessel subtype in bone. *Nature* **507**, 323–328 (2014).
165. Ramasamy, S. K., Kusumbe, A. P., Wang, L. & Adams, R. H. Endothelial Notch activity promotes angiogenesis and osteogenesis in bone. *Nature* **507**, 376–380 (2014).
166. Kunisaki, Y. et al. Arteriolar niches maintain haematopoietic stem cell quiescence. *Nature* **502**, 637–643 (2013).
167. Mizuhashi, K. et al. Resting zone of the growth plate houses a unique class of skeletal stem cells. *Nature* **563**, 254–258 (2018).
168. Cahalan, M. D., Parker, I., Wei, S. H. & Miller, M. J. Two-photon tissue imaging: seeing the immune system in a fresh light. *Nat. Rev. Immunol.* **2**, 872–880 (2002).
169. Erturk, A. et al. Three-dimensional imaging of solvent-cleared organs using 3DISCO. *Nat. Protoc.* **7**, 1983–1995 (2012).
170. Tanaka, K. et al. Intravital imaging of gastrointestinal diseases in preclinical models using two-photon laser scanning microscopy. *Surg. Today* **43**, 123–129 (2013).
171. Phan, T. G. & Bullen, A. Practical intravital two-photon microscopy for immunological research: faster, brighter, deeper. *Immunol. Cell Biol.* **88**, 438–444 (2010).
172. Perry, S. W., Burke, R. M. & Brown, E. B. Two-photon and second harmonic microscopy in clinical and translational cancer research. *Ann. Biomed. Eng.* **40**, 277–291 (2012).
173. Bousso, P. & Moreau, H. D. Functional immunoimaging: the revolution continues. *Nat. Rev. Immunol.* **12**, 858–864 (2012).
174. Germain, R. N., Robey, E. A. & Cahalan, M. D. A decade of imaging cellular motility and interaction dynamics in the immune system. *Science* **336**, 1676–1681 (2012).
175. Niesner, R. A., Andresen, V. & Gunzer, M. Intravital 2-photon microscopy – focus on speed and time resolved imaging modalities. *Immunol. Rev.* **221**, 7–25 (2008).
176. Wang, T. et al. Three-photon imaging of mouse brain structure and function through the intact skull. *Nat. Methods* **15**, 789–792 (2018).
177. Carriles, R. et al. Invited review article: imaging techniques for harmonic and multiphoton absorption fluorescence microscopy. *Rev. Sci. Instrum.* **80**, 081101 (2009).
178. Vielreicher, M. et al. Taking a deep look: modern microscopy technologies to optimize the design and functionality of biocompatible scaffolds for tissue engineering in regenerative medicine. *J. R. Soc. Interface* **10**, 20130263 (2013).
179. Georgiadis, M., Muller, R. & Schneider, P. Techniques to assess bone ultrastructure organization: orientation and arrangement of mineralized collagen fibrils. *J. R. Soc. Interface* **13**, 20160088 (2016).
180. Genthial, R. et al. Label-free imaging of bone multiscale porosity and interfaces using third-harmonic generation microscopy. *Sci. Rep.* **7**, 3419 (2017).
181. Saitou, T., Kiyomatsu, H. & Imamura, T. Quantitative morphometry for osteochondral tissues using second harmonic generation microscopy and image texture information. *Sci. Rep.* **8**, 2826 (2018).
182. Okada, T., Takahashi, S., Ishida, A. & Ishigame, H. In vivo multiphoton imaging of immune cell dynamics. *Pflugers Arch.* **468**, 1793–1801 (2016).
183. Mazo, I. B. et al. Hematopoietic progenitor cell rolling in bone marrow microvessels: parallel contributions by endothelial selectins and vascular cell adhesion molecule 1. *J. Exp. Med.* **188**, 465–474 (1998).
184. Vandoorne, K. et al. Imaging the vascular bone marrow niche during inflammatory stress. *Circ. Res.* **123**, 415–427 (2018).
185. Bixel, M. G. et al. Flow dynamics and HSPC homing in bone marrow microvessels. *Cell. Rep.* **18**, 1804–1816 (2017).
186. Hasenberg, A. et al. Catchup: a mouse model for imaging-based tracking and modulation of neutrophil granulocytes. *Nat. Methods* **12**, 445–452 (2015).
187. Spencer, J. A. et al. Direct measurement of local oxygen concentration in the bone marrow of live animals. *Nature* **508**, 269–273 (2014).
188. Köhler, A. et al. G-CSF mediated thrombopoietin release triggers neutrophil motility and mobilization from bone marrow via induction of Cxcr2 ligands. *Blood* **117**, 4349–4357 (2011).
189. Junt, T. et al. Dynamic visualization of thrombopoiesis within bone marrow. *Science* **317**, 1767–1770 (2007).
190. Massberg, S. et al. Immunosurveillance by hematopoietic progenitor cells trafficking through blood, lymph, and peripheral tissues. *Cell* **131**, 994–1008 (2007).
191. Devi, S. et al. Neutrophil mobilization via plerixafor-mediated CXCR4 inhibition arises from lung demargination and blockade of neutrophil homing to the bone marrow. *J. Exp. Med.* **210**, 2321–2336 (2013).
192. Lassailly, F., Foster, K., Lopez-Onieva, L., Currie, E. & Bonnet, D. Multimodal imaging reveals structural and functional heterogeneity in different bone marrow compartments: functional implications on hematopoietic stem cells. *Blood* **122**, 1730–1740 (2013).
193. Köhler, A. et al. Altered cellular dynamics and endosteal location of aged early hematopoietic progenitor cells revealed by time-lapse intravital imaging in long bones. *Blood* **114**, 290–298 (2009).
194. Kiel, M. J., Iwashita, T., Yilmaz, O. H. & Morrison, S. J. Spatial differences in hematopoiesis but not in stem cells indicate a lack of regional patterning in definitive hematopoietic stem cells. *Dev. Biol.* **283**, 29–39 (2005).
195. Chan, C. K. et al. Endochondral ossification is required for haematopoietic stem-cell niche formation. *Nature* **457**, 490–494 (2009).
196. Nombela-Arrieta, C. & Manz, M. G. Quantification and three-dimensional microanatomical organization of the bone marrow. *Blood Adv.* **1**, 407–416 (2017).
197. Otto, L., Zelinskyy, G., Schuster, M., Dittmer, U. & Gunzer, M. Imaging of cytotoxic antiviral immunity while considering the 3R principle of animal research. *J. Mol. Med.* **96**, 349–360 (2018).
198. Mill, L. et al. In *Bildverarbeitung für die Medizin 2018*. Springer, 115–120 (2018).
199. Aichert, A. et al. Epipolar consistency in transmission imaging. *IEEE Trans Med Imaging* **34**, 2205–2219 (2015).
200. Bier, B. *et al*. X-ray-transform invariant anatomical landmark detection for pelvic trauma surgery. *arXiv e-prints* https://arxiv.org/abs/1803.08608 (2018).
201. Choi, J. H. et al. Fiducial marker-based correction for involuntary motion in weight-bearing C-arm CT scanning of knees. II. Experiment. *Med. Phys.* **41**, 061902 (2014).
202. Pan, X., Sidky, E. Y. & Vannier, M. Why do commercial CT scanners still employ traditional, filtered back-projection for image reconstruction? *Inverse Probl.* **25**, 1230009 (2009).
203. Würfl, T., Ghesu, F. C., Christlein, V. & Maier, A. in *Medical Image Computing and Computer-Assisted Intervention – MICCAI 2016*. 432–440 (2016).
204. Zhu, B., Liu, J. Z., Cauley, S. F., Rosen, B. R. & Rosen, M. S. Image reconstruction by domain-transform manifold learning. *Nature* **555**, 487–492 (2018).
205. Ye, J. C., Han, Y. & Cha, E. Deep convolutional framelets: a general deep learning framework for inverse problems. *arXiv e-prints* https://arxiv.org/abs/1707.00372 (2017).
206. Kobler, E., Klatzer, T., Hammernik, K. & Pock, T. Variational networks: connecting variational methods and deep learning, in *German Conference on Pattern Recognition*. Springer, 281–293 (2017).
207. Halabi, S. S. et al. The RSNA pediatric bone age machine learning challenge. *Radiology* **290**, 498–503 (2018).
208. Ellmann, S. et al. Prediction of early metastatic disease in experimental breast cancer bone metastasis by combining PET/CT and MRI parameters to a model-averaged neural network. *Bone* **120**, 254–261 (2018).
209. Yune, S. *et al*. Beyond human perception: sexual dimorphism in hand and wrist radiographs is discernible by a deep learning model. *J. Digit. Imaging* https://doi.org/10.1007/s10278-018-0148-x (2018).
210. Maier, A., Syben, C., Lasser, T. & Riess, C. A gentle introduction to deep learning in medical image processing. *Zeitschrift für Medizinische Physik* **29**, 86–101 (2018).
211. Maier, A. *et al*. Precision learning: towards use of known operators in neural networks. *arXiv e-prints* https://arxiv.org/abs/1712.00374 (2017).
212. Andrews, J. C. et al. Nanoscale X-ray microscopic imaging of mammalian mineralized tissue. *Microsc. Microanal.* **16**, 327–336 (2010).

213. Stelzer, E. H. Light-sheet fluorescence microscopy for quantitative biology. *Nat. Methods* **12**, 23–26 (2014).
214. Pan, C. et al. Shrinkage-mediated imaging of entire organs and organisms using uDISCO. *Nat. Methods* **13**, 859–867 (2016).
215. Moser, E., Stadlbauer, A., Windischberger, C., Quick, H. H. & Ladd, M. E. Magnetic resonance imaging methodology. *Eur. J. Nucl. Med. Mol. Imaging* **36** (Suppl. 1), S30–S41 (2009).

Acknowledgements
The authors thank the IMaging Centre ESsen, the Optical Imaging Centre Erlangen and the Erwin L. Hahn Institute for Magnetic Resonance Imaging at University Duisburg-Essen for support with imaging. The authors' work is supported by funding from the German Research Foundation (SPP1480 Immunobone), to M.G. and G.S.; the Collaborative Research Centre (CRC) 1181, to G.S.; and the European Union (EU HEALTH-2013-INNOVATION-1, MATHIAS), to M.G.. The work of S.K., A.M. and G.S. is also supported by the European Research Council (ERC) Synergy grant NanoScope (grant no. 810316) and the work of G.S. is also supported by the Innovative Medicine Initiative (IMI)-funded project RTCure.

Author contributions
All authors contributed equally to all aspects of the manuscript, including researching data for the article, providing substantial contributions to discussions of its content, writing the article, and reviewing and/or editing of the manuscript before submission.

Competing interests
The authors declare no competing interests.

Publisher's note

Supplementary information
Supplementary information is available for this paper at https://doi.org/10.1038/s41584-019-0274-y.

Surgical and tissue engineering strategies for articular cartilage and meniscus repair

*Heenam Kwon[1], Wendy E. Brown[1], Cassandra A. Lee[2], Dean Wang[3], Nikolaos Paschos[4], Jerry C. Hu[1] and Kyriacos A. Athanasiou[1]**

Abstract | Injuries to articular cartilage and menisci can lead to cartilage degeneration that ultimately results in arthritis. Different forms of arthritis affect ~50 million people in the USA alone, and it is therefore crucial to identify methods that will halt or slow the progression to arthritis, starting with the initiating events of cartilage and meniscus defects. The surgical approaches in current use have a limited capacity for tissue regeneration and yield only short-term relief of symptoms. Tissue engineering approaches are emerging as alternatives to current surgical methods for cartilage and meniscus repair. Several cell-based and tissue-engineered products are currently in clinical trials for cartilage lesions and meniscal tears, opening new avenues for cartilage and meniscus regeneration. This Review provides a summary of surgical techniques, including tissue-engineered products, that are currently in clinical use, as well as a discussion of state-of-the-art tissue engineering strategies and technologies that are being developed for use in articular cartilage and meniscus repair and regeneration. The obstacles to clinical translation of these strategies are also included to inform the development of innovative tissue engineering approaches.

[1]*Department of Biomedical Engineering, University of California Irvine, Irvine, CA, USA.*

[2]*Department of Orthopaedic Surgery, University of California Davis Medical Center, Sacramento, CA, USA.*

[3]*Department of Orthopaedic Surgery, University of California Irvine Medical Center, Orange, CA, USA.*

[4]*Division of Sports Medicine, Department of Orthopaedic Surgery, New England Baptist Hospital, Tufts University School of Medicine, Boston, MA, USA.*

**e-mail: athens@uci.edu*

https://doi.org/10.1038/s41584-019-0255-1

Arthritis is a debilitating condition that affects ~50 million adults in the USA, a prevalence that is projected to rise by ~60% in the next two decades[1]. Osteoarthritis (OA), the most common type of arthritis[2], is associated with pain and loss of joint function. Although the aetiology of OA can be idiopathic, the disease is often characterized by cartilage degeneration in articulating joints as a result of 'wear and tear' or injury, including sports-related injuries. For example, in one study, individuals who sustained knee injuries were 7.4 times more likely to develop OA than those who had not sustained knee injuries[3]. Meniscus and anterior cruciate ligament (ACL) tears can also contribute to the development of OA because damage to these structures alters joint loading[4,5]; OA occurs 10–20 years after injury in ~50% of patients who sustain meniscal or ACL tears[5]. Globally, knee and hip cartilage degeneration is one of the leading contributors to disability[6]. Rheumatoid arthritis (RA), the second most common type of arthritis, is a chronic autoimmune disease characterized by inflammation and deterioration of joints that results in loss of function, and affects 1.3 million adults in the USA[7]. Worldwide, arthritides such as OA and RA represent a substantial burden to health-care systems[8,9].

Despite the pervasiveness of OA, most current treatments are palliative and do not prevent further joint degeneration[10]. Likewise, treatments for RA often reduce joint inflammation without treating cartilage damage[11]. Ultimately, many patients with arthritis will require total joint arthroplasty, an invasive end-stage treatment that uses implants that wear out over time. Current surgical strategies for cartilage repair are designed to treat small defects in cartilage and are not directly indicated for use in inflamed joints, such as those that occur in RA. However, using tissue engineering strategies, which focus on the complete regeneration of articular cartilage[12,13] and menisci[14,15], researchers can potentially create neotissue that has been modified to withstand immune-mediated degeneration. Thus, in the future, tissue engineering strategies could offer new therapeutic avenues for patients with RA before total joint arthroplasty is indicated.

In this Review, we begin by discussing current surgical techniques, including tissue-engineered treatments, defined here as cell-based (scaffold-free and scaffold-based) therapies, for the repair of articular cartilage and meniscus lesions. We then discuss advances in tissue engineering research for articular cartilage and meniscus regeneration, including novel scaffold-based and scaffold-free approaches, promising sources of cells for cell-based therapies and emerging data on biochemical and biomechanical stimuli. We also present data

Key points

- Current cartilage repair techniques include surgery and cell-based therapies for articular cartilage, and surgery for meniscus repair; however, such treatments have limited capacity to induce regeneration.
- Tissue engineering strategies to create cartilage using a variety of cell sources and exogenous stimuli have made advances towards replicating the native architecture and functional properties of cartilage.
- Most cell-based tissue engineering products currently in clinical trials are indicated for knee articular cartilage, with very few indicated for hip cartilage or the meniscus.
- Allogeneic and non-articulating cartilage might serve as additional cell sources for engineered articular cartilage and meniscus products.
- The pro-inflammatory environment of arthritic joints and issues surrounding neotissue integration need to be addressed to maximize the clinical translation of new tissue-engineered products.

on cell-based tissue-engineered products for cartilage regeneration currently in development. Finally, we discuss scientific and regulatory obstacles to the clinical translation of tissue-engineered technologies, as well as future directions to encourage researchers in the field to overcome these challenges.

Current surgical strategies

Repairing articular cartilage defects

Articular cartilage is predominantly composed of type II collagen and glycosaminoglycans and is avascular with low cellularity (FIG. 1a) and, therefore, has a low healing capacity. Clinicians encounter articular cartilage damage in more than half of knee arthroscopies performed as a result of injury or symptoms of cartilage damage[16,17]. Specifically, chondral lesions (defects that do not penetrate into the subchondral bone) and osteochondral lesions (defects that penetrate into the subchondral bone) were found in 61% of patients surveyed[12,17]. Because cartilage defects are often asymptomatic[18], careful assessment is required to determine whether the lesion is the source of pain in an individual. Current surgical strategies aim to repair small (<4 cm^2) defects in cartilage to prevent further degeneration and progression towards OA (FIG. 1b). Cartilage repair strategies for the knee are well-established and produce improvements in clinical outcomes for patients[19,20]. However, repair of hip cartilage is less frequently performed than repair of knee cartilage. The use of bone marrow stimulation, grafting and cell-based techniques for articular cartilage repair are discussed in the following section.

Bone marrow stimulation and augmentation. Bone marrow stimulation techniques for small (<4 cm^2), contained, defects have evolved from open debridement of damaged cartilage and removal of subchondral bone to the Steadman microfracture technique[21], in which the calcified cartilage is removed and an awl is used to create perforations in the subchondral plate. Bone marrow released into the defect forms a blood clot, which might ultimately lead to the formation of fibrocartilage. Unlike hyaline cartilage, fibrocartilage is rich in type I collagen and is of limited durability. Individuals treated with microfracture show initial clinical improvement after surgery, but have an accelerated decline in clinical outcome scores and a higher failure rate during long-term follow-up than those treated with osteochondral autograft treatment[22,23]. To overcome the shortcomings of microfracture, augmented bone marrow stimulation techniques were subsequently developed, including the concomitant injection of molecules such as growth factors, the use of acellular scaffolds (such as collagen membranes) or liquid hydrogels, and the use of micronized acellular cartilage extracellular matrix from allografts[24]. However, more high-quality studies are needed to demonstrate the superiority of augmented bone marrow stimulation techniques over other established procedures, such as microfracture or autologous chondrocyte implantation (ACI)[25].

Autografts and allografts. Osteochondral autograft transfer delivers viable, mature hyaline cartilage–bone units into chondral defects. These osteochondral grafts can bear load in the early postoperative period, enabling faster rehabilitation than following other, currently available, cell-based cartilage repair strategies[26]. Osteochondral autograft transfer involves the harvesting of 'plugs' from regions of the distal femur that bear low loads (such as the intercondylar notch or medial or lateral trochlea) and, therefore, its use is reserved for small chondral defects (<2 cm^2) owing to limited graft availability[27].

The avascular nature of cartilage renders it immune privileged[28], thereby opening up the potential for allogeneic approaches. Osteochondral allograft transplantation does not have the donor site limitations of osteochondral autograft transfer and can be used in revision surgery for failed cartilage repairs, making osteochondral allografting an appealing technique, although the availability of allograft tissue limits its use. Matching allografts to the shape and contours of the native knee architecture can also be difficult to achieve, potentially creating biomechanical loading imbalances and resulting in degenerative joint changes[29,30]. Techniques to improve the viability of chondrocytes in fresh osteochondral allografts and to accelerate the remodelling of graft tissue into host tissue are continually being investigated because both factors seem to be important for the longevity of the transplanted allograft[31,32].

Both osteochondral autograft transfer and osteochondral allograft transplantation have produced high rates of long-term graft survival, as well as high degrees of reported patient satisfaction and return-to-play among athletes[26,33–35]. For example, a 2016 systematic review found that ~90% of patients who underwent osteochondral autograft transfer had good or excellent outcomes at up to 10 years after surgery[19]. Another study showed that the survival of fresh osteochondral allografts was 82% at 10 years and 66% at 20 years after transplantation[33]. Cryopreserved osteochondral allografts (Cartiform), fresh osteochondral allografts (ProChondrix) and particulated juvenile allograft cartilage (DeNovo NT), which are processed by laser cutting or mincing, have also been used to treat articular cartilage defects[36]; however, short-term and long-term data are needed to determine the clinical success of these products.

Debridement
The removal of damaged tissue and/or torn fragments from a defect.

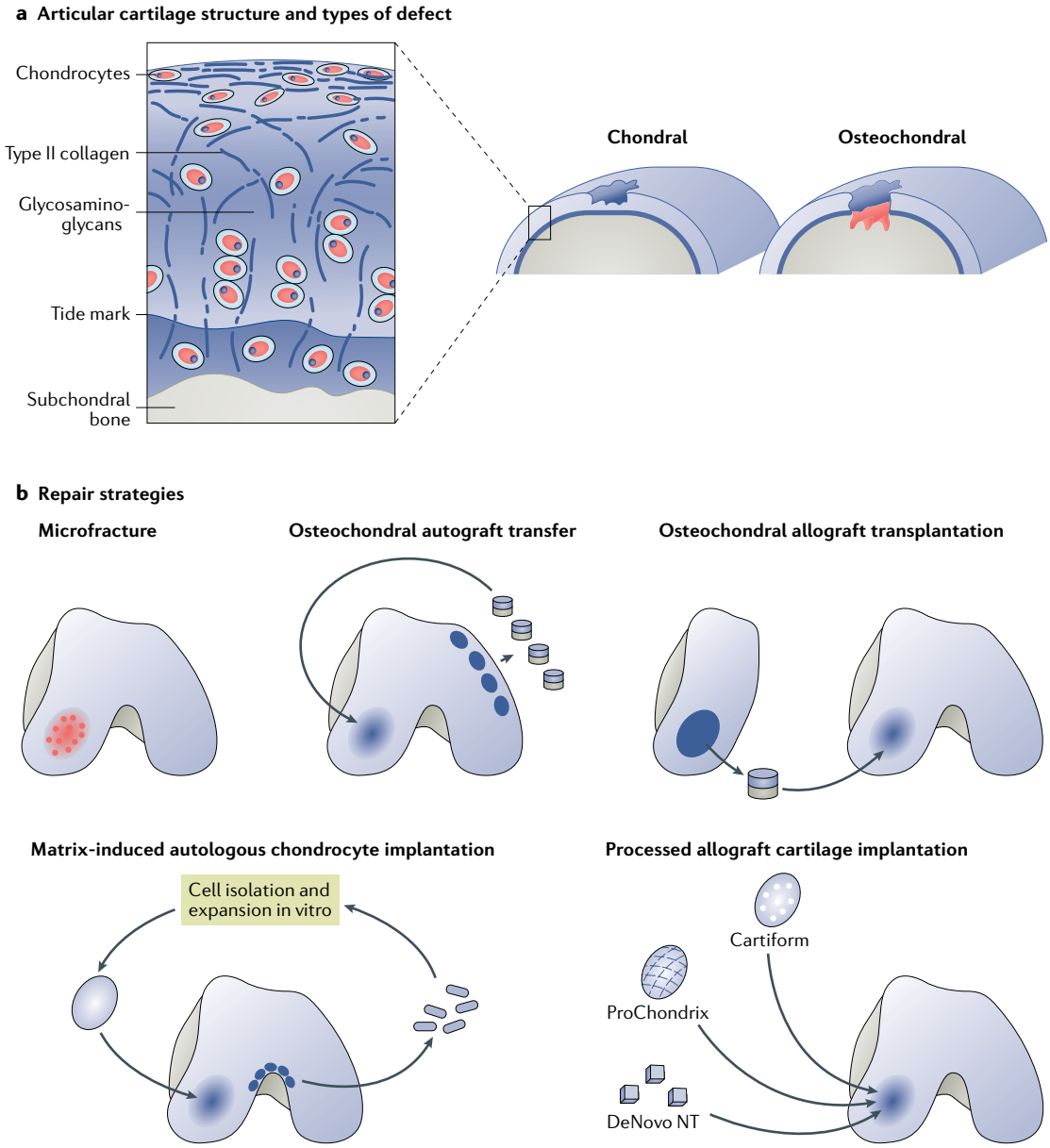

Fig. 1 | **Articular cartilage structure and treatment methods. a** | Articular cartilage consists of chondrocytes embedded in a defined structure of collagen fibres and glycosaminoglycans. Two main types of defect can occur: chondral defects, which only penetrate the cartilage, and osteochondral defects, which also penetrate the subchondral bone. **b** | Currently used repair strategies for cartilage defects include microfracture, osteochondral autograft transfer, osteochondral allograft transplantation, implantation of processed allograft cartilage such as DeNovo NT, ProChondrix and Cartiform, and matrix-induced autologous chondrocyte implantation. The choice of treatment method depends on the size and type of the defect, the expertise and preferences of the surgeon and patient-specific factors such as age and activity level.

Cell-based techniques. Current cell-based cartilage repair techniques enable the implant to be contoured to the recipient defect, making these techniques attractive for treating large (>3–4 cm^2) chondral lesions in areas with variable topographies, such as the patellofemoral joint or acetabulum. ACI requires two operations: chondrocytes are harvested from healthy articular cartilage in one operation and are then re-implanted into the chondral defect in a second operation after expansion in culture. A newer iteration of this technique, known as matrix-induced ACI (MACI), includes seeding of the chondrocytes onto a scaffold before implantation[37]. Patients treated with MACI have reported substantial long-term improvements in knee function and high rates of satisfaction[38,39]. In one study, at 5 years after surgery, 93% of patients expressed satisfaction with their postoperative pain relief, 90% had an improved ability to perform daily activities and 80% were able to participate more in sports compared with before the operation[38]. However, procedures that require only one operation are currently more appealing for clinicians than ACI or MACI.

Repairing meniscus defects

Two semicircular, wedge-shaped menisci are located between the distal femur and the tibial plateau and serve to distribute loads and protect articular cartilage. Each meniscus has two distinct regions (FIG. 2a): the outer, vascular, neural region (the red–red zone), which contains elongated fibroblast-like cells and predominantly type I collagen, and the inner, avascular, aneural zone (the white–white zone), which contains rounded chondrocyte-like cells (fibrochondrocytes) and predominantly type II collagen. These two zones are separated by the red–white zone, which has characteristics of both the red–red zone and the white–white zone. The meniscus functions by distributing load through its circumferentially aligned collagen fibres (FIG. 2a). Meniscus tears disrupt this function; however, only a small proportion of tears are considered repairable on the basis of tissue vascularity, tear pattern, anatomical location and tear acuity (FIG. 2b). For example, vertical longitudinal tears within the red–red or red–white zone of the meniscus are often amenable to repair[40]. Horizontal and radial tears are thought to rarely heal owing to incursion into the avascular white–white zone. Furthermore, radial tears disrupt the circumferential collagen fibres that are critical for maintaining hoop stresses, whereas circumferential vertical or horizontal tears can leave the meniscus with the potential for residual functionality because these tears follow the circumferential collagen fibres. The length, depth and size of tear, as well as joint stability and other patient-related factors such as age and symptoms also affect healing[41,42]. Despite our understanding of the crucial function of the meniscus in knee biomechanics, partial meniscectomy to remove unstable, damaged portions of the tear remains the gold standard for surgical treatment of meniscus tears, and accounts for half of the knee arthroscopic procedures performed in the USA[43]. However, both partial and total meniscectomy are linked to the development of knee OA[44], a fact that provides motivation for the development of novel interventions such as cell-based regenerative therapies.

Reduction of meniscal tears. Lesions in the meniscus that are mechanically unstable, complex or of a degenerative nature are conventionally treated with partial meniscectomy; however, attempts to reduce meniscal tears instead of performing partial meniscectomy have become more common during the past 15 years[45] (FIG. 2c). Meniscus defect reduction (often described by clinicians as meniscus repair) is usually accomplished by closure of the tear with sutures and/or anchors. For example, suturing of defects in the red–red and red–white zones led to satisfactory clinical healing in 76% of patients with meniscal tears[46]. Tear reduction also resulted in meniscus preservation without degeneration in younger patients (aged between 16 and 52 years)[47,48]. Meniscal tear reductions performed concurrently with ACL reconstruction have superior healing rates than meniscal tear reductions alone[49], potentially owing to the intra-articular release of cells and growth factors from the bone marrow that occurs when drilling a bone tunnel during ACL reconstruction[50]. Parameters affecting meniscus repair are probably multifactorial, but biological augmentation techniques, such as mechanical stimulation of the adjacent synovium or meniscus by rasping or radial trephination[51,52], the addition of an exogenous fibrin clot[53] or the introduction of bone marrow stem cells by marrow venting[54], are thought to promote healing.

Allografts. Meniscus allograft transplantation is the only option for total meniscus replacement, and is widely performed following total or near total meniscectomy (FIG. 2d). Allograft transplantation is indicated in patients who have a stable, correctly aligned joint and, at most, early knee OA[55]. Meniscus allografts can be inserted with several forms of attached bone, such as bone plugs, a common bone bridge or a hemi-plateau, or without attached bone[56]. In particular, meniscus fixation using bone plugs leads to better load transmission than fixation without using bone plugs[56]. Appropriate allograft sizing to the recipient knee[56] is also an important factor for tissue healing[57] and for the preservation of knee biomechanics[58]. Allograft recipients have good rates of clinical improvement. In a long-term follow-up study (mean 152 months) in 30 patients who received meniscal allografts, all patients had improved function (as measured by Lysholm score, short form-36 (SF-36) score and Knee Injury and Osteoarthritis Outcome Score (KOOS)), and 90% were satisfied with the outcome of the surgery[59]. However, meniscus replacement does not prevent joint space narrowing[60].

Synthetic implants. Partial meniscus replacements, such as collagen meniscus implants (CMI, available in the USA) and polyurethane polymeric implants (Actifit, available in Europe), can be used in patients with segmental meniscus defects, an intact peripheral rim and limited articular cartilage damage[61]. CMI provided substantial pain relief and functional improvement and had a low rate of implant failure at follow-up (mean 9.6 years) in patients receiving implants following partial meniscectomy[62]. Similarly, polyurethane polymeric implants improved clinical outcomes in patients following partial meniscectomy up to 4 years after implantation[63]. For replacement of the entire meniscus, a polyethylene-reinforced polycarbonate urethane prosthetic (NuSurface) is currently in FDA clinical trials[64]. Although synthetic meniscus implants can improve clinical outcomes, their use is limited by several shortcomings and technical difficulties: synthetic implants do not result in meniscus regeneration; the ability of synthetic implants to stop progression of OA is unproven; synthetic implants are difficult to place properly within the defect using an arthroscopic approach; and synthetic implants are challenging to handle and suture[65]. Therefore, a great need exists for cell-based approaches that can regenerate damaged meniscus.

Age-related differences in outcomes

Parameters that affect the outcomes of articular cartilage and meniscus repair are multifactorial, but generally, increased patient age has a negative correlation with good outcomes, in particular after bone marrow stimulation techniques. Treatments that are acceptable for use in paediatric and adolescent patients might not be suitable for use in adults, who tend to have degenerative,

Hoop stresses
Compressive forces experienced by the meniscus in the circumferential direction.

Rasping
Mechanical scraping to expose fresh and/or bleeding tissue.

Radial trephination
Puncturing small holes into the joint lining and/or synovium and into the tissue to stimulate healing.

Bone plugs
Created or fashioned bone cylinders containing the enthesis of the meniscal roots.

Common bone bridge
Excised bone containing and preserving the anatomic relationship between the anterior and posterior meniscal horns (also known as 'slot').

Hemi-plateau
Half of the tibial plateau, containing the articular surface, subchondral bone and meniscus with root attachments.

Lysholm score
A scoring system used to measure changes in limping, support, locking, instability, pain, swelling, stair climbing and squatting (originally developed to evaluate outcomes of knee ligament surgery).

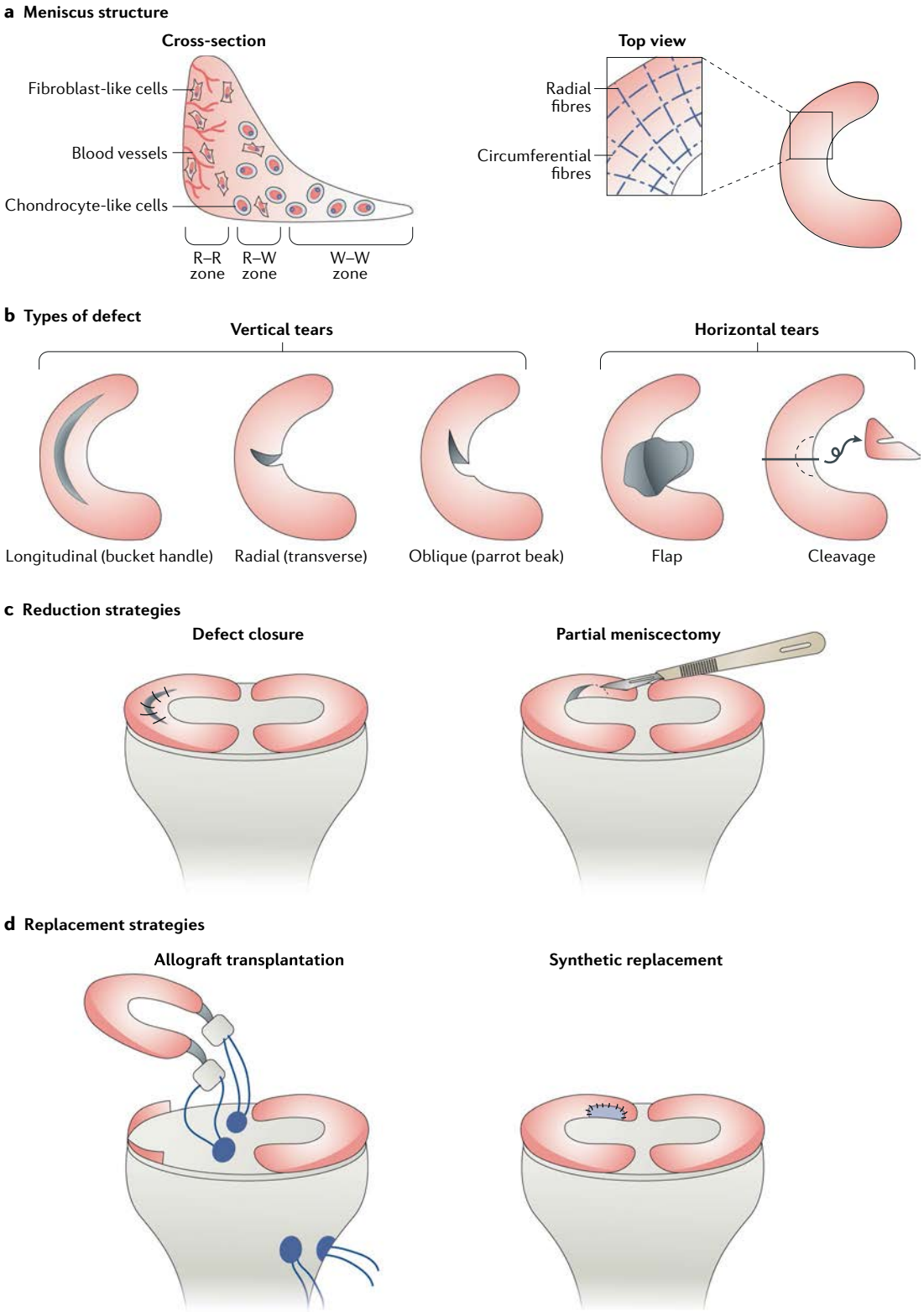

Fig. 2 | **Meniscus structure and treatment methods. a** | The meniscus consists of three main zones: red–red (R–R), red–white (R–W) and white–white (W–W). The R–R zone is fully vascularized and the W–W zone is avascular. **b** | A variety of different types of defect can occur in the meniscus, some of which are easier to repair than others owing to their intrusion into vascular or avascular zones. **c** | Reduction strategies in current use include defect closure with sutures or anchors and the trimming of torn pieces (partial or total meniscectomy). **d** | Replacement strategies in current use include allograft transplantation and the use of synthetic implants. As with articular cartilage, the size and type of defect, the expertise and preferences of the surgeon and patient-specific factors such as age and activity level affect the choice of treatment method.

rather than acute traumatic, lesions. Two main principles exist for treating paediatric articular cartilage or meniscus defects: techniques must be effective to help prevent the risk of developing OA at a young age; and joint anatomy and functionality must be restored to ensure symptomatic relief and resumption of pre-injury levels of physical activity[66]. Given the increase in paediatric joint injuries[67,68], potentially as a result of increased participation in sports, the development of therapies that will withstand the test of time is greatly needed.

Treatment of articular cartilage defects in young patients. Although many of the same techniques are used to treat cartilage lesions in children and adolescents as in adults, outcomes can differ. For microfracture, patients older than 40 years had worse outcomes than younger patients (<30 years of age) in many studies[69–72], potentially because older patients have fewer bone marrow progenitor cells and diminished regenerative capacity compared with younger patients. A similar trend occurs with osteochondral autograft transfer, for which better outcomes have been reported in young patients (<30 years of age)[73]. By contrast, 88% of paediatric and adolescent patients had successful outcomes following osteochondral allograft transplantation after a median of 2.7 years[74], similar to success rates reported in adults[75]. ACI in young patients (≤18 years of age) produced an improvement in postoperative outcomes in 84–96% of patients at 2–4 years of follow-up[76,77], which was higher than the rate of improvement in adults for the same follow-up period (78–83%)[78,79]. Overall, in younger patients (≤40 years of age), many of whom are athletes, osteochondral autograft transfer[22,80] and ACI or MACI[81] might result in better long-term outcomes and higher rates of return-to-play than microfracture.

Treatment of meniscus defects in young patients. As with articular cartilage, outcomes associated with treating meniscus pathologies differ as a result of multiple factors, including age and tear type. In general, meniscus allograft transplantation is indicated in young patients (<50 years of age) with meniscal deficiency, and is contraindicated in patients with evidence of advanced OA[82]. In patients aged 16 years or younger, an improved Lysholm score and a revision rate of 22% have been reported after a mean follow-up of 7.2 years following meniscus allograft transplantation[83]. For meniscal tear reduction, most studies in a meta-analysis showed little difference in failure rates between patients under and over the age of 40 years[84,85]. Another meta-analysis on meniscus repair that included 13 studies in adults showed a healing rate of 62–79% and a pooled re-tear rate of 23% after >5 years[86]. Comparisons between surgical outcomes in paediatric and adolescent patients versus adult patients need to take into consideration the types of tear that are being reduced. In paediatric and adolescent patients, meniscus defect reduction can be attempted for most meniscal tears regardless of zone, size and patient-specific factors, as the priority is to preserve the knee. By contrast, in adults, meniscus defect reduction is usually only performed for tears that have a high potential to heal, such as peripheral tears. Thus, despite the beneficial healing environment in paediatric and adolescent patients that results from a high degree of vascularization and increased cellular metabolism[87,88], healing rates in paediatric and adolescent patients compared with adult patients can seem similar because of the types of tears that are treated.

Tissue engineering strategies

Current surgical approaches do not provide long-term solutions for articular cartilage and meniscus regeneration, but tissue engineering techniques could provide alternative treatment strategies. Scaffolds, cells and biochemical and biomechanical stimuli, the main tools used to create engineered tissues (FIG. 3), are discussed in this section, as well as advances in cartilage engineering and the results of preclinical and clinical studies using engineered articular cartilage and meniscus products.

Scaffold and scaffold-free approaches

A variety of synthetic or natural materials, including polylactides, polyglycolides and silk, have been investigated for use as scaffolds for engineered articular cartilage[89] and meniscus[88]. Decellularized cartilage-derived matrix has also been investigated for use as a scaffold in cartilage regeneration[90,91]. For example, decellularized cartilage-derived matrix scaffolds inhibit the hypertrophic differentiation of embedded mesenchymal stem cells (MSCs) and promote the synthesis of cartilage matrix by these cells[90]. Decellularized extracellular matrix scaffolds derived from inner and outer regions of the meniscus support the differentiation of MSCs towards fibrochondrocyte and elongated fibroblastic phenotypes, respectively[91]. Various other types of scaffolds, including hydrogels and porous polymeric structures, are also under investigation for use in articular cartilage and meniscus tissue engineering. For example, injectable hydrogels, which can form irregular shapes to better fill defects, enable the use of minimally invasive implantation methods[92]. In the past 20 years, both natural materials (for example, alginate and hyaluronan) and synthetic materials (for example, polycaprolactone and polylactic acid) have been used in 3D printers to create anatomically shaped scaffolds for articular cartilage and menisci[93,94]. The advantages of using scaffolds for cartilage engineering include the ability to incorporate growth factors into the scaffold and the initial mechanical stability that they provide[95].

Despite the advantages of scaffolds, scaffold use can also result in degradation-associated toxicity, stress shielding, altered cell phenotypes and hindrances to remodelling[95]. These difficulties have provided the motivation for investigations into scaffold-free techniques to engineer cartilage[96] and menisci[97]. In particular, the scaffold-free self-assembling process facilitates cell-to-cell interactions by minimizing free energy, and recapitulates the conditions of cartilage development, which result in changes in the ratios of chondroitin 6-sulfate to chondroitin 4-sulfate and type VI collagen to type II collagen within the engineered neocartilage as it develops[98]. Through the use of biochemical and biomechanical stimuli, cartilage engineered using a scaffold-free approach has attained functional properties on a par with native tissue[99]. For example, engineered articular

Stress shielding
Protection of tissue from normal mechanical stresses by the presence of a much stiffer implant, often resulting in tissue loss.

Self-assembling process
A scaffold-free technology that produces tissues that demonstrate spontaneous organization without external forces via the minimization of free energy through cell-to-cell interactions.

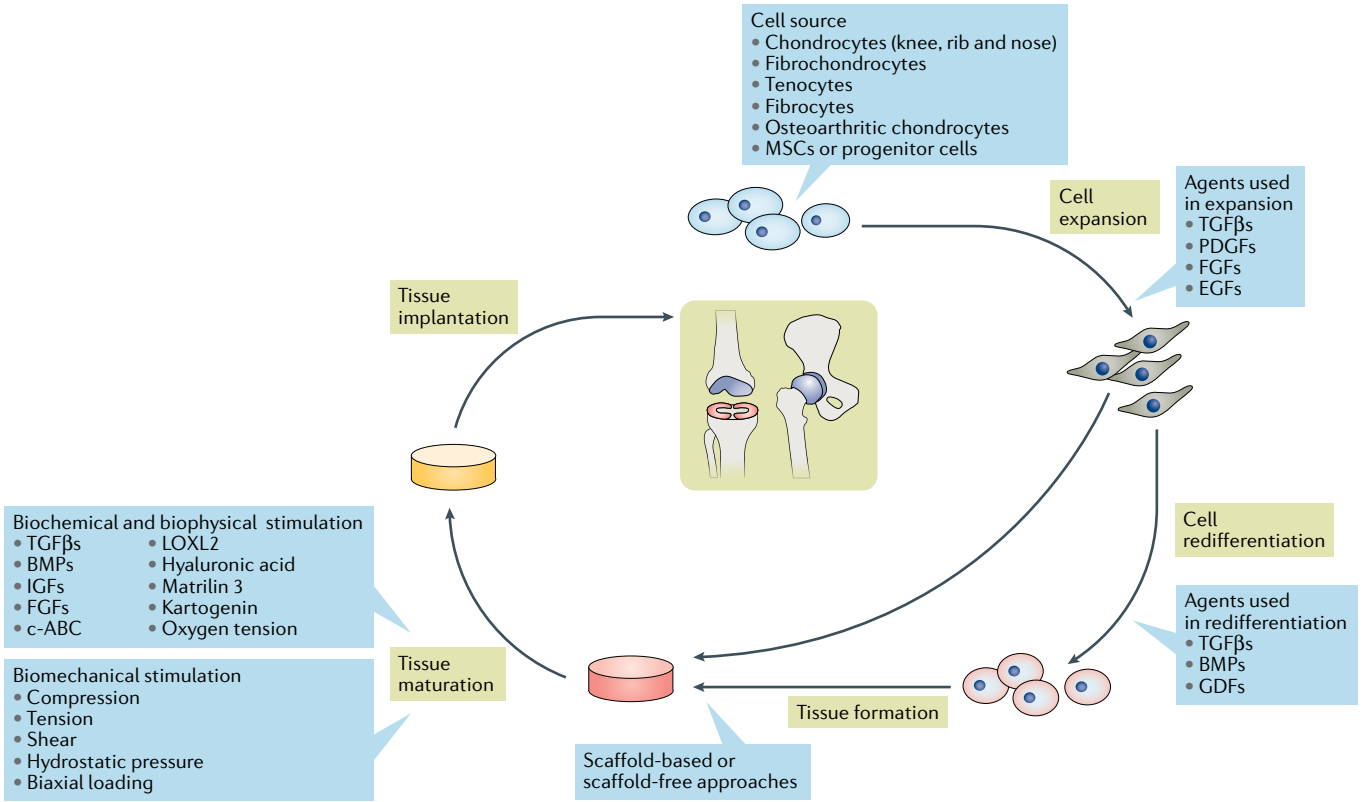

Fig. 3 | **Advances in tissue engineering strategies for articular cartilage and meniscus.** Engineered implants go through several stages of development that can be modified or enhanced by the addition of appropriate stimuli. The source of cells is important, as many cells dedifferentiate in culture. Alternative cell sources currently being trialled include non-articular chondrocytes, tenocytes, fibrocytes, osteoarthritic chondrocytes and stem cells or progenitor cells. Growth factors such as transforming growth factor βs (TGFβs), platelet-derived growth factors (PDGFs), fibroblast growth factors (FGFs), epidermal growth factor (EGF), bone morphogenetic proteins (BMPs) and growth and differentiation factors (GDFs) are used to effectively expand and help to redifferentiate cells before neotissue formation. Scaffold-based and scaffold-free methods can be used to engineer articular cartilage and menisci, and biochemical and biophysical factors such as TGFβs, BMPs, insulin-like growth factors (IGFs), FGFs, chondroitinase ABC (c-ABC), lysyl oxidase-like 2 (LOXL2), hyaluronic acid, matrilin 3, kartogenin and variations in oxygen tension are used to promote the maturation of engineered tissues. Similarly, biomechanical stimulation by, for example, compression, tension, shear, hydrostatic pressure and biaxial loading, can be used to improve the functional properties of the neotissue. MSC, mesenchymal stem cell.

cartilage has achieved compressive and tensile moduli of ~0.32 MPa (REF.[100]) and ~8 MPa (REF.[99]), respectively, which are within the ranges of values for native articular cartilage (0.1–2 MPa and 5–25 MPa, respectively)[101]. Similarly, scaffold-free engineered menisci have compressive and tensile moduli of ~0.12 MPa (REF.[102]) and ~5 MPa (REF.[103]), respectively, compared with the ranges of values for native tissue of 0.1–0.15 MPa and 10–30 MPa, respectively[88]. Thus, scaffold-free methods have the potential to circumvent challenges associated with scaffolds and to produce biomechanically functional implants.

Advances in scaffold-based and scaffold-free approaches have also focused on the recapitulation of native tissue architecture[104–107]. For example, stiffness gradient hydrogels (0.005–0.06 MPa) derived from poly(ethylene glycol) and chondroitin sulfate yield constructs with stiffness-dependent glycosaminoglycan gradients that mimic the glycosaminoglycan gradient found in articular cartilage between the superficial and deep zones[104]. In another study, bi-layered poly(ε-caprolactone) scaffolds with porous layers and aligned fibrous layers supported the development of zonal arrangement of engineered cartilage[105]. Collagen density and the alignment of porous collagen scaffolds can also be tailored via biaxial compression[106], which might be useful for engineering anisotropy in the meniscus. Scaffold-free approaches have also been used to generate zonal tissue and anisotropy; for example, anisotropic menisci with zonal variations have been produced using the self-assembling process[107]. These studies[104–107] suggest that recapitulating zonal and anisotropic properties of cartilage and menisci might be necessary to impart native functional properties to a tissue-engineered product.

Anisotropy
Having directionally dependent properties.

Engineering articular cartilage

Cell sources. Although chondrocytes are the obvious choice for use in engineering articular cartilage, the scarcity of chondrocytes necessitates cell expansion in vitro, which results in rapid dedifferentiation[108]. Although, to date, there is no evidence that dedifferentiated cells can be redifferentiated in vivo, the results of some studies have suggested that redifferentiation can be

accomplished in vitro[109,110]. For example, culturing either in vitro expanded chondrocytes or MSCs under 3D culture conditions supplemented with transforming growth factor-β1 (TGFβ1), growth and differentiation factor 5 (GDF5) and bone morphogenetic protein 2 (BMP2), collectively termed aggregate redifferentiation, resulted in increased expression of the chondrogenic genes *SOX9*, *ACAN* and *COL2A1* compared with untreated cells[111]. Alternative cell sources include chondrocytes from non-articular cartilages; for example, costal (rib) chondrocyte-derived neocartilage has compressive properties on a par with those of native articular cartilage[109]. HOX-negative nasal chondrocytes are thought to possess greater self-renewal capacity than articular chondrocytes[112] and a nasal chondrocyte-based articular cartilage product (N-TEC) is currently in clinical trials for articular cartilage repair in Europe[113]. In addition, constructs engineered using osteoarthritic chondrocytes have yielded neocartilage containing type II collagen and lubricin, but not type I collagen or type X collagen, which are indicative of chondrocyte dedifferentiation and hypertrophy[114]. Thus, non-articular and osteoarthritic cartilage might yield viable cells for use in articular cartilage repair.

Adult MSCs derived from adipose tissue, bone marrow, synovium or skin have been extensively investigated for use in cartilage tissue engineering. Bone marrow-derived MSCs and umbilical cord blood-derived MSCs are already used to create engineered cartilage repair products, and dermis-derived MSCs and precursor cells have chondrogenic differentiation potential[115,116]. Other types of MSCs and progenitor cells are emerging as candidates for use in tissue engineering. For example, peripheral blood-derived MSCs and endothelial progenitor cells have both been used to fill osteochondral defects in rabbits[117,118]. In a non-controlled, clinical pilot study with 15 participants, adult $CD146^+$ cartilage progenitor cells formed hyaline-like cartilage when implanted into knee articular cartilage defects[119]. After 12 months, the improvement in the International Knee Documentation Committee (IKDC) score was 52% and the improvement in the Lysholm score was 71% compared with preoperative scores[119]. Notably, hypertrophy frequently occurs in MSCs during in vitro chondrogenic differentiation[120], indicating the possibility that MSC-derived neocartilage might progress towards endochondral ossification[121], resulting in neotissue that is not suitable for cartilage repair and regeneration. Thus, despite promising early data, the long-term (>1 year) durability of MSC-derived tissues remains to be investigated.

Biochemical stimuli. Growth factors have long been recognized as important factors in neocartilage formation[122], but other molecules are emerging as potential modulators of engineered cartilage. In the past few years, hyaluronic acid has been shown to stimulate chondrogenesis and reduce hypertrophy in bone marrow-derived MSCs[123] and in a co-culture of adipose-derived MSCs and chondrocytes[124]. Similar effects have also been shown for the addition of matrilin 3 to cultures of bone marrow-derived MSCs[125]. The addition of kartogenin induced chondrogenic differentiation in MSCs and reduced type II collagen breakdown by 1.8-fold in a mouse model of OA[126]; however, the therapeutic dose and long-term in vivo efficacy of kartogenin have yet to be determined, limiting its use[127]. Biophysical stimuli such as glycosaminoglycan-depleting enzymes (such as chondroitinase ABC) or crosslinking agents (such as lysyl oxidase-like 2 (LOXL2)) have also been used to increase collagen content and to form collagen crosslinks, leading to improved tensile properties in neocartilage[128–130]. In fact, a regimen of TGFβ1, chondroitinase ABC and LOXL2 applied after aggregate redifferentiation generated neocartilage with tensile modulus and ultimate tensile strength values approximately twice those of untreated neocartilage[99]. Oxygen tension also has an important role in chondrogenesis and in improving neotissue functional properties. In one study, hypoxia upregulated *LOX* expression in chondrocytes by 18-fold, leading to an increase in tensile stiffness of neocartilage by ~80% compared with neocartilage formed under normoxic conditions[131]. Overall, these studies suggest that novel biochemical and biophysical stimuli should be used for effective neocartilage formation.

Biomechanical stimuli. Biomechanical stimuli such as compression, shear and hydrostatic pressure are important for cartilage homeostasis and are already used to improve the properties of engineered cartilage[132]. One advance in the use of biomechanical stimuli in tissue engineering has been the application of these stimuli to non-articular chondrocytes. Passive axial compression applied to costal chondrocytes increased the instantaneous modulus of engineered constructs by up to 92% compared with unstimulated neocartilage constructs[133]. Tension has also been trialled as an additional stimulus to improve the biomechanical properties of neocartilage. Tension stimulation of scaffold-free neocartilage treated with TGFβ1, chondroitinase ABC and LOXL2 resulted in increases of almost six-fold in tensile modulus and strength[99]. After in vivo implantation, these constructs had 90% of the collagen content and up to 94% of the tensile properties of native tissue[99]. A combination of compression and shear has also been tested, and resulted in a substantial increase in type II collagen production by chondrocytes in engineered neocartilage[134]. The results of these studies suggest that biomechanical stimulation has a pivotal role in engineering functional cartilage tissue in vitro. Understanding biomechanical stresses in the native environment of the joint, as well as their effects on both the generation of robust neotissue in vitro and the generated tissue in vivo, is important for achieving clinical translation of engineered cartilage.

Engineering menisci

Cell sources. Although meniscal fibrochondrocytes might seem to be an obvious choice for engineering the meniscus, co-culturing these cells with others might be required to achieve the best results. Similar to chondrocytes, meniscal fibrochondrocytes dedifferentiate when expanded[135], a fact that has led to the investigation of MSCs from the bone marrow[136], synovium[137] and adipose tissue as alternative cell sources[138]. In a 2017 study,

International Knee Documentation Committee (IKDC) score
A scoring system used to measure symptoms, sports and daily activities, current knee function and function before injury.

COL1A1, *COL2A1*, *ACAN* and *SOX9* were induced in tonsil-derived MSCs, and the feasibility of using these cells to repair meniscus defects was shown in rabbits[139]. Co-culture of synovium-derived stem cells and meniscus cells at a ratio of 1:3 increased glycosaminoglycan production by ~82% compared with stem cell monoculture and by ~33% compared with meniscus cell monoculture[140]. These findings echo those of studies investigating the formation of neomenisci using co-cultures of chondrocytes and differentiated cells[141] (such as tenocytes, ligament fibrocytes or meniscus fibrochondrocytes). For example, neomenisci formed using 50% articular chondrocytes and 50% meniscal fibrochondrocytes contain 700% more glycosaminoglycan and 90% more collagen than neomenisci formed using fibrochondrocytes alone[97]. The identification of new cell sources, as well as the optimization of co-culture systems, will both be important for overcoming the hurdles of cell culture for meniscus tissue engineering.

Biochemical stimuli. Growth factors including members of the TGFβ family, fibroblast growth factors (FGFs), platelet-derived growth factors (PDGFs) and epidermal growth factor (EGF) have shown efficacy in improving extracellular matrix production in engineered meniscus[88]. The addition of TGFβ1 and FGF2 stimulated collagen synthesis in meniscus constructs by 144% and 60%, respectively, compared with untreated constructs, although only TGFβ1 was effective in stimulating glycosaminoglycan production[142]. Growth factors have also been used to induce lubrication in engineered menisci; the use of insulin-like growth factor 1 localized lubricin to the neotissue surface and resulted in a coefficient of friction of ~0.2 (REF.[143]). Zonal development can also be engineered using growth factors. Modulating the release of TGFβ3 and connective tissue growth factor using 3D-printed scaffolds resulted in MSC-derived menisci with zone-specific *COL1A1* and *COL2A1* expression, as well as zone-specific production of type I and type II collagen[144]. Other biochemical stimuli can also aid the production of engineered menisci with improved functional properties. Treatment of neofibrocartilage implants with a combination of TGFβ1, LOXL2 and chondroitinase ABC increased collagen crosslink formation by 3.8-fold compared with untreated implants[103]. Upon implantation, the tensile strength of the interface of native meniscus and treated neofibrocartilage increased by 745% compared with the in vitro properties of untreated implants[103]. By contrast, changes in oxygen tension have yielded mixed results for engineering menisci. A 2017 study showed increased *ACAN* and *COL2A1* expression, as well as proteoglycan and type II collagen production by expanded human meniscus fibrochondrocytes under hypoxic conditions[145], whereas a 2013 study showed that normoxic conditions resulted in increased expression of *COL2A1* and *ACAN*, as well as the production of type II collagen and aggrecan by expanded human fibrochondrocytes compared with hypoxic conditions[146]. Therefore, modulation of oxygen tension as a biochemical stimulus might hold promise for meniscus engineering[130], but further investigations are needed to identify optimal culture conditions.

Biomechanical stimuli. The meniscus functions under compression, which results in the development of tensile hoop stress, therefore both of these mechanical forces are important for meniscus engineering. For example, using a compressive regimen of 10% strain at 1 Hz (which also results in tension), the collagen content, circumferential tensile modulus and radial tensile modulus of neomeniscus constructs can be increased compared with unstimulated constucts[147]. Over the past few years, studies of the development of biomechanical stimuli for meniscus engineering have focused on replicating the native zonal arrangement and matrix-level organization. For example, application of sinusoidal hydrostatic pressure between 0.55 and 5.03 MPa at 1 Hz for 4 h per day to aggregates of human fibrochondrocytes resulted in a substantial difference in type II collagen production between inner and outer zone meniscus fibrochondrocytes[148], providing support for the use of this stimulus to help recapitulate zonal architecture. A bioreactor applying 5–10% compressive strain was used to produce neomenisci with a fibrous collagen matrix in the outer zone that was similar in alignment to native tissue[149]. Investigations into how biomechanical stimuli can induce anisotropy in other engineered fibrocartilages have also been informative for meniscus engineering. For example, the application of passive axial compression during culture promoted anisotropic collagen organization similar to that seen in native tissue in tissue-engineered temporomandibular joint discs[150]. In addition to recapitulating native tissue biochemical and biomechanical properties, it is important to mimic other native features such as anisotropy and zonal organization because these structural features are necessary for meniscus function.

Clinical studies

The technologies used to produce cell-based repair products for articular cartilage repair have been reviewed elsewhere[151]. This section focuses on the clinical applications of articular cartilage and meniscus repair products in development (TABLE 1) and promising results from clinical trials of these products (TABLE 2). Acellular, scaffold-based products are not discussed. Additional clinical studies that have been performed under Institutional Review Board approval and in accordance with the principles of the Declaration of Helsinki, but not as part of registered clinical trials, are listed in Supplementary Table S1.

The majority of engineered cartilage products in the clinical pipeline, such as NOVOCART 3D and NeoCart, are manufactured using expanded autologous chondrocytes (TABLE 1). Because chondrocytes dedifferentiate upon in vitro expansion, products derived from expanded chondrocytes are likely to have inferior biomechanical properties to those of native tissue. Strategies such as the application of hydrostatic pressure have been developed to recover the chondrogenic phenotype. These strategies have resulted in articular cartilage repair implants that produce early-stage clinical improvements, but the long-term success and durability of these implants remains to be seen.

RevaFlex and CARTISTEM are both manufactured using allogeneic cells (TABLE 1). In a phase I/II

study, chondral defects treated with RevaFlex had grossly 'normal or nearly normal' cartilage repair (as measured by the International Cartilage Repair Society (ICRS)-Cartilage Repair Assessment System) with no signs of immunological response after 1 year in 66.7% of patients treated[152]. In a study in South Korea, treatment of chondral lesions with CARTISTEM improved clinical outcomes compared with preoperative scores and there were no signs of bone or tumour growth up to 7 years after surgery[153]. CARTISTEM has completed a phase I/IIa study in the USA[154]. The successful clinical outcomes of allogeneic therapies to date open up a new avenue for eliminating donor site morbidity and the extra surgical step of tissue harvest when treating cartilage lesions.

Although engineered cartilage products in the clinical pipeline are primarily indicated for knee defects, several products have also been used in the hip (TABLE 2). Treatment of acetabular chondral defects with BST-CarGel improved International Hip Outcome Tool (iHOT) scores by 46% in a retrospective case series of 37 patients[155]. In a prospective study of 13 patients, treatment of acetabular chondral delamination (average defect size 3.7 cm^2) with BST-CarGel resulted in over 90% filling by volume of each chondral defect after 2 years[156]. In another study, the application of either NOVOCART 3D Inject or co.don Chondrosphere to acetabular cartilage defects (average size 2.21 cm^2) produced substantial improvements in activity and quality of life and reduced pain after a mean of 19 months[157].

Compared with articular cartilage, few clinical trials have been carried out with engineered meniscus products (TABLE 2). For example, Cell Bandage, which is composed of autologous bone marrow-derived MSCs embedded in a collagen sponge, is placed between the torn edges of the meniscus and the defect is sutured closed. It is thought that the MSCs embedded in Cell Bandage release growth factors that promote defect repair[158]. In a first-in-human study, Cell Bandage improved IKDC scores by ~40 points, the Tegner–Lysholm score by ~40 points and the range of motion (ROM) score by ~10 degrees at 12 months after surgery, and these results were maintained at 24 months[158]. In another study, Chondrogen injections containing 50 million or 150 million allogeneic bone marrow-derived MSCs also substantially decreased patient-reported visual analogue scale pain scores for up to 24 months[159]. Although meniscus repair products are not as numerous as articular cartilage products and fewer clinical trials have been performed, preliminary clinical data suggest positive outcomes for cell-based therapies.

Challenges to clinical translation

Cell sourcing

Obtaining sufficient numbers of autologous cells remains a major limiting factor to the translation of engineered articular cartilage and meniscus products (FIG. 4a). As previously noted, sourcing cells from non-articular cartilages, such as costal cartilage, might be a solution to the lack of autologous chondrocytes, although passaging might still be necessary with these cells. Expression of *COL1A1* and *COL2A1* by these cells decreases after just one passage[108], but although this collagen expression profile is undesirable for engineering articular cartilage, passaged cells that express *COL1A1* might still be useful in meniscus tissue engineering because native meniscus contains ~80% type I collagen in the red–red zone[88]. Furthermore, a spectrum of engineered cartilages from hyaline to fibrous can be engineered from costal chondrocytes by modulating their redifferentiation after passaging[160]. Innovative use of cells and non-articular cartilage cell sources has the potential to greatly alleviate the scarcity of cells for autologous articular cartilage and meniscus therapies.

Biological variability

Biological variability between donors makes the consistent production of high-quality autologous neotissue difficult to achieve (FIG. 4a). Not all donors possess cells capable of forming robust neotissue. For example, chondrocytes sourced from 64–80-year-old donors exhibited variable expression of chondrogenic genes at passage two[161]. In cells from one group of donors, *COL2A1* expression increased when the cells were cultured as a microtissue compared with monolayer culture, whereas in cells from another group of donors, *COL2A1* expression did not increase upon microtissue culture[161]. Using allogeneic cells would reduce problems related to donor variability during manufacturing, but the allogeneic implants would need to be well tolerated by the recipient. Several cartilage repair products already include allogeneic cells or tissues (TABLE 1). Lending further credence to this approach, healing of temporomandibular joint disc defects using allogeneic neocartilage has been achieved in mini-pigs[162]. In that study, costal chondrocyte-generated neocartilage implants were well tolerated immunologically and resulted in a decrease in OA[162]. Although there is increased concern about disease transmission with the use of allogeneic approaches, tissue banks already provide allogeneic cells and tissues for transplantation in accordance with FDA guidance on donor screening and testing[163]. Thus, the use of well-characterized allogeneic cells might avoid disease transmission while mitigating the intractable problem of biological variability.

Achieving biomimicry

Insofar as the functions of articular cartilage and the meniscus are to distribute loads and enable frictionless joint movement, tissue engineering efforts should reflect these functions. Advances have been made in improving the robustness of engineered cartilage towards native tissue values; however, considerable efforts are still required to engineer tribological properties and durability into neocartilage and neomenisci to achieve biomimicry. It has been well documented that a functionality index (FI) enables comparison of the quality of engineered tissues relative to healthy native tissues[100,109,150]. However, to be more powerful, the FI should be modified to reflect the relevant salient properties of each target tissue, such as including the coefficient of friction for articular cartilage or an anisotropy index for the meniscus. Although complete biomimicry (FI = 1) in engineered cartilage has traditionally been the goal of tissue engineering approaches, a 2018 study[162] in which the implantation

International Cartilage Repair Society (ICRS)-Cartilage Repair Assessment System
A tool used to macroscopically evaluate the quality of cartilage repair tissue.

International Hip Outcome Tool
A tool used to measure symptoms, functional limitation, work-related concerns, sports and recreational activities, and social, emotional and lifestyle concerns using a visual analogue scale.

Tegner–Lysholm score
A patient-reported score of the effect of knee pain and stability on daily life.

Range of motion (ROM) score
A measurement of the range of flexion and extension of a joint.

Tribological properties
Functional properties relating to friction and lubrication of tissues.

Table 1 | **Cell-based tissue-engineered products for articular cartilage and meniscus repair**

Product name (company)	Cell or tissue source	Seeding density	Biomaterial or scaffold	Stimuli	Time between operations (time in culture)	No. of patient operations	Refs
Articular cartilage							
BioCart II (ProChon Biotech)	Autologous chondrocytes (passage number unknown)	0.4×10^6 cells plus 0.1×10^6 cells/cm^2 of scaffold	Freeze-dried fibrin–hyaluronan	Autologous serum and FGF2	3–4 weeks (3–4 days in 3D culture)	2	172,173
BioSeed-C (BioTissue SA)	Expanded autologous chondrocytes (passage number unknown)	20×10^6 cells per scaffold	Fibrin, polyglycolic acid, polylactic acid and polydioxanone	Autologous serum	4–5 weeks	2	174–176
BST-CarGel (Piramal Healthcare (Canada))	Autologous whole peripheral blood	3:1 ratio of autologous whole peripheral blood to biomaterial	Dissolved chitosan in glycerophosphate buffer	Unknown	n/a	1	177
CaReS (Arthro Kinetics Biotechnology)	Primary autologous chondrocytes	Unknown	Type I collagen hydrogel	Autologous serum	2 weeks (10–13 days in 3D culture)	2	178
Cartilage autograft implantation system (CAIS) (DePuy Mitek)	Autologous cartilage fragments	1–2 mm minced cartilage dispersed onto scaffold	Absorbable co-polymer of 35% polycaprolactone and 65% polyglycolic acid with a polydioxanone mesh	Unknown	n/a	1	179
Cartipatch (TBF Genie Tissulaire)	Expanded autologous chondrocytes (passage 3)	10×10^6 cells/ml of hydrogel	Agarose–alginate	Autologous serum	6-7 weeks	2	180,181
CARTISTEM (Medipost)	Expanded, allogeneic, umbilical cord blood-derived MSCs (passage number unknown)	500 µl of hydrogel per cm^2 of defect area, 5×10^6 cells/ml of hydrogel	Hyaluronic acid hydrogel	Fetal bovine serum	n/a	1	153
co.don Chondrosphere (co.don AG)	Expanded, autologous chondrocytes (passage number unknown)	10–70 spheroids/cm^2 of defect area or ~3×10^6 cells/cm^2 of defect area	Scaffold-free	Autologous serum	~5–10 weeks	2	182,183
HYALOFAST (Anika Therapeutics)	Autologous BMAC	2 ml BMAC per scaffold	Benzyl ester of hyaluronic acid (HYAFF-11)	Unknown	n/a	1	184
HYALOGRAFT C (Anika Therapeutics)	Expanded autologous chondrocytes (passage 1 or passage 2)	$1.5–4 \times 10^6$ cells per scaffold	Benzyl ester of hyaluronic acid (HYAFF-11)	Autologous serum and TGFβ1	4 weeks (2 weeks in 3D culture)	2	185–188
INSTRUCT (CellCoTec B.V.)	Autologous, primary articular chondrocytes and bone marrow-derived cells	Unknown	Poly((ethylene oxide) terephthalate-co-poly(butylene) terephthalate)	Unknown	n/a	1	189
NOVOCART 3D (Aesculap Biologics)	Expanded autologous chondrocytes (passage 1)	0.5–3 × 10^6 cells/cm^2 of scaffold	Type I collagen and chondroitin sulfate	Autologous serum	3 weeks (2 days in 3D culture)	2	190
NOVOCART Inject (TETEC AG)	Expanded autologous chondrocytes (passage number unknown)	Unknown	In situ polymerized injectable albumin–hyaluronic acid hydrogel	Autologous serum, BMP2 and insulin	Unknown (3–4 weeks in 2D culture)	2	157

Table 1 (cont.) | **Cell-based tissue-engineered products for articular cartilage and meniscus repair**

Product name (company)	Cell or tissue source	Seeding density	Biomaterial or scaffold	Stimuli	Time between operations (time in culture)	No. of patient operations	Refs
Articular cartilage (cont.)							
NeoCart (Histogenics)	Expanded autologous chondrocytes (passage number unknown)	12×10^6 cells/ml collagen solution	Bovine type I collagen	Hypoxia and hydrostatic pressure	6–12 weeks	2	191–193
N-TEC (BIO-CHIP)	Expanded autologous nasal chondrocytes (passage number unknown)	50×10^6 cells per membrane	Type I and type III collagen membrane (Chondro-Gide)	• Autologous serum, FGF2 and TGFβ1 (expansion) • Autologous serum, insulin and ascorbic acid 2-phosphate (3D culture)	≥7 weeks (2 weeks in 2D culture and 2 weeks in 3D culture)	2	194
RevaFlex (ISTO Technologies)	Expanded allogeneic juvenile chondrocytes (passage number unknown)	Unknown	Scaffold-free	Unknown	n/a	1	152
Meniscus							
Chondrogen (Mesoblast)	Expanded allogeneic adult bone marrow-derived MSCs (passage 2)	25×10^6 or 75×10^6 cells/ml of sodium hyaluronate	Sodium hyaluronate	Fetal bovine serum (expansion)	n/a	1	159
Cell Bandage (Azellon)	Expanded autologous bone marrow-derived MSCs (passage 1)	1×10^6 cells/cm^2 of scaffold	Collagen sponge from bovine corium	Fetal bovine serum and FGF (expansion)	>2 weeks (6 h in 3D culture)	2	158

Acellular, scaffold-based products are not included. The term 'chondrocytes' refers to articular chondrocytes unless otherwise specified. The sponsors and products listed here might since have been acquired by other companies. BMAC, bone marrow aspirate concentrate; BMP2, bone morphogenic protein 2; FGF, fibroblast growth factor; MSC, mesenchymal stem cell; n/a, not applicable; TGFβ1, transforming growth factor β1.

of engineered cartilage with an FI of 0.42 resulted in the complete healing of temporomandibular joint disc defects raises the question as to the degree of biomimicry necessary to achieve regeneration. It remains to be seen whether the achievement of biomimicry, especially with respect to biomechanical properties, imparts long-term durability to neotissue in vivo. Furthermore, no data exist to definitively show that the repair of articular cartilage and meniscus damage delays or halts the progression of OA. The ability of small defect repairs to stop OA progression would be difficult to assess in a well-controlled, randomized clinical trial owing to the need to include a no-treatment study arm and the long time-frames involved. Although evidence exists that neotissue with an FI of <1 elicits successful healing and that complete biomimicry might not be necessary[162], data on the long-term outcomes of using such an approach are lacking. Thus, it will be instructive to continue examining the degree of biomimicry necessary to ensure satisfactory long-term healing outcomes.

Implant integration and protection

The clinical translation of tissue-engineered products requires many factors to be taken into consideration beyond the manufacture of robust neotissue. Articular cartilage and the white–white zone of the meniscus are avascular, which makes integration of implants into existing native tissue difficult (FIG. 4a). The removal of anti-adhesive glycosaminoglycans and the priming of engineered tissue with collagen crosslinking agents are promising strategies that have shown preliminary success towards improving implant integration. For example, chondroitinase ABC treatment of native articular cartilage plugs before they are press-fitted into an articular cartilage annulus resulted in an integrated assembly with interfacial shear strength of 0.135 MPa, compared with 0.068 MPa in the untreated control[164]. In another study, LOXL2 treatment of similar assemblies of engineered cartilage and native cartilage rings resulted in a 2.2-fold increase in interfacial stiffness[165]. Implant integration can also be affected by postoperative recovery regimens. Unlike humans, animals operated on in preclinical studies will not obey strict rehabilitation regimens and might disrupt implant integration by engaging in impulsive physical activity immediately after surgery. Thus, in both animals and humans, the use of novel tissue-engineered implants might require novel surgical procedures that protect engineered implants and prevent implant displacement. For example, a reproducible intralaminar fenestration technique has been

Table 2 | **Clinical trials of cell-based tissue-engineered products for cartilage and meniscus repair**

Product (company)	Clinical status	Study location	No. of patients	Clinical indication	Comparator	Outcomes	Refs
Articular cartilage							
BioCart II (ProChon Biotech)	Phase II (status unknown)	USA and Israel	40 (estimated)	Single, contained cartilage defect on the femoral condyle of the knee (1.5–7.5 cm^2, depth up to 6 mm)	Microfracture	Results not published	195
BioSeed-C (BioTissue SA)	Phase III (ongoing)	Germany	80	Focal, contained, full-thickness cartilage defect on the lateral and medial condyles of the knee (Outerbridge grade III–IV)	chondrotissue (BioTissue SA)	Results not published	196
	Non-interventional study (completed 2016)	Germany	76 (target)	Focal cartilage defects on the femoral condyles, trochlea and patella of the knee (>2 × 2 cm and Outerbridge grade III–IV) that have been previously treated with BioSeed-C	None	Results not published	197
BST-CarGel (Piramal Healthcare (Canada))	Phase IV (terminated)	Canada and Europe	5	Single, focal, full-thickness cartilage defect on the femoral condyle of the knee (1.5–3 cm^2 and ICRS grade III–IV)	Microfracture	Results not published	198
	Phase III (status unknown)	Unknown	50 (estimated)	Focal chondral defects of the hip (>2 cm^2)	Microfracture	Results not published	199
	RCT (completed 2011)	Canada, South Korea and Spain	80	Focal cartilage defect on the medial femoral condyle of the knee (grade III–IV, unknown scoring system)	Microfracture	• Improved lesion filling and quality of repair tissue superior to microfracture alone at 12 months • Equivalent WOMAC scores and comparable safety outcomes between groups at 12 months	177
	Observational study (completed 2014)	Canada and Spain	67	Focal cartilage defects on the femoral condyle of the knee (ICRS grade III–IV or Outerbridge grade III–IV)	Microfracture	• Improved lesion filling and quality of repair tissue superior to microfracture alone at 5 years • No difference in WOMAC scores and comparable safety outcomes between groups at 5 years	200
Cartilage autograft implantation system (CAIS) (DePuy Mitek)	Phase III (status unknown)	Singapore	36 (estimated)	Full-thickness cartilage defect on the femoral condyle or trochlea of the knee (2–10 cm^2)	Microfracture	Results not published	201
	Clinical trial (terminated)	USA and Canada	75	One or two focal chondral defects (1–10 cm^2, depth up to 6 mm) or a non-osteochondritis dissecans lesion between grades I and III or an osteochondritis dissecans lesion between grades I and IV	Microfracture	Results not published	202
CARTIPATCH (TBF Genie Tissulaire)	Phase III (terminated)	Belgium	40	Isolated femoral osteochondral defect (2.5–7.0 cm^2, maximum depth of 10 mm, ICRS grade III–IV)	Microfracture	Results not published	203
	Phase III (completed 2013)	Belgium	64	Single femoral osteochondral defect (2.5–7.0 cm^2, maximum depth 10 mm, ICRS grade III–IV)	Microfracture	Results not published	204

Table 2 (cont.) | **Clinical trials of cell-based tissue-engineered products for cartilage and meniscus repair**

Product (company)	Clinical status	Study location	No. of patients	Clinical indication	Comparator	Outcomes	Refs
Articular cartilage (cont.)							
CARTIPATCH (TBF Genie Tissulaire)	Phase III (completed 2013)	France	47	Isolated femoral osteochondral defect (2.5–7.5 cm^2, ICRS grade III–IV)	Mosaicplasty	• Decreased IKDC score compared with mosaicplasty at 24 months • Decreased O'Driscoll score compared with mosaicplasty at 24 months	181
	Phase II (completed 2006)	France	17	Isolated chondral or osteochondral defect on the femoral condyles of the knee (1–5 cm^2, ICRS grade III–IV)	None	• Increased IKDC score at 24 months compared with baseline • 81% defect fill observed by MRI at 24 months	180
CARTISTEM (Medipost)	Phase I/II (completed 2017)	USA	12	Single, focal, full-thickness cartilage defect of the knee (≥2 cm^2, ICRS grade III–IV)	None	Results not published	154
	Phase III (completed 2015)	South Korea	103	Cartilage defect of the knee (2–9 cm^2, ICRS grade IV)	Microfracture	Results not published	205
	Phase III (completed 2011)	South Korea	104	Cartilage defect of the knee (2–9 cm^2, ICRS grade IV)	Microfracture	Results not published	206
	Phase I/II (completed, date unknown)	South Korea	7	Full-thickness cartilage defects of the knee (>2 cm^2, Kellgren–Lawrence grade III and ICRS grade IV)	None	• Maturing repair tissue by arthroscopy reported at 12 weeks • Improved VAS pain score and IKDC score at 24 months compared with pre-transplantation scores • Regenerated cartilage detected by MRI at 36 months • Improved outcomes stable and no signs of osteogenesis or tumorigenesis at 7 years	153
co.don Chondrosphere (co.don AG)	Phase III (active, not recruiting)	Germany and Poland	102	Isolated single chondral defect on the femoral condyle of the knee (1–4 cm^2, depth up to 6 mm, ICRS grade III–IV)	Microfracture	Results not published	207
	Phase II (completed 2018)	Germany	75	Isolated single chondral defect or osteochondritis dissecans lesion on the femoral condyle, trochlea, tibia or retropatella (4–10 cm^2, depth up to 6 mm, ICRS grade III–IV)	Different doses of co.don Chondrosphere	No substantial differences in the incidence of adverse events reported between the different doses	208
HYALOFAST (Anika Therapeutics)	Prospective study (recruiting)	USA and Europe	200 (estimated)	Cartilage defect on the femoral condyle or trochlea (1–6 cm^2, ICRS grade III–IV)	Microfracture	Results not published	209
INSTRUCT (CellCoTec B.V.)	Prospective study (completed 2014)	Europe	40	Cartilage defect on the femoral condyle and trochlea of the knee (modified Outerbridge grade III–IV)	None	• Graft delamination reported in two patients leading to treatment failure in one patient • ~90–100% defect filling at 24 months • Improved VAS pain score and IKDC score at 24 months compared with baseline • Improved KOOS at 12 months compared with baseline • Histological presence of hyaline cartilage in 72% of tissue samples and fibrocartilage and hyaline cartilage in 97% of tissue samples • Presence of repair tissue detected by MRI at 12 months	189

Table 2 (cont.) | **Clinical trials of cell-based tissue-engineered products for cartilage and meniscus repair**

Product (company)	Clinical status	Study location	No. of patients	Clinical indication	Comparator	Outcomes	Refs
Articular cartilage (cont.)							
NOVOCART 3D and NOVOCART 3D Plus (Aesculap Biologics, TETEC AG)	Phase III (recruiting); NOVOCART 3D	USA	30 (estimated)	Patients in whom microfracture failed in a previous trial	None	Results not published	210
	Observational study (active, not recruiting); NOVOCART 3D	Germany	81	Localized, full-thickness cartilage defect of the knee (2.5–10 cm^2, ICRS grade III–IV)	None	Results not published	211
	Phase III (recruiting); NOVOCART 3D	USA and Canada	233 (estimated)	Isolated cartilage defects on the femoral condyle of the knee (2–6 cm^2)	Microfracture	Results not published	212
	Phase III (active, not recruiting); NOVOCART 3D Plus	Europe	263	One or two cartilage defects on the femoral condyle and/or the trochlea of the knee (2–6 cm^2, ICRS grade III–IV)	Microfracture	Results not published	213
NOVOCART Inject and NOVOCART Inject Plus (TETEC AG)	Phase III (recruiting); NOVOCART Inject Plus	Europe	100	One or two focal cartilage defects on the femoral condyle, trochlea, patella or tibial plateau of the knee (4–12 cm^2, ICRS grade III–IV)	None	Results not published	214
	Non-interventional study (recruiting); NOVOCART Inject	Germany	245 (estimated)	'Insulated' full-thickness cartilage defects of the knee (2.5–10 cm^2, ICRS grade III–IV)	None	Results not published	215
	Observational study (active, not recruiting); NOVOCART Inject	Germany	21	'Insulated' full-thickness cartilage defects of the hip (1.5–10 cm^2, ICRS grade III)	None	Results not published	216
NeoCart (Histogenics)	Phase III (active, not recruiting)	USA	245	Cartilage defect of femur and/or trochlea of the knee	Microfracture	Results not published	217
	Phase II (completed 2014)	USA	30	Cartilage defect on the femoral condyle of the knee (ICRS grade III)	Microfracture	• No difference in adverse event rates between groups • Greater improvement in KOOS, IKDC and VAS pain scores at 6, 12 and 24 months compared with microfracture • Improved MOCART scores at 24 months compared with scores at 3 months • Improved KOOS, SF-36 and IKDC scores at 5 years compared with baseline • Decreased VAS pain score and improved range of motion at 5 years compared with baseline	191,218
	Phase I (completed, date unknown)	USA	8	Full-thickness cartilage defect on the femoral condyle of the knee (grade III, unknown scoring system)	None	• Improved VAS pain score at 12 months compared with baseline • Improved IKDC score and range of motion at 24 months compared with baseline • Six patients with 67–100% defect filling, one patient with 33–66% defect filling and one patient with <33% defect filling as determined by MRI • No arthrofibrosis or implant hypertrophy found	192

Table 2 (cont.) | **Clinical trials of cell-based tissue-engineered products for cartilage and meniscus repair**

Product (company)	Clinical status	Study location	No. of patients	Clinical indication	Comparator	Outcomes	Refs
Articular cartilage (cont.)							
N-TEC (BIO-CHIP)	Phase II (recruiting)	Europe	108 (estimated)	One or two localized cartilage defects on the femoral condyle and/or trochlea of the knee (2–8 cm^2, ICRS grade III–IV)	N-CAM (BIO-CHIP)	Results not published	113
	Phase I (completed 2018)	Switzerland	10	One or two cartilage defects on the femoral condyle and/or trochlea of the knee (2–8 cm^2, ICRS grade III–IV)	None	• No adverse events • Defect filling with repair tissue variable • Improved KOOS and IKDC scores at 24 months compared with pre-operative values • Approaching 'ideal level' of glycosaminoglycan content determined by ΔR_1 ($R_1 = 1/T_1$) and water and collagen contents 'similar to those in native tissue' at 24 months	194
RevaFlex (ISTO Technologies)	Phase III (terminated)	USA	14	One or two cartilage defects on the femur of the knee (≤5 cm^2)	Microfracture	Results not published	219
	Phase I/II (completed, date unknown)	USA	9	Up to two cartilage defects on the femoral condyle or trochlea of the knee (1–5 cm^2, ICRS grade III–IV)	None	• Improved patient-reported outcome measures at 12 months • Cartilage repair graded as grossly normal/near normal in 66.7% of patients at 12 months • Maturation of the implant (determined by defect filling and quality of repair tissue) observed by MRI at 12 months	152
Meniscus							
Chondrogen (Mesoblast)	Phase I/II (completed 2011)	USA	55	Following meniscectomy	Placebo (hyaluronan)	Results not published	220
	Phase I/II (completed 2008)	USA	55	Following meniscectomy	Placebo (hyaluronan)	• Three patients with >15% increase in meniscus volume in group receiving 50×10^6 cells, 0 in the control group and 0 in group receiving 150×10^6 cells at 24 months • Decreased VAS pain score and increased Lysholm score in all treatment groups at 24 months compared with baseline	159
Cell Bandage (Azellon)	Phase I (ongoing)	Europe	10	Meniscus tear that would otherwise be treated by meniscectomy (white–white zone)	None	Results not published	221

Acellular scaffold-based products are not included. The term 'Europe' refers to trials that took place in three or more European countries; if a trial took place in fewer than three European countries, all countries are listed. The sponsors and products listed here might since have been acquired by other companies. ICRS, International Cartilage Repair Society; IKDC, International Knee Documentation Committee; KOOS, Knee Injury and Osteoarthritis Outcome Score; MOCART, magnetic resonance observation of cartilage repair tissue; R_1, longitudinal relaxation rate; RCT, randomized controlled trial; SF-36, short form-36; T_1, longitudinal relaxation time; VAS, visual analogue scale; WOMAC, Western Ontario and McMaster Universities Osteoarthritis Index.

developed that enables engineered neocartilage to be secured into native tissue without directly suturing the implant[162]. Because implant integration, surgical techniques and rehabilitation all contribute to the efficacy of cartilage regeneration, developing appropriate protocols to address these factors should be as much of a priority for researchers as developing the implants themselves.

Inflammation and immunogenicity

Upon implantation, engineered neotissue must also withstand the pro-inflammatory environment of the injured or diseased joint. Chronic joint inflammation (as can be present in OA and RA) can be destructive to tissue-engineered implants and impede their integration and performance. Many studies have examined ways to

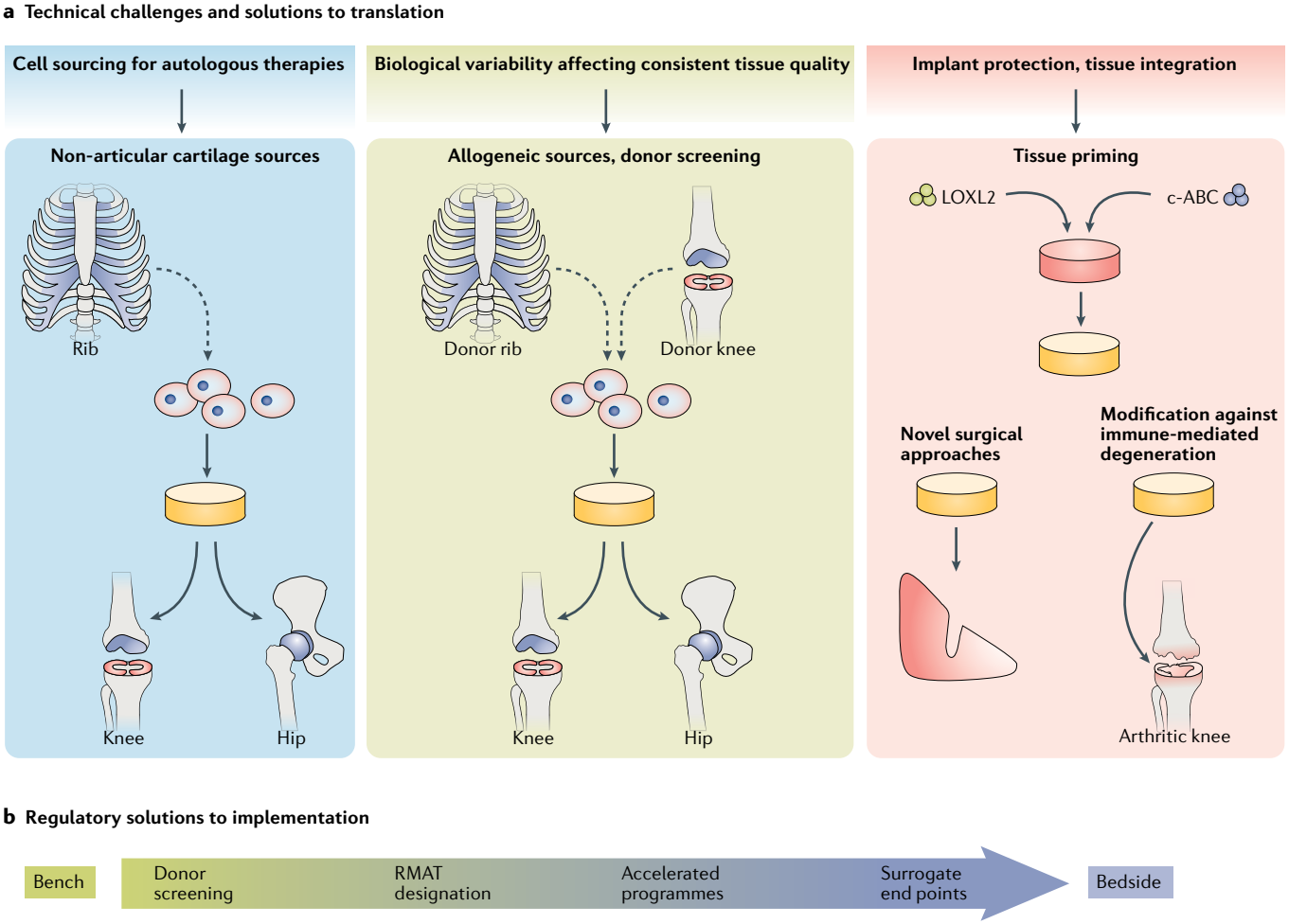

Fig. 4 | **Challenges to the clinical translation of engineered cartilage and meniscus products. a** | The main technical challenges to clinical translation include obtaining sufficient numbers of autologous cells, the effects of biological variability on the consistent production of high-quality engineered tissues and integration of the engineered tissues once implanted in vivo. Potential solutions and avenues of further investigation include: cells sourced from non-articulating cartilage (such as costal (rib) cartilage); allogeneic approaches, including extensive screening to identify appropriate donors; modification of engineered tissues to withstand immune-mediated degeneration within an inflamed joint; priming of engineered tissues with chondroitinase ABC (c-ABC) and lysyl oxidase-like 2 (LOXL2) for enhanced integration; and novel in vivo implantation methods that protect tissue-engineered implants. **b** | Regulatory challenges to clinical translation include the long time-frames and high costs associated with clinical trials. It is hoped that solutions such as the Regenerative Medicine Advanced Therapy (RMAT) designation, other FDA programmes that enable accelerated review and approval of applications, and the use of surrogate end points will help overcome these challenges.

ameliorate the immune response to ensure the survival of tissue-engineered implants in inflammatory environments, such as joints affected by OA and RA. Macrophage phenotypes can be modulated in vitro to promote healing and to potentially reduce inflammation in OA[166]. Other strategies to reduce inflammation, such as the use of adipose-derived MSCs to reduce matrix metalloproteinase 3 (MMP3) and MMP13 expression, also hold promise[167]. The rejection of allogeneic engineered cartilage and menisci is also a concern. Although articular cartilage is considered to be immune privileged, and fresh allografts (such as osteochondral allografts, DeNovo NT and meniscus allografts) are in current clinical use, the degree of immune privilege an implant has depends on its location within the knee joint and its proximity to the synovium[28]. Meniscus allografts are well tolerated, but it remains to be seen whether allogeneic neomenisci implanted into the vascular red–red zone of the meniscus would elicit an immune response. Osteochondral allografts are frequently used in articular cartilage repair and are well tolerated[33] despite the fact that the subchondral bone is vascularized, lending some support to the idea that red–red zone allografts might be tolerated. However, most irreparable meniscus defects that would require engineered meniscus grafts occur in the white–white zone, which does not contain vasculature. Thus, this area might also possess a degree of immune privilege, similar to articular cartilage, although the exact immune privilege status of the meniscus still needs further study. Efforts to minimize the immunogenicity of allogeneic and xenogeneic articular cartilage and menisci include decellularization and antigen removal[168–170], but these methods

typically create a disrupted matrix and non-viable cells, depriving the neotissue of the capacity for homeostasis, remodelling and integration. A variety of immunological challenges associated with cartilage and meniscus tissue engineering, such as the pro-inflammatory environment of arthritic joints and the antigenicity of allogeneic cells and matrix components, indicate that neotissue should be modified to be able to withstand or modulate the immune response to ensure graft survival and integration.

Regulatory concerns

Several regulatory hurdles surround the translation of engineered cartilage and meniscus products into patients (FIG. 4b). Clinical trials to examine the safety and efficacy of engineered cartilage and meniscus products in large patient populations are costly and time-consuming. Recognizing this, the FDA has announced a new policy framework to expedite the approval of new therapies while preserving public health via a risk-based approach. Special designations, such as the Regenerative Medicine Advanced Therapy (RMAT) designation, have been created to expedite the approval process[171]. Advantages of the RMAT designation include FDA assistance as early as the phase I trial stage, the discussion of potential surrogate or intermediate end points to accelerate approval and eligibility for priority review of marketing applications. The use of surrogate end points might accelerate time to market by shifting some of the burden of proof to post-market follow-up studies. The RMAT designation, as well as other special designations and accelerated programmes[171], might be solutions to reducing the cost and time required to gain marketing approval for engineered articular cartilage and meniscus products.

Conclusions

Current surgical repair techniques for articular cartilage and meniscus pathologies are insufficient to halt the development and progression of OA, which has accelerated the development of alternative tissue engineering strategies. Many advances have been made in cell sourcing and the use of stimuli to engineer neotissue akin to native articular cartilage and menisci, which can potentially provide long-term solutions for cartilage and meniscus healing. For example, the use of cells from allogeneic, non-articulating and/or diseased cartilage might counter the lack of native autologous cells. Although the goal of tissue engineering is to achieve biomimicry, tissue engineering approaches must also aim to create neotissue that withstands joint inflammation, readily integrates into surrounding native tissues and ensures positive outcomes regardless of biological variability and the age of the patient. The progression towards the use of cell-based tissue-engineered therapies in the clinic can be seen in the numerous clinical trials and Institutional Review Board-approved studies that are currently underway. Although most products are primarily indicated for use in the knee, many of the same engineering principles can be translated to the development of products for other joints such as the hip. The establishment of the RMAT designation should accelerate the regulatory process for these products. Rapidly emerging tissue engineering technologies could lead to the development of long-lasting products that are readily available off the shelf for articular cartilage and meniscus regeneration in the not-so-distant future.

Published online 11 July 2019

1. Centers for Disease Control and Prevention. Arthritis-related statistics. *CDC* https://www.cdc.gov/arthritis/data_statistics/arthritis-related-stats.htm (2018).
2. Centers for Disease Control and Prevention. Osteoarthritis. *CDC* https://www.cdc.gov/arthritis/basics/osteoarthritis.htm (2019).
3. Wilder, F. V., Hall, B. J., Barrett, J. P. Jr & Lemrow, N. B. History of acute knee injury and osteoarthritis of the knee: a prospective epidemiological assessment. The Clearwater Osteoarthritis Study. *Osteoarthritis Cartilage* **10**, 611–616 (2002).
4. Wellsandt, E. et al. Decreased knee joint loading associated with early knee osteoarthritis after anterior cruciate ligament injury. *Am. J. Sports Med.* **44**, 143–151 (2016).
5. Lohmander, L. S., Englund, P. M., Dahl, L. L. & Roos, E. M. The long-term consequence of anterior cruciate ligament and meniscus injuries: osteoarthritis. *Am. J. Sports Med.* **35**, 1756–1769 (2007).
6. Cross, M. et al. The global burden of hip and knee osteoarthritis: estimates from the Global Burden of Disease 2010 study. *Ann. Rheum. Dis.* **73**, 1323–1330 (2014).
7. Helmick, C. G. et al. Estimates of the prevalence of arthritis and other rheumatic conditions in the United States. Part I. *Arthritis Rheum.* **58**, 15–25 (2008).
8. Losina, E. et al. Lifetime medical costs of knee osteoarthritis management in the United States: impact of extending indications for total knee arthroplasty. *Arthritis Care Res.* **67**, 203–215 (2015).
9. Birnbaum, H. et al. Societal cost of rheumatoid arthritis patients in the US. *Curr. Med. Res. Opin.* **26**, 77–90 (2010).
10. Hochberg, M. C. et al. American College of Rheumatology 2012 recommendations for the use of nonpharmacologic and pharmacologic therapies in osteoarthritis of the hand, hip, and knee. *Arthritis Care Res.* **64**, 465–474 (2012).
11. Singh, J. A. et al. 2015 American College of Rheumatology Guideline for the treatment of rheumatoid arthritis. *Arthritis Care Res.* **68**, 1–25 (2016).
12. Makris, E. A., Gomoll, A. H., Malizos, K. N., Hu, J. C. & Athanasiou, K. A. Repair and tissue engineering techniques for articular cartilage. *Nat. Rev. Rheumatol.* **11**, 21–34 (2015).
13. Athanasiou, K. A., Darling, E. M., Hu, J. C., DuRaine, G. D. & Reddi, A. H. *Articular Cartilage* 2nd edn Ch. 4 257–389 (Taylor & Francis, 2016).
14. Moran, C. J., Busilacchi, A., Lee, C. A., Athanasiou, K. A. & Verdonk, P. C. Biological augmentation and tissue engineering approaches in meniscus surgery. *Arthroscopy* **31**, 944–955 (2015).
15. Athanasiou, K. A. & Sanchez-Adams, J. *Engineering the Knee Meniscus* Ch. 3 35–53 (Morgan & Claypool, 2009).
16. Curl, W. W. et al. Cartilage injuries: a review of 31,516 knee arthroscopies. *Arthroscopy* **13**, 456–460 (1997).
17. Hjelle, K., Solheim, E., Strand, T., Muri, R. & Brittberg, M. Articular cartilage defects in 1,000 knee arthroscopies. *Arthroscopy* **18**, 730–734 (2002).
18. Flanigan, D. C., Harris, J. D., Trinh, T. Q., Siston, R. A. & Brophy, R. H. Prevalence of chondral defects in athletes' knees: a systematic review. *Med. Sci. Sports Exerc.* **42**, 1795–1801 (2010).
19. Richter, D. L., Schenck, R. C. Jr, Wascher, D. C. & Treme, G. Knee articular cartilage repair and restoration techniques: a review of the literature. *Sports Health* **8**, 153–160 (2016).
20. Bedi, A., Feeley, B. T. & Williams, R. J. 3rd. Management of articular cartilage defects of the knee. *J. Bone Joint Surg. Am.* **92**, 994–1009 (2010).
21. Steadman, J. R., Rodkey, W. G. & Rodrigo, J. J. Microfracture: surgical technique and rehabilitation to treat chondral defects. *Clin. Orthop. Relat. Res.* **391**, S362–S369 (2001).
22. Gudas, R. et al. Ten-year follow-up of a prospective, randomized clinical study of mosaic osteochondral autologous transplantation versus microfracture for the treatment of osteochondral defects in the knee joint of athletes. *Am. J. Sports Med.* **40**, 2499–2508 (2012).
23. Solheim, E., Hegna, J., Strand, T., Harlem, T. & Inderhaug, E. Randomized study of long-term (15–17 years) outcome after microfracture versus mosaicplasty in knee articular cartilage defects. *Am. J. Sports Med.* **46**, 826–831 (2018).
24. Albright, J. C. & Daoud, A. K. Microfracture and microfracture plus. *Clin. Sports Med.* **36**, 501–507 (2017).
25. Gao, L., Orth, P., Cucchiarini, M. & Madry, H. Autologous matrix-induced chondrogenesis: a systematic review of the clinical evidence. *Am. J. Sports Med.* **47**, 222–231 (2017).
26. Krych, A. J. et al. Return to sport after the surgical management of articular cartilage lesions in the knee: a meta-analysis. *Knee Surg. Sports Traumatol. Arthrosc.* **25**, 3186–3196 (2017).
27. Hangody, L. et al. Autologous osteochondral mosaicplasty. Surgical technique. *J. Bone Joint Surg. Am.* **86-A**, S65–S72 (2004).
28. Arzi, B. et al. Cartilage immunoprivilege depends on donor source and lesion location. *Acta Biomater.* **23**, 72–81 (2015).
29. Koh, J. L., Kowalski, A. & Lautenschlager, E. The effect of angled osteochondral grafting on contact pressure: a biomechanical study. *Am. J. Sports Med.* **34**, 116–119 (2006).
30. Koh, J. L., Wirsing, K., Lautenschlager, E. & Zhang, L. O. The effect of graft height mismatch on contact pressure following osteochondral grafting: a biomechanical study. *Am. J. Sports Med.* **32**, 317–320 (2004).
31. Cook, J. L. et al. Importance of donor chondrocyte viability for osteochondral allografts. *Am. J. Sports Med.* **44**, 1260–1268 (2016).
32. Williams, R. J. 3rd, Ranawat, A. S., Potter, H. G., Carter, T. & Warren, R. F. Fresh stored allografts for the treatment of osteochondral defects of the knee. *J. Bone Joint Surg. Am.* **89**, 718–726 (2007).

33. Levy, Y. D., Gortz, S., Pulido, P. A., McCauley, J. C. & Bugbee, W. D. Do fresh osteochondral allografts successfully treat femoral condyle lesions? *Clin. Orthop. Relat. Res.* **471**, 231–237 (2013).
34. Hangody, L. & Fules, P. Autologous osteochondral mosaicplasty for the treatment of full-thickness defects of weight-bearing joints: ten years of experimental and clinical experience. *J. Bone Joint Surg. Am.* **85-A**, S25–S32 (2003).
35. Balazs, G. C. et al. Return to play among elite basketball players after osteochondral allograft transplantation of full-thickness cartilage lesions. *Orthop. J. Sports Med.* **6**, 2325967118786941 (2018).
36. Hinckel, B. B., Gomoll, A. H. & Farr, J. 2nd Cartilage restoration in the patellofemoral joint. *Am. J. Orthop.* **46**, 217–222 (2017).
37. Dunkin, B. S. & Lattermann, C. New and emerging techniques in cartilage repair: MACI. *Oper. Tech. Sports Med.* **21**, 100–107 (2013).
38. Ebert, J. R., Fallon, M., Wood, D. J. & Janes, G. C. A Prospective clinical and radiological evaluation at 5 years after arthroscopic matrix-induced autologous chondrocyte implantation. *Am. J. Sports Med.* **45**, 59–69 (2017).
39. Ebert, J. R., Fallon, M., Smith, A., Janes, G. C. & Wood, D. J. Prospective clinical and radiologic evaluation of patellofemoral matrix-induced autologous chondrocyte implantation. *Am. J. Sports Med.* **43**, 1362–1372 (2015).
40. Fillingham, Y. A., Riboh, J. C., Erickson, B. J., Bach, B. R. Jr & Yanke, A. B. Inside-out versus all-inside repair of isolated meniscal tears: an updated systematic review. *Am. J. Sports Med.* **45**, 234–242 (2017).
41. Barrett, G. R., Field, M. H., Treacy, S. H. & Ruff, C. G. Clinical results of meniscus repair in patients 40 years and older. *Arthroscopy* **14**, 824–829 (1998).
42. Eggli, S., Wegmuller, H., Kosina, J., Huckell, C. & Jakob, R. P. Long-term results of arthroscopic meniscal repair. An analysis of isolated tears. *Am. J. Sports Med.* **23**, 715–720 (1995).
43. Kim, S., Bosque, J., Meehan, J. P., Jamali, A. & Marder, R. Increase in outpatient knee arthroscopy in the United States: a comparison of National Surveys of Ambulatory Surgery, 1996 and 2006. *J. Bone Joint Surg. Am.* **93**, 994–1000 (2011).
44. Papalia, R., Del Buono, A., Osti, L., Denaro, V. & Maffulli, N. Meniscectomy as a risk factor for knee osteoarthritis: a systematic review. *Br. Med. Bull.* **99**, 89–106 (2011).
45. Abrams, G. D. et al. Trends in meniscus repair and meniscectomy in the United States, 2005–2011. *Am. J. Sports Med.* **41**, 2333–2339 (2013).
46. Johnson, M. J., Lucas, G. L., Dusek, J. K. & Henning, C. E. Isolated arthroscopic meniscal repair: a long-term outcome study (more than 10 years). *Am. J. Sports Med.* **27**, 44–49 (1999).
47. Pujol, N., Bohu, Y., Boisrenoult, P., Macdes, A. & Beaufils, P. Clinical outcomes of open meniscal repair of horizontal meniscal tears in young patients. *Knee Surg. Sports Traumatol. Arthrosc.* **21**, 1530–1533 (2013).
48. Choi, N. H., Kim, T. H., Son, K. M. & Victoroff, B. N. Meniscal repair for radial tears of the midbody of the lateral meniscus. *Am. J. Sports Med.* **38**, 2472–2476 (2010).
49. Wasserstein, D. et al. A matched-cohort population study of reoperation after meniscal repair with and without concomitant anterior cruciate ligament reconstruction. *Am. J. Sports Med.* **41**, 349–355 (2013).
50. Hutchinson, I. D., Moran, C. J., Potter, H. G., Warren, R. F. & Rodeo, S. A. Restoration of the meniscus: form and function. *Am. J. Sports Med.* **42**, 987–998 (2014).
51. Zhang, Z., Arnold, J. A., Williams, T. & McCann, B. Repairs by trephination and suturing of longitudinal injuries in the avascular area of the meniscus in goats. *Am. J. Sports Med.* **23**, 35–41 (1995).
52. Taylor, S. A. & Rodeo, S. A. Augmentation techniques for isolated meniscal tears. *Curr. Rev. Musculoskelet. Med.* **6**, 95–101 (2013).
53. Henning, C. E. et al. Arthroscopic meniscal repair using an exogenous fibrin clot. *Clin. Orthop. Relat. Res.* **252**, 64–72 (1990).
54. Dean, C. S., Chahla, J., Matheny, L. M., Mitchell, J. J. & LaPrade, R. F. Outcomes after biologically augmented isolated meniscal repair with marrow venting are comparable with those after meniscal repair with concomitant anterior cruciate ligament reconstruction. *Am. J. Sports Med.* **45**, 1341–1348 (2017).
55. Verdonk, R. et al. Indications and limits of meniscal allografts. *Injury* **44** (Suppl. 1), 21–27 (2013).
56. Rodeo, S. A. Meniscal allografts—where do we stand? *Am. J. Sports Med.* **29**, 246–261 (2001).
57. Lee, S. R., Kim, J. G. & Nam, S. W. The tips and pitfalls of meniscus allograft transplantation. *Knee Surg. Relat. Res.* **24**, 137–145 (2012).
58. Dienst, M., Greis, P. E., Ellis, B. J., Bachus, K. N. & Burks, R. T. Effect of lateral meniscal allograft sizing on contact mechanics of the lateral tibial plateau: an experimental study in human cadaveric knee joints. *Am. J. Sports Med.* **35**, 34–42 (2007).
59. Vundelinckx, B., Vanlauwe, J. & Bellemans, J. Long-term subjective, clinical, and radiographic outcome evaluation of meniscal allograft transplantation in the knee. *Am. J. Sports Med.* **42**, 1592–1599 (2014).
60. Lee, S. M. et al. Long-term outcomes of meniscal allograft transplantation with and without extrusion: mean 12.3-year follow-up study. *Am. J. Sports Med.* **47**, 815–821 (2019).
61. van Tienen, T. G., Hannink, G. & Buma, P. Meniscus replacement using synthetic materials. *Clin. Sport Med.* **28**, 143–156 (2009).
62. Bulgheroni, E. et al. Long-term outcomes of medial CMI implant versus partial medial meniscectomy in patients with concomitant ACL reconstruction. *Knee Surg. Sports Traumatol. Arthrosc.* **23**, 3221–3227 (2015).
63. Schuttler, K. F. et al. Midterm follow-up after implantation of a polyurethane meniscal scaffold for segmental medial meniscus loss: maintenance of good clinical and MRI outcome. *Knee Surg. Sports Traumatol. Arthrosc.* **24**, 1478–1484 (2016).
64. US National Library of Medicine. *ClinicalTrials.gov* https://clinicaltrials.gov/ct2/show/NCT02136901 (2018).
65. Marinescu, R. & Antoniac, I. in *Handbook of Bioceramics and Biocomposite* (ed. Antoniac, I. V.) 1–31 (Springer, Cham, 2015).
66. Kramer, D. E. & Micheli, L. J. Meniscal tears and discoid meniscus in children: diagnosis and treatment. *J. Am. Acad. Orthop. Surg.* **17**, 698–707 (2009).
67. Adirim, T. A. & Cheng, T. L. Overview of injuries in the young athlete. *Sports Med.* **33**, 75–81 (2003).
68. Beck, N. A., Lawrence, J. T. R., Nordin, J. D., DeFor, T. A. & Tompkins, M. ACL tears in school-aged children and adolescents over 20 years. *Pediatrics* **139**, e20161877 (2017).
69. Kreuz, P. C. et al. Is microfracture of chondral defects in the knee associated with different results in patients aged 40 years or younger? *Arthroscopy* **22**, 1180–1186 (2006).
70. Asik, M., Ciftci, F., Sen, C., Erdil, M. & Atalar, A. The microfracture technique for the treatment of full-thickness articular cartilage lesions of the knee: midterm results. *Arthroscopy* **24**, 1214–1220 (2008).
71. Mithoefer, K., McAdams, T., Williams, R. J., Kreuz, P. C. & Mandelbaum, B. R. Clinical efficacy of the microfracture technique for articular cartilage repair in the knee: an evidence-based systematic analysis. *Am. J. Sports Med.* **37**, 2053–2063 (2009).
72. Mithoefer, K. et al. The microfracture technique for the treatment of articular cartilage lesions in the knee. A prospective cohort study. *J. Bone Joint Surg. Am.* **87**, 1911–1920 (2005).
73. Gudas, R. et al. A prospective randomized clinical study of mosaic osteochondral autologous transplantation versus microfracture for the treatment of osteochondral defects in the knee joint in young athletes. *Arthroscopy* **21**, 1066–1075 (2005).
74. Murphy, R. T., Pennock, A. T. & Bugbee, W. D. Osteochondral allograft transplantation of the knee in the pediatric and adolescent population. *Am. J. Sports Med.* **42**, 635–640 (2014).
75. Frank, R. M. et al. Osteochondral allograft transplantation of the knee: analysis of failures at 5 years. *Am. J. Sports Med.* **45**, 864–874 (2017).
76. Micheli, L. J. et al. Articular cartilage defects of the distal femur in children and adolescents: treatment with autologous chondrocyte implantation. *J. Pediatr. Orthop.* **26**, 455–460 (2006).
77. Mithofer, K., Minas, T., Peterson, L., Yeon, H. & Micheli, L. J. Functional outcome of knee articular cartilage repair in adolescent athletes. *Am. J. Sports Med.* **33**, 1147–1153 (2005).
78. Knutsen, G. et al. Autologous chondrocyte implantation compared with microfracture in the knee. A randomized trial. *J. Bone Joint Surg. Am.* **86**, 455–464 (2004).
79. Saris, D. B. et al. Treatment of symptomatic cartilage defects of the knee: characterized chondrocyte implantation results in better clinical outcome at 36 months in a randomized trial compared to microfracture. *Am. J. Sports Med.* **37** (Suppl. 1), 10–19 (2009).
80. Gudas, R., Stankevicius, E., Monastyreckiene, E., Pranys, D. & Kalesinskas, R. J. Osteochondral autologous transplantation versus microfracture for the treatment of articular cartilage defects in the knee joint in athletes. *Knee Surg. Sports Traumatol. Arthrosc.* **14**, 834–842 (2006).
81. Kon, E. et al. Arthroscopic second-generation autologous chondrocyte implantation compared with microfracture for chondral lesions of the knee: prospective nonrandomized study at 5 years. *Am. J. Sports Med.* **37**, 33–41 (2009).
82. Noyes, F. R. & Barber-Westin, S. D. Meniscus transplantation: indications, techniques, clinical outcomes. *Instr. Course Lect.* **54**, 341–353 (2005).
83. Riboh, J. C., Tilton, A. K., Cvetanovich, G. L., Campbell, K. A. & Cole, B. J. Meniscal allograft transplantation in the adolescent population. *Arthroscopy* **32**, 1133–1140 (2016).
84. Steadman, J. R. et al. Meniscus suture repair: minimum 10-year outcomes in patients younger than 40 years compared with patients 40 and older. *Am. J. Sports Med.* **43**, 2222–2227 (2015).
85. Rothermel, S. D., Smuin, D. & Dhawan, A. Are outcomes after meniscal repair age dependent? A systematic review. *Arthroscopy* **34**, 979–987 (2018).
86. Nepple, J. J., Dunn, W. R. & Wright, R. W. Meniscal repair outcomes at greater than five years: a systematic literature review and meta-analysis. *J. Bone Joint Surg. Am.* **94**, 2222–2227 (2012).
87. Shyh-Chang, N. et al. Lin28 enhances tissue repair by reprogramming cellular metabolism. *Cell* **155**, 778–792 (2013).
88. Makris, E. A., Hadidi, P. & Athanasiou, K. A. The knee meniscus: structure-function, pathophysiology, current repair techniques, and prospects for regeneration. *Biomaterials* **32**, 7411–7431 (2011).
89. Bhattacharjee, M. et al. Tissue engineering strategies to study cartilage development, degeneration and regeneration. *Adv. Drug Deliv. Rev.* **84**, 107–122 (2015).
90. Rowland, C. R., Colucci, L. A. & Guilak, F. Fabrication of anatomically-shaped cartilage constructs using decellularized cartilage-derived matrix scaffolds. *Biomaterials* **91**, 57–72 (2016).
91. Shimomura, K., Rothrauff, B. B. & Tuan, R. S. Region-specific effect of the decellularized meniscus extracellular matrix on mesenchymal stem cell-based meniscus tissue engineering. *Am. J. Sports Med.* **45**, 604–611 (2017).
92. Liu, M. et al. Injectable hydrogels for cartilage and bone tissue engineering. *Bone Res.* **5**, 17014 (2017).
93. Guo, T., Lembong, J., Zhang, L. G. & Fisher, J. P. Three-dimensional printing articular cartilage: recapitulating the complexity of native tissue. *Tissue Eng. B* **23**, 225–236 (2017).
94. Shen, S. et al. 3D printing-based strategies for functional cartilage regeneration. *Tissue Eng. B* https://doi.org/10.1089/ten.teb.2018.0248 (2019).
95. Athanasiou, K. A., Eswaramoorthy, R., Hadidi, P. & Hu, J. C. Self-organization and the self-assembling process in tissue engineering. *Annu. Rev. Biomed. Eng.* **15**, 115–136 (2013).
96. Hu, J. C. & Athanasiou, K. A. A self-assembling process in articular cartilage tissue engineering. *Tissue Eng.* **12**, 969–979 (2006).
97. Hoben, G. M., Hu, J. C., James, R. A. & Athanasiou, K. A. Self-assembly of fibrochondrocytes and chondrocytes for tissue engineering of the knee meniscus. *Tissue Eng.* **13**, 939–946 (2007).
98. Ofek, G. et al. Matrix development in self-assembly of articular cartilage. *PLoS One* **3**, e2795 (2008).
99. Lee, J. K. et al. Tension stimulation drives tissue formation in scaffold-free systems. *Nat. Mater.* **16**, 864–873 (2017).
100. Elder, B. D. & Athanasiou, K. A. Systematic assessment of growth factor treatment on biochemical and biomechanical properties of engineered articular cartilage constructs. *Osteoarthritis Cartilage* **17**, 114–123 (2009).
101. Little, C. J., Bawolin, N. K. & Chen, X. Mechanical properties of natural cartilage and tissue-engineered constructs. *Tissue Eng. B* **17**, 213–227 (2011).
102. Gunja, N. J., Huey, D. J., James, R. A. & Athanasiou, K. A. Effects of agarose mould compliance and surface roughness on self-assembled meniscus-shaped constructs. *J. Tissue Eng. Regen. Med.* **3**, 521–530 (2009).

103. Makris, E. A., MacBarb, R. F., Paschos, N. K., Hu, J. C. & Athanasiou, K. A. Combined use of chondroitinase-ABC, TGF-β1, and collagen crosslinking agent lysyl oxidase to engineer functional neotissues for fibrocartilage repair. *Biomaterials* **35**, 6787–6796 (2014).
104. Zhu, D., Tong, X., Trinh, P. & Yang, F. Mimicking cartilage tissue zonal organization by engineering tissue-scale gradient hydrogels as 3D cell niche. *Tissue Eng. A* **24**, 1–10 (2018).
105. Steele, J. A. et al. Combinatorial scaffold morphologies for zonal articular cartilage engineering. *Acta Biomater.* **10**, 2065–2075 (2014).
106. Zitnay, J. L. et al. Fabrication of dense anisotropic collagen scaffolds using biaxial compression. *Acta Biomater.* **65**, 76–87 (2018).
107. Higashioka, M. M., Chen, J. A., Hu, J. C. & Athanasiou, K. A. Building an anisotropic meniscus with zonal variations. *Tissue Eng. A* **20**, 294–302 (2014).
108. Darling, E. M. & Athanasiou, K. A. Rapid phenotypic changes in passaged articular chondrocyte subpopulations. *J. Orthop. Res.* **23**, 425–432 (2005).
109. Huwe, L. W., Brown, W. E., Hu, J. C. & Athanasiou, K. A. Characterization of costal cartilage and its suitability as a cell source for articular cartilage tissue engineering. *J. Tissue Eng. Regen. Med.* **12**, 1163–1176 (2018).
110. Kwon, H., O'Leary, S. A., Hu, J. C. & Athanasiou, K. A. Translating the application of transforming growth factor-β1, chondroitinase-ABC, and lysyl oxidase-like 2 for mechanically robust tissue-engineered human neocartilage. *J. Tissue Eng. Regen. Med.* **13**, 283–294 (2019).
111. Murphy, M. K., Huey, D. J., Hu, J. C. & Athanasiou, K. A. TGF-β1, GDF-5, and BMP-2 stimulation induces chondrogenesis in expanded human articular chondrocytes and marrow-derived stromal cells. *Stem Cells* **33**, 762–773 (2015).
112. Pelttari, K. et al. Adult human neural crest-derived cells for articular cartilage repair. *Sci. Transl Med.* **6**, 251ra119 (2014).
113. US National Library of Medicine. *ClinicalTrials.gov* https://clinicaltrials.gov/ct2/show/NCT02673905 (2018).
114. Bianchi, V. J., Weber, J. F., Waldman, S. D., Backstein, D. & Kandel, R. A. Formation of hyaline cartilage tissue by passaged human osteoarthritic chondrocytes. *Tissue Eng. A* **23**, 156–165 (2017).
115. Kwon, H. et al. Tissue engineering potential of human dermis-isolated adult stem cells from multiple anatomical locations. *PLoS One* **12**, e0182531 (2017).
116. Lavoie, J. F. et al. Skin-derived precursors differentiate into skeletogenic cell types and contribute to bone repair. *Stem Cells Dev.* **18**, 893–906 (2009).
117. Fu, W. L., Zhou, C. Y. & Yu, J. K. A new source of mesenchymal stem cells for articular cartilage repair: MSCs derived from mobilized peripheral blood share similar biological characteristics in vitro and chondrogenesis in vivo as MSCs from bone marrow in a rabbit model. *Am. J. Sports Med.* **42**, 592–601 (2014).
118. Chang, N. J. et al. Transplantation of autologous endothelial progenitor cells in porous PLGA scaffolds create a microenvironment for the regeneration of hyaline cartilage in rabbits. *Osteoarthritis Cartilage* **21**, 1613–1622 (2013).
119. Jiang, Y. et al. Human cartilage-derived progenitor cells from committed chondrocytes for efficient cartilage repair and regeneration. *Stem Cells Transl Med.* **5**, 733–744 (2016).
120. Somoza, R. A., Welter, J. F., Correa, D. & Caplan, A. I. Chondrogenic differentiation of mesenchymal stem cells: challenges and unfulfilled expectations. *Tissue Eng. B* **20**, 596–608 (2014).
121. Chen, S., Fu, P., Cong, R., Wu, H. & Pei, M. Strategies to minimize hypertrophy in cartilage engineering and regeneration. *Genes Dis.* **2**, 76–95 (2015).
122. Kwon, H., Paschos, N. K., Hu, J. C. & Athanasiou, K. Articular cartilage tissue engineering: the role of signaling molecules. *Cell. Mol. Life Sci.* **73**, 1173–1194 (2016).
123. Feng, Q. et al. Sulfated hyaluronic acid hydrogels with retarded degradation and enhanced growth factor retention promote hMSC chondrogenesis and articular cartilage integrity with reduced hypertrophy. *Acta Biomater.* **53**, 329–342 (2017).
124. Amann, E., Wolff, P., Breel, E., van Griensven, M. & Balmayor, E. R. Hyaluronic acid facilitates chondrogenesis and matrix deposition of human adipose derived mesenchymal stem cells and human chondrocytes co-cultures. *Acta Biomater.* **52**, 130–144 (2017).
125. Liu, Q. et al. Suppressing mesenchymal stem cell hypertrophy and endochondral ossification in 3D cartilage regeneration with nanofibrous poly(l-lactic acid) scaffold and matrilin-3. *Acta Biomater.* **76**, 29–38 (2018).
126. Johnson, K. et al. A stem cell-based approach to cartilage repair. *Science* **336**, 717–721 (2012).
127. Cai, G. et al. Recent advances in kartogenin for cartilage regeneration. *J. Drug Target* **27**, 28–32 (2019).
128. Bian, L. et al. Influence of temporary chondroitinase ABC-induced glycosaminoglycan suppression on maturation of tissue-engineered cartilage. *Tissue Eng. A* **15**, 2065–2072 (2009).
129. Natoli, R. M., Revell, C. M. & Athanasiou, K. A. Chondroitinase ABC treatment results in greater tensile properties of self-assembled tissue-engineered articular cartilage. *Tissue Eng. A* **15**, 3119–3128 (2009).
130. Makris, E. A., Responte, D. J., Paschos, N. K., Hu, J. C. & Athanasiou, K. A. Developing functional musculoskeletal tissues through hypoxia and lysyl oxidase-induced collagen cross-linking. *Proc. Natl Acad. Sci. USA* **111**, E4832–E4841 (2014).
131. Makris, E. A., Hu, J. C. & Athanasiou, K. A. Hypoxia-induced collagen crosslinking as a mechanism for enhancing mechanical properties of engineered articular cartilage. *Osteoarthritis Cartilage* **21**, 634–641 (2013).
132. Athanasiou, K. A., Darling, E. M., Hu, J. C., DuRaine, G. D. & Reddi, A. H. *Articular Cartilage* 2nd edn Ch. 1 18–25 (Taylor & Francis, 2016).
133. Huwe, L. W., Sullan, G. K., Hu, J. C. & Athanasiou, K. A. Using costal chondrocytes to engineer articular cartilage with applications of passive axial compression and bioactive stimuli. *Tissue Eng. A* **24**, 516–526 (2018).
134. Meinert, C., Schrobback, K., Hutmacher, D. W. & Klein, T. J. A novel bioreactor system for biaxial mechanical loading enhances the properties of tissue-engineered human cartilage. *Sci. Rep.* **7**, 16997 (2017).
135. Son, M. S. & Levenston, M. E. Quantitative tracking of passage and 3D culture effects on chondrocyte and fibrochondrocyte gene expression. *J. Tissue Eng. Regen. Med.* **11**, 1185–1194 (2017).
136. Zellner, J. et al. Role of mesenchymal stem cells in tissue engineering of meniscus. *J. Biomed. Mater. Res. A* **94**, 1150–1161 (2010).
137. Moriguchi, Y. et al. Repair of meniscal lesions using a scaffold-free tissue-engineered construct derived from allogenic synovial MSCs in a miniature swine model. *Biomaterials* **34**, 2185–2193 (2013).
138. Sasaki, H. et al. In vitro repair of meniscal radial tear with hydrogels seeded with adipose stem cells and TGF-β3. *Am. J. Sports Med.* **46**, 2402–2413 (2018).
139. Koh, R. H., Jin, Y. J., Kang, B. J. & Hwang, N. S. Chondrogenically primed tonsil-derived mesenchymal stem cells encapsulated in riboflavin-induced photocrosslinking collagen-hyaluronic acid hydrogel for meniscus tissue repairs. *Acta Biomater.* **53**, 318–328 (2017).
140. Xie, X. et al. A co-culture system of rat synovial stem cells and meniscus cells promotes cell proliferation and differentiation as compared to mono-culture. *Sci. Rep.* **8**, 7693 (2018).
141. Hadidi, P. et al. Tendon and ligament as novel cell sources for engineering the knee meniscus. *Osteoarthritis Cartilage* **24**, 2126–2134 (2016).
142. Pangborn, C. A. & Athanasiou, K. A. Growth factors and fibrochondrocytes in scaffolds. *J. Orthop. Res.* **23**, 1184–1190 (2005).
143. Bonnevie, E. D., Puetzer, J. L. & Bonassar, L. J. Enhanced boundary lubrication properties of engineered menisci by lubricin localization with insulin-like growth factor I treatment. *J. Biomech.* **47**, 2183–2188 (2014).
144. Lee, C. H. et al. Protein-releasing polymeric scaffolds induce fibrochondrocytic differentiation of endogenous cells for knee meniscus regeneration in sheep. *Sci. Transl Med.* **6**, 266ra171 (2014).
145. Liang, Y. et al. Plasticity of human meniscus fibrochondrocytes: a study on effects of mitotic divisions and oxygen tension. *Sci. Rep.* **7**, 12148 (2017).
146. Croutze, R., Jomha, N., Uludag, H. & Adesida, A. Matrix forming characteristics of inner and outer human meniscus cells on 3D collagen scaffolds under normal and low oxygen tensions. *BMC Musculoskelet. Disord.* **14**, 353 (2013).
147. Huey, D. J. & Athanasiou, K. A. Tension-compression loading with chemical stimulation results in additive increases to functional properties of anatomic meniscal constructs. *PLoS One* **6**, e27857 (2011).
148. Zellner, J. et al. Dynamic hydrostatic pressure enhances differentially the chondrogenesis of meniscal cells from the inner and outer zone. *J. Biomech.* **48**, 1479–1484 (2015).
149. Puetzer, J. L. & Bonassar, L. J. Physiologically distributed loading patterns drive the formation of zonally organized collagen structures in tissue-engineered meniscus. *Tissue Eng. A* **22**, 907–916 (2016).
150. MacBarb, R. F., Chen, A. L., Hu, J. C. & Athanasiou, K. A. Engineering functional anisotropy in fibrocartilage neotissues. *Biomaterials* **34**, 9980–9989 (2013).
151. Huang, B. J., Hu, J. C. & Athanasiou, K. A. Cell-based tissue engineering strategies used in the clinical repair of articular cartilage. *Biomaterials* **98**, 1–22 (2016).
152. McCormick, F. et al. Treatment of focal cartilage defects with a juvenile allogeneic 3-dimensional articular cartilage graft. *Oper. Tech. Sports Med.* **21**, 95–99 (2013).
153. Park, Y. B., Ha, C. W., Lee, C. H., Yoon, Y. C. & Park, Y. G. Cartilage regeneration in osteoarthritic patients by a composite of allogeneic umbilical cord blood-derived mesenchymal stem cells and hyaluronate hydrogel: results from a clinical trial for safety and proof-of-concept with 7 years of extended follow-up. *Stem Cells Transl Med.* **6**, 613–621 (2017).
154. US National Library of Medicine. *ClinicalTrials.gov* https://clinicaltrials.gov/ct2/show/NCT01733186 (2018).
155. Rhee, C., Amar, E., Glazebrook, M., Coday, C. & Wong, I. H. Safety profile and short-term outcomes of BST-CarGel as an adjunct to microfracture for the treatment of chondral lesions of the hip. *Orthop. J. Sports Med.* **6**, 2325967118789871 (2018).
156. Tahoun, M. et al. Results of arthroscopic treatment of chondral delamination in femoroacetabular impingement with bone marrow stimulation and BST-CarGel((R)). *SICOT J.* **3**, 51 (2017).
157. Thier, S., Weiss, C. & Fickert, S. Arthroscopic autologous chondrocyte implantation in the hip for the treatment of full-thickness cartilage defects—a case series of 29 patients and review of the literature. *SICOT J.* **3**, 72 (2017).
158. Whitehouse, M. R. et al. Repair of torn avascular meniscal cartilage using undifferentiated autologous mesenchymal stem cells: from in vitro optimization to a first-in-human study. *Stem Cells Transl Med.* **6**, 1237–1248 (2017).
159. Vangsness, C. T. Jr. et al. Adult human mesenchymal stem cells delivered via intra-articular injection to the knee following partial medial meniscectomy: a randomized, double-blind, controlled study. *J. Bone Joint Surg.* **96**, 90–98 (2014).
160. Murphy, M. K., Masters, T. E., Hu, J. C. & Athanasiou, K. A. Engineering a fibrocartilage spectrum through modulation of aggregate redifferentiation. *Cell Transplant.* **24**, 235–245 (2015).
161. Martin, F., Lehmann, M., Sack, U. & Anderer, U. Featured article: In vitro development of personalized cartilage microtissues uncovers an individualized differentiation capacity of human chondrocytes. *Exp. Biol. Med.* **242**, 1746–1756 (2017).
162. Vapniarsky, N. et al. Tissue engineering toward temporomandibular joint disc regeneration. *Sci. Transl Med.* **10**, eaaq1802 (2018).
163. US Food & Drug Administration. Guidance for industry: eligibility determination for donors of human cells, tissues, and cellular and tissue-based products (HCT/Ps). *FDA.gov* https://www.fda.gov/media/73072/download (2015).
164. Arvayo, A. L., Wong, I. J., Dragoo, J. L. & Levenston, M. E. Enhancing integration of articular cartilage grafts via photochemical bonding. *J. Orthop. Res.* **36**, 2406–2415 (2018).
165. Athens, A. A., Makris, E. A. & Hu, J. C. Induced collagen cross-links enhance cartilage integration. *PLoS One* **8**, e60719 (2013).
166. Utomo, L., van Osch, G. J., Bayon, Y., Verhaar, J. A. & Bastiaansen-Jenniskens, Y. M. Guiding synovial inflammation by macrophage phenotype modulation: an in vitro study towards a therapy for osteoarthritis. *Osteoarthritis Cartilage* **24**, 1629–1638 (2016).
167. Lai, J. H. et al. Interaction between osteoarthritic chondrocytes and adipose-derived stem cells is dependent on cell distribution in three-dimension and transforming growth factor-β3 induction. *Tissue Eng. A* **21**, 992–1002 (2015).

168. Elder, B. D., Eleswarapu, S. V. & Athanasiou, K. A. Extraction techniques for the decellularization of tissue engineered articular cartilage constructs. *Biomaterials* **30**, 3749–3756 (2009).
169. Cissell, D. D., Hu, J. C., Griffiths, L. G. & Athanasiou, K. A. Antigen removal for the production of biomechanically functional, xenogeneic tissue grafts. *J. Biomech.* **47**, 1987–1996 (2014).
170. McNickle, A. G., Wang, V. M., Shewman, E. F., Cole, B. J. & Williams, J. M. Performance of a sterile meniscal allograft in an ovine model. *Clin. Orthop. Relat. Res.* **467**, 1868–1876 (2009).
171. US Food & Drug Administration. Expedited programs for regenerative medicine therapies for serious conditions: guidance for industry. *FDA.gov* https://www.fda.gov/media/120267/download (2017).
172. Nehrer, S., Chiari, C., Domayer, S., Barkay, H. & Yayon, A. Results of chondrocyte implantation with a fibrin-hyaluronan matrix: a preliminary study. *Clin. Orthop. Relat. Res.* **466**, 1849–1855 (2008).
173. Domayer, S. E. et al. T2 mapping and dGEMRIC after autologous chondrocyte implantation with a fibrin-based scaffold in the knee: preliminary results. *Eur. J. Radiol.* **73**, 636–642 (2010).
174. Fontana, A., Bistolfi, A., Crova, M., Rosso, F. & Massazza, G. Arthroscopic treatment of hip chondral defects: autologous chondrocyte transplantation versus simple debridement—a pilot study. *Arthroscopy* **28**, 322–329 (2012).
175. Ossendorf, C. et al. Treatment of posttraumatic and focal osteoarthritic cartilage defects of the knee with autologous polymer-based three-dimensional chondrocyte grafts: 2-year clinical results. *Arthritis Res. Ther.* **9**, R41 (2007).
176. Kreuz, P. C., Muller, S., Ossendorf, C., Kaps, C. & Erggelet, C. Treatment of focal degenerative cartilage defects with polymer-based autologous chondrocyte grafts: four-year clinical results. *Arthritis Res. Ther.* **11**, R33 (2009).
177. Stanish, W. D. et al. Novel scaffold-based BST-CarGel treatment results in superior cartilage repair compared with microfracture in a randomized controlled trial. *J. Bone Joint Surg. Am.* **95**, 1640–1650 (2013).
178. Schneider, U. et al. A prospective multicenter study on the outcome of type I collagen hydrogel-based autologous chondrocyte implantation (CaReS) for the repair of articular cartilage defects in the knee. *Am. J. Sports Med.* **39**, 2558–2565 (2011).
179. Cole, B. J. et al. Outcomes after a single-stage procedure for cell-based cartilage repair: a prospective clinical safety trial with 2-year follow-up. *Am. J. Sports Med.* **39**, 1170–1179 (2011).
180. Selmi, T. A. et al. Autologous chondrocyte implantation in a novel alginate-agarose hydrogel: outcome at two years. *J. Bone Joint Surg. Br.* **90**, 597–604 (2008).
181. Clave, A. et al. Third-generation autologous chondrocyte implantation versus mosaicplasty for knee cartilage injury: 2-year randomized trial. *J. Orthop. Res.* **34**, 658–665 (2016).
182. Fickert, S. et al. One-year clinical and radiological results of a prospective, investigator-initiated trial examining a novel, purely autologous 3-dimensional autologous chondrocyte transplantation product in the knee. *Cartilage* **3**, 27–42 (2012).
183. Meyer, U., Meyer, Th., Handschel, J. & Wiesmann, H. P. (eds) *Fundamentals of Tissue Engineering and Regenerative Medicine* (Springer, 2009).
184. Gobbi, A. et al. One-step surgery with multipotent stem cells and hyaluronan-based scaffold for the treatment of full-thickness chondral defects of the knee in patients older than 45 years. *Knee Surg. Sports Traumatol. Arthrosc.* **25**, 2494–2501 (2017).
185. Marcacci, M. et al. Articular cartilage engineering with Hyalograft C: 3-year clinical results. *Clin. Orthopaed. Related Res.* **435**, 96–105 (2005).
186. Nehrer, S. et al. Three-year clinical outcome after chondrocyte transplantation using a hyaluronan matrix for cartilage repair. *Eur. J. Radiol.* **57**, 3–8 (2006).
187. Tognana, E., Borrione, A., De Luca, C. & Pavesio, A. Hyalograft C: hyaluronan-based scaffolds in tissue-engineered cartilage. *Cells Tissues Organs* **186**, 97–103 (2007).
188. Brittberg, M. in *Techniques in Cartilage Repair Surgery* Ch. 19 (eds Shetty, A. A. et al.) 227–235 (Springer, 2014).
189. Hendriks, J. et al. First clinical experience with INSTRUCT—a single surgery, autologous cell based technology for cartilage repair [poster]. *CellCoTec* http://www.cellcotec.com/wp-content/uploads/2017/11/P187-first-clinical-experience-with-INSTRUCT-final2.pdf (2013).
190. Zak, L. et al. Results 2 years after matrix-associated autologous chondrocyte transplantation using the Novocart 3D scaffold: an analysis of clinical and radiological data. *Am. J. Sports Med.* **42**, 1618–1627 (2014).
191. Crawford, D. C., DeBerardino, T. M. & Williams, R. J. 3rd NeoCart, an autologous cartilage tissue implant, compared with microfracture for treatment of distal femoral cartilage lesions: an FDA phase-II prospective, randomized clinical trial after two years. *J. Bone Joint Surg. Am.* **94**, 979–989 (2012).
192. Crawford, D. C. et al. An autologous cartilage tissue implant NeoCart for treatment of grade III chondral injury to the distal femur: prospective clinical safety trial at 2 years. *Am. J. Sports Med.* **37**, 1334–1343 (2009).
193. Mizuno, S., Kusanagi, A., Tarrant, L. J. B., Tokuno, T. & Smith, R. L. Systems for cartilage repair. US Patent 20130273121A1 (2013).
194. Mumme, M. et al. Nasal chondrocyte-based engineered autologous cartilage tissue for repair of articular cartilage defects: an observational first-in-human trial. *Lancet* **388**, 1985–1994 (2016).
195. US National Library of Medicine. *ClinicalTrials.gov* https://clinicaltrials.gov/ct2/show/NCT00729716 (2012).
196. European Medicines Agency. *EU Clinical Trials Register* https://www.clinicaltrialsregister.eu/ctr-search/trial/2011-003594-28/DE (2011).
197. German Institute of Medical Documentation and Information. *German Clinical Trials Register* http://www.drks.de/DRKS00010658 (2016).
198. US National Library of Medicine. *ClinicalTrials.gov* https://clinicaltrials.gov/ct2/show/NCT02981355 (2018).
199. US National Library of Medicine. *ClinicalTrials.gov* https://clinicaltrials.gov/ct2/show/NCT02540200 (2016).
200. Shive, M. S. et al. BST-CarGel(R) treatment maintains cartilage repair superiority over microfracture at 5 years in a multicenter randomized controlled trial. *Cartilage* **6**, 62–72 (2015).
201. US National Library of Medicine. *ClinicalTrials.gov* https://clinicaltrials.gov/ct2/show/NCT01498029 (2012).
202. US National Library of Medicine. *ClinicalTrials.gov* https://clinicaltrials.gov/ct2/show/NCT00881023 (2016).
203. US National Library of Medicine. *ClinicalTrials.gov* https://clinicaltrials.gov/ct2/show/NCT00945399 (2015).
204. European Medicines Agency. *EU Clinical Trials Register* https://www.clinicaltrialsregister.eu/ctr-search/trial/2007-003481-18/BE (2008).
205. US National Library of Medicine. *ClinicalTrials.gov* https://clinicaltrials.gov/ct2/show/NCT01626677 (2017).
206. US National Library of Medicine. *ClinicalTrials.gov* https://clinicaltrials.gov/ct2/show/NCT01041001 (2017).
207. US National Library of Medicine. *ClinicalTrials.gov* https://clinicaltrials.gov/ct2/show/NCT01222559 (2018).
208. Becher, C. et al. Safety of three different product doses in autologous chondrocyte implantation: results of a prospective, randomised, controlled trial. *J. Orthop. Surg. Res.* **12**, 71 (2017).
209. US National Library of Medicine. *ClinicalTrials.gov* https://clinicaltrials.gov/ct2/show/NCT02659215 (2018).
210. US National Library of Medicine. *ClinicalTrials.gov* https://clinicaltrials.gov/ct2/show/NCT03219307 (2019).
211. US National Library of Medicine. *ClinicalTrials.gov* https://clinicaltrials.gov/ct2/show/NCT02348697 (2019).
212. US National Library of Medicine. *ClinicalTrials.gov* https://clinicaltrials.gov/ct2/show/NCT01957722 (2019).
213. US National Library of Medicine. *ClinicalTrials.gov* https://clinicaltrials.gov/ct2/show/NCT01656902 (2018).
214. US National Library of Medicine. *ClinicalTrials.gov* https://clinicaltrials.gov/ct2/show/NCT03319797 (2019).
215. US National Library of Medicine. *ClinicalTrials.gov* https://clinicaltrials.gov/ct2/show/NCT02941120 (2019).
216. US National Library of Medicine. *ClinicalTrials.gov* https://clinicaltrials.gov/ct2/show/NCT02179346 (2019).
217. US National Library of Medicine. *ClinicalTrials.gov* https://clinicaltrials.gov/ct2/show/NCT01066702 (2019).
218. Anderson, D. E. et al. Magnetic resonance imaging characterization and clinical outcomes after neocart surgical therapy as a primary reparative treatment for knee cartilage injuries. *Am. J. Sports Med.* **45**, 875–883 (2017).
219. US National Library of Medicine. *ClinicalTrials.gov* https://clinicaltrials.gov/ct2/show/NCT01400607 (2017).
220. US National Library of Medicine. *ClinicalTrials.gov* https://clinicaltrials.gov/ct2/show/NCT00702741 (2014).
221. European Medicines Agency. *EU Clinical Trials Register* https://www.clinicaltrialsregister.eu/ctr-search/trial/2010-024162-22/GB (2011).

Acknowledgements
The work of the authors was supported by the National Institutes of Health (grants R01AR067821 and R01AR071457 to K.A.A.), and by funds provided by the Henry Samueli Chair in Engineering.

Author contributions
H.K., W.E.B., C.A.L., D.W., N.P. and J.C.H. researched data for this article. All authors provided substantial contributions to the discussion of content, wrote the article and reviewed and/or edited the article before submission. H.K. and W.E.B. contributed equally to this article.

Competing interests
W.E.B. declares she is the Director of Outreach and a social media contributor for Science Cheerleaders, Incorporated. C.A.L. declares she is on the advisory board of Vericel. N.P. declares he is an associate editor of the Arthroscopy Journal. K.A.A. declares he is on the scientific advisory board of Histogenics. K.A.A., J.C.H., H.K. and W.E.B. declare they are listed as co-authors of submitted US patent applications (16/136,894 and 16/137,120). D.W. declares no competing interests.

Peer review information
Nature Reviews Rheumatology thanks H. Madry, E. Kon and D. J. Kelly for their contribution to the peer review of this work.

Publisher's note
Springer Nature remains neutral with regard to jurisdictional claims in published maps and institutional affiliations.

Supplementary information
Supplementary information is available for this paper at https://doi.org/10.1038/s41584-019-0255-1.